ALICE Tomography Section: Phase-Space Measurements and Analysis

Thesis submitted in accordance with the requirements of
the University of Liverpool for the degree of Doctor in Philosophy
by
Mark Gerard Ibison

September 2013

Abstract

The technique of phase-space tomography applies the principles of tomographic reconstruction to the diagnostics of particle accelerator beams. It is one of the few methods capable of mapping phase-space in detail, using instrumentation commonly available on research accelerator beam-lines, that is, beam profile imaging and variable focussing magnets.

This thesis studies the effects of space-charge in the particle bunch on the measurement of transverse phase-space, in the horizontal and vertical dimensions, by the beam tomography method. It applies a novel 'comparative' method of using quadrupole tomography scanning to look for these effects, over the length of the diagnostic section of the injection line which transfers the electron beam from the ALICE accelerator to the Electron Model for Many Applications (EMMA) ring at the Daresbury Laboratory. Simulations of the full tomographic process, from beam profile imaging to reconstruction, are developed in the particle tracking code GPT. These are used to investigate space-charge effects, in support of the experimental studies.

The concept of 'normalised phase-space' is described, in the context of tomography with a very limited number of views, presenting its advantages as applied to a specific type of reconstruction algorithm, the Maximum Entropy Technique. Recommendations for future work in this field are suggested, with possible application both for new machines at the Daresbury Laboratory, and at other accelerator facilities.

Contents

List of Figures

Acknowledgements

The author wishes to thank ...

Dr Kai Hock, my Supervisor, for his continuously constructive criticism and his patience, and in particular for assistance with developing specific code modules, especially for the tomographic reconstruction algorithms;

Dr Andrzej (Andy) Wolski, my second Supervisor, for his expert advice and unfailing encouragement, and for his most useful comments on the draft as it approached completion;

Dr David Holder, for his invaluable assistance especially in volunteering to help run experiments during the ‘graveyard shift’ on the ALICE accelerator, and in overcoming some of the more obscure LaTeX issues;

the Science and Technology Facilities Council (STFC), for its financial support during my studentship, without which my studies would not have been possible;

the late Rev J. P. (‘Pedro’) Williams for his excellent ‘A’ Level teaching at Preston Catholic College, which turned me towards becoming a physicist rather than a chemist;

and last, but definitely not least

my dear wife Mary, who encouraged me to embark on these studies and cajoled me into completing them.

List of Publications

Refereed Journals

1. S. Machida, M. Ibison et al, "Acceleration in the linear non-scaling fixed-field alternating-gradient accelerator EMMA", Nature Physics 8, 243247 (2012).
2. M. G. Ibison, K. M. Hock, et al, "ALICE Tomography Section: Measurements and Analysis", Journal of Instrumentation, 7, P04016 (2012).
3. K. M. Hock, M. G. Ibison, et al, "Beam tomography in transverse normalised phase space", Nuclear Instruments and Methods A, vol. 642, (2011), pp. 36-44.
4. K. M. Hock and M. G. Ibison, "A study of the Maximum Entropy Technique for phase space tomography", Journal of Instrumentation, in press (2013).

Conference Proceedings

1. M. G. Ibison, K. M. Hock, D. J. Holder, M. Korostelev, "Development of tomographic reconstruction methods for studies of transverse phase space in the EMMA FFAG injection line", presented at 1st International Particle Accelerator Conference (IPAC 10), Kyoto, Japan, 23-28 May 2010
2. M. G. Ibison, K. M. Hock, D. J. Holder, M. Korostelev, B. D. Muratori, A. Wolski, "Measurements at the ALICE tomography section", presented at the Conference 'IPAC 11', San Sebastian, Spain, September 2011
3. M. G. Ibison, K. M. Hock, D. J. Holder, M. Korostelev, B. D. Muratori, A. Wolski, "The effect of space-charge on the tomographic measurement of transverse phase space in the EMMA injection line", presented at the Conference 'IPAC 11', San Sebastian, Spain, September 2011
4. M. G. Ibison, K. M. Hock, D. J. Holder, B. D. Muratori, and A. Wolski, "Modelling Space-Charge and its Influence on the Measurement of Phase-Space in ALICE by Tomographic Methods", presented at the Conference 'IPAC 12', New Orleans, USA, May 2012

Chapter 1

Introduction

1.1 Overall Objectives of the Project

The principal goal of the project was to develop the technique of phase-space tomography applied to the EMMA injection line of the ALICE accelerator at the Daresbury Laboratory; to understand the requirements, capabilities and limitations of the technique; and to use it as a tool to investigate the effect of space-charge on the injected electron beam, both by computer simulation and by experimental measurements.
The detailed objectives arising from this goal may be categorised under two headings as follows:

Practical and Experimental Work

- to study the hardware requirements for tomography data acquisition, including the evaluation and test of improved screen imaging camera systems;
- to check that beam-line conditions and camera settings were optimised for tomography data collection;
- to plan, organise and carry out appropriate tomography experiments to collect screen image datasets, during scheduled ALICE/EMMA shift sessions;

Computer Development and Simulation

- to develop computer codes for
  (a) generating input data settings for running tomography scans;
  (b) processing experimental output data and reconstructing transverse phase-space distributions;
  (c) extracting parameters of interest by analysis of phase-space reconstructions;
- to compare the different reconstruction algorithms used in beam tomography;

- to benchmark the simulation codes used, in particular the functions they provide for incorporating space-charge effects, against analytical codes in simple predictable cases;
- to build detailed models of the diagnostics section of the ALICE beam-line using particle tracking codes;
- to model the full tomography measurement process, from the generation of realistic input particle distributions to the simulation of output screen images suitable for tomographic reconstruction;
- to use the models as a tool for exploring the influence of space-charge on tomographic measurements of phase-space, and for supporting experimental results.

1.1.1 Statement of Contribution to Accelerator Science

The work described in this thesis makes a contribution, which as far as is known is new and original, to the field of phase-space tomography, specifically in the application of this technique for the first time to the ALICE accelerator at the Daresbury Laboratory, UK. ALICE is a research machine which was designed for the development of the principle of energy recovery from the accelerated electrons, and is described further in Section 1.3.

Particular aspects of the work which should be highlighted include:-

Space-Charge Effects Space-charge is a term for the repulsive interaction between the similarly-charged particles in a bunch, and is stronger when they are in close proximity. A novel method of investigating space-charge effects in an accelerator beam-line is introduced, by making tomography measurements at separate locations in the line and then comparing the two sets of results to look for differences, as in Section 5.1.2. If other influences can be discounted, these changes may be ascribed to space-charge acting over the section of line between the two locations.

Normalised Phase-Space 'Phase-space' refers to the function of position x and momentum p_x which describes the dynamics of one or more particles moving in space, generally through the electromagnetic fields - or field-free regions - of a particle accelerator. In this work, the concept is extended by developing the idea of 'normalised phase-space' in the tomography of particle beams, where 'normalisation' is defined by a special transformation which depends on particular parameters of the beam. It turns out that working in normalised phase-space can have definite advantages over 'real' phase-space, in the quality of information in the distribution obtained by tomography. A fuller explanation is given in Chapter 6.

Correction Techniques Although they are the product of other work more fully described in [1], the new techniques of projection thresholding and background suppression by truncation of projections are referenced here, in Sect.3.1.4. Both of these methods reduce noise and artifacts and so improve quality in tomographic reconstructions, therefore impacting positively on the ALICE and EMMA projects.

Benchmarking of Codes Space-charge in ALICE has been previously studied in particle tracking code simulations such as those described in [2]. This is extended in the current project, which corroborates the evidence for measurable space-charge effects predicted by the code, by benchmarking against analytical calculations, under simplified conditions which are nevertheless relevant to the ALICE situation.

1.2 Modern Particle Accelerators

Particle accelerators have developed enormously both in size and power, from the earliest machines of Cockcroft and Walton in 1932 to the scale of the Large Hadron Collider (LHC), started up in 2008. At the same time, the range of application for accelerators has also grown from their origins in nuclear physics research, to include such fields as medicine, industry, and energy, as well as fundamental particle physics.

In all modern machines, the prediction of performance, in particular the properties of the accelerated particle beam, which usually takes the form of discrete bunches rather than a continuous uniform stream, is of great importance for successful operation. For this purpose, beam diagnostic instrumentation is provided to give the operator and the designer information on key parameters, to confirm that the machine is functioning to specification.

One of the basic parameters of the beam is the position of its centroid with respect to the middle of the vacuum pipe through which it travels. The transverse coordinates, conventionally denoted x (horizontal) and y (vertical), may be deduced from the electronic signal pulse induced instantaneously in the 2 pairs of electrodes of a Beam Position Monitor (BPM) embedded in the vessel walls, when a particle bunch, with its concentration of charge, passes that location. Time of flight may also be calculated for the transit of a bunch between BPMs. This is an example of a non-destructive diagnostic technique; however, to observe in detail how the particles within a bunch are behaving, other methods are required.

Wire scanners operate by stepping a thin stretched wire horizontally or vertically through the beam, while recording the current collected from the section of the beam incident on the wire. This offers a moderately non-interceptive means of profiling with limited resolution. Other examples of profiling devices include the Residual Gas Ionisation Profile Monitor [3, p. 33], which makes use of fluorescence due to interactions between the beam particles and the few remaining gas molecules in the vacuum vessel.

The preferred method for obtaining a high-resolution x-y beam profile is to intercept the beam with a fluorescent screen, which may consist either of powdered scintillator on a substrate, or a thin single crystal. With crystal screens, care must be taken not to exceed the safe beam current to avoid damaging or destroying them by heat load. Such an event risks incapacitating at least the affected section of the machine by contamination of the vacuum vessel with screen fragments.

An alternative offering better resistance to beam damage, but lower sensitivity, is the application of optical transition radiation (OTR) [3, p. 14], in which the imaging screen is made from thin metal foil such as $10\,\mu$m aluminium. Light is generated when a charged particle of any kind crosses a boundary between media of different dielectric constant ϵ. For a relativistic beam of energy E, the radiation is particularly useful in the case of electrons because it is concentrated conveniently into narrow cones of opening angle $m_e c^2/E$, where m_e is the electron mass and c is the velocity of light in vacuum.

Screens of both types are mounted on supports which may be driven mechanically into the beam when required. Some of the emitted light is collected by a charge-coupled device (CCD) camera mounted at right angles to the beam direction, as shown in Fig. 1.1. With the screen inclined at 45^o the image is a true, undistorted profile of the beam, integrated over the length of the bunch, or train of bunches. Cross hairs, which may be etched onto the screen, assist with beam location and facilitate the calibration of the optical system, from screen to camera sensor. Cameras often operate in relatively high radiation environments which degrade the CCD device as well as causing darkening of glass lenses. Either they are protected by lead shielding, viewing the screen via an indirect optical path of mirrors and lenses, or they are made as simple cheap devices, designed to be easily replaceable.

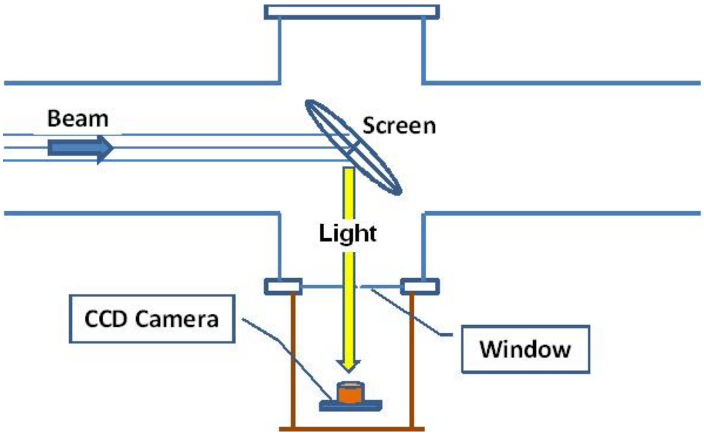

Figure 1.1: A plan view shows the typical configuration of a CCD camera viewing an imaging screen, as installed on ALICE. The screen is inside the vacuum chamber, the camera outside looking through a transparent window. Screen movement into/out of the beam is most commonly vertical, but horizontal at a few stations.

Although the light yield is usually very linear with beam intensity, accuracy will be reduced if there are even small areas of excessive brightness in the image, caused by saturation of particular CCD pixels, which have a limited storage capacity.

Another key measurement is the current of electrically-charged particles comprising the beam. This may be simply and conveniently determined by absorbing the beam in a block of conductive material, in a **Faraday cup** device. The shape is designed to avoid escape of any secondary emissions caused by collisions of the energetic primary particles. By integrating the current pulses detected, which may be fed to an oscilloscope for display, the charge represented by individual bunches of particles may be resolved, if the readout electronics are sufficiently fast.

1.3 The EMMA Concept

EMMA (Electron Machine with Many Applications), the world's first non-scaling Fixed-Field Alternating Gradient (ns-FFAG) accelerator, has been under commissioning at the Daresbury Laboratory of STFC since June 2010. EMMA is a 5.3 m diameter ring which contains 84 magnets, with 19 radio-frequency (RF) cavities to provide acceleration (Fig. 1.2) [4]. The magnets are special quadrupoles, aligned off-centre to provide a dipole field component for steering the electrons around the ring, as well as their primary role of focussing the beam. Successful acceleration was announced officially in January 2012 [5]. The **ns-FFAG** is a class of accelerator whose bending and focussing fields are kept fixed during acceleration, in contrast to the **synchrotron** design in which the fields must be progressively ramped up as the beam energy increases. In EMMA, even though the RF frequency is also fixed, its phase with respect

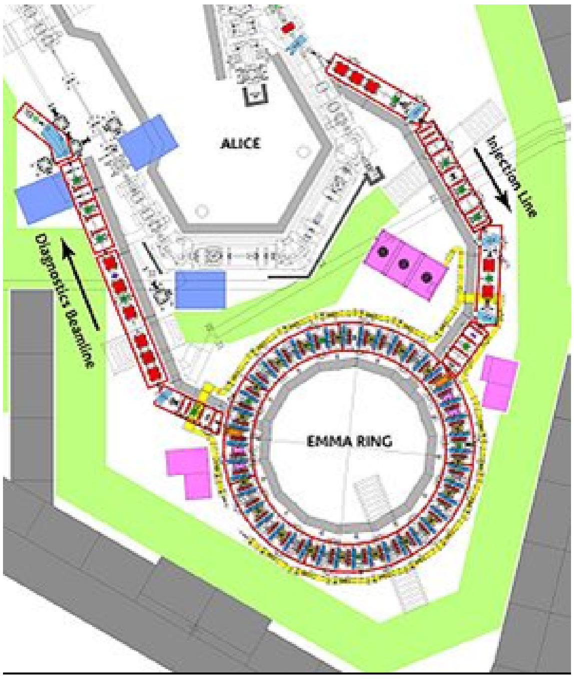

Figure 1.2: The layout of the complete EMMA complex is shown, including the link with the injector (ALICE), the EMMA ring itself, and the injection and extraction (here labelled 'diagnostics') lines.

to the beam is maintained as the time of flight remains almost constant with increasing energy. At the same time the machine has a large dynamic aperture, the orbit radius showing only modest growth while the momentum increases by a factor of 2 or more. EMMA demonstrates several novel features and has the potential for rapid acceleration in a small machine, although there are still many challenges. Devices using the same FFAG concept are anticipated to have applications in a variety of fields such as muon acceleration; used with protons, for more effective radiotherapy for cancer; and in nuclear power, as a driver for the Accelerator-Driven Subcritical Reactor (ADSR) design [6]. The injector for EMMA is the ALICE (Accelerators and Lasers in Combined Experiments) machine which can operate up to an energy of 35 MeV, but for EMMA provides an electron beam at a suitable injection energy of about 12 MeV [7]. The ALICE Project is an experimental test facility. Electrons from its 350 keV laser-driven photoinjector pass through an 8.35 MeV superconducting booster linear accelerator (LINAC) and into the main LINAC. After use in the experimental sections, most of the energy may be recovered as the electrons recirculate through the main LINAC again, and this energy becomes available for new electrons in the next cycle.

1.4 ALICE Diagnostics

The injection line to EMMA has been designed to extract the beam from ALICE through a dipole magnet, which when energised bends the beam out of the first ALICE straight, ST1. Shown in plan view in Fig. 1.3, it consists of an initial 'dog-leg' section, preceding a matching section which modifies the beam lattice parameters to suit the tomography section immediately following it [8]. This acts as a beam diagnostic which can measure the properties of the beam in some detail, prior to injection into EMMA.

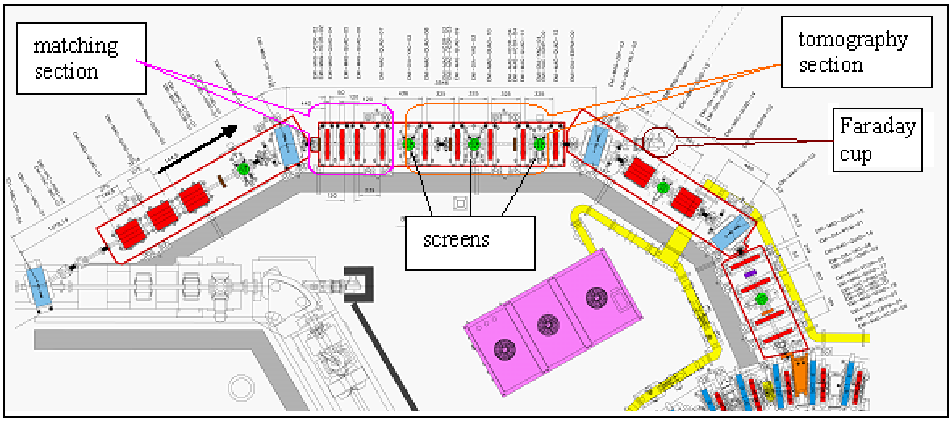

Figure 1.3: The EMMA Injection Line comprises dipole magnets (blue), quadrupoles (red) and screens (green). The matching and tomography sections are indicated, as well as the Faraday cup, to use which the 3rd dipole is de-energised.

The tomography section consists of two cells, each comprising a horizontally-focussing quadrupole magnet, a drift space (without fields), a defocusing magnet, and a further drift space, a configuration commonly described as a 'FODO' cell. Both cells have fluorescent yttrium aluminium garnet (YAG) crystal screens at each end (in Fig. 1.4 the quadrupoles are in red and the screen viewport is visible behind the plastic cover where the camera is normally mounted). Just before the tomography section, the matching section of four quadrupole magnets is located. A Faraday cup is also installed at the end of the straight, beyond the tomography section; to use it, the last dipole magnet of the straight is switched off, so that the beam continues into the cup instead of taking the bend towards EMMA. Through an amplifier, an oscilloscope is used to measure the pulse height from the cup, which is proportional to the charge within each bunch.

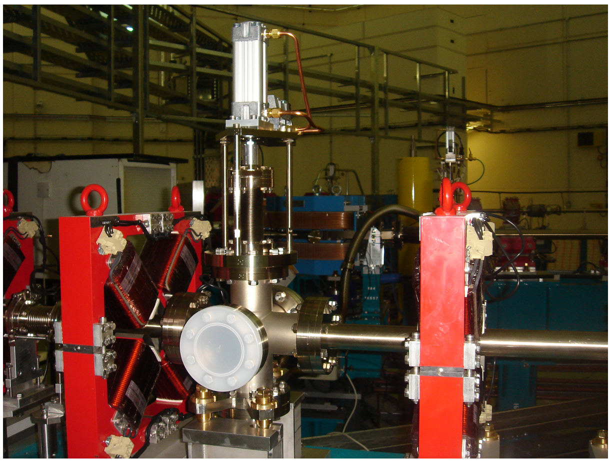

Figure 1.4: Part of the ALICE to EMMA Injection beam-line showing two quadrupole magnets (in red) and a screen station (between the magnets), with its camera removed and the viewport protected by a plastic cover. Above the screen station is the actuator and bellows for remotely raising the screen or inserting it into the beam.

1.5 Beam Diagnostics Methods

1.5.1 Principles of Transverse Linear Beam Dynamics

It is useful to first establish the theoretical basis for describing the motion of particles within the magnetic fields of an accelerator. For convenience we define a rotating curvilinear Cartesian coordinate system (x, y, s) where x, y are the transverse horizontal and vertical directions and s is the displacement measured longitudinally along the path of the beam as it traverses the beam-line. The analysis is simplified if we consider only those elements with 'linear' effects on the beam, to good approximation. This includes dipole magnets, with essentially constant field B_y between their poles, bending the beam in the x-direction; and quadrupoles, with field gradient $k = \frac{dB_y}{dx}$ focussing in the x-direction (or $\frac{dB_x}{dy}$ if focussing in the y-direction). Normal quadrupoles which focus horizontally always defocus vertically, and vice-versa.

The mathematical formulation of this motion, which incorporates the concept of a restoring force which can vary with displacement s, gives **Hill's Equation**:

$$\frac{d^2x}{ds^2} + K(s)x(s) = 0 \tag{1.1}$$

If K were constant, this would just describe Simple Harmonic Motion; in practice, it defines the 'betatron oscillations' of particles in the horizontal plane. There is a similar equation in 'y' for the vertical plane.

Solving Hill's Equation A solution to Eq. 1.1 which introduces the parameter $\beta(s)$ as the amplitude modulation, and $\phi(s)$ as the phase advance, with constants ϵ and ϕ_0

dependent on initial conditions, may be postulated:

$$x = \sqrt{\epsilon\beta(s)}\cos(\phi(s) + \phi_0) \tag{1.2}$$

By differentiating and substituting in Eq. 1.1, we find that the expressions for x and $x' = \frac{dx}{ds}$ are:

$$x = \sqrt{\epsilon\beta(s)}\cos\phi \text{ and } x' = -\alpha\sqrt{\frac{\epsilon}{\beta(s)}}\cos\phi - \sqrt{\frac{\epsilon}{\beta(s)}}\sin\phi \tag{1.3}$$

where $\alpha = -\frac{\beta'}{2}$. α and β are known as the Courant-Snyder (or 'Twiss') parameters. We find that for some defined α and β values (at a given s), if x is plotted against x' as ϕ goes from 0 to 2π, the result is elliptical, known as the 'phase-space ellipse'. At other locations on the beam-line, the ellipse will change in shape and orientation with β, but it is found that the area ($\pi\epsilon$) remains constant. ϵ is called the '**transverse emittance** and is a fundamental property of the initial beam as it is created. Its units are *metre–radians*, but it is more often quoted in *mm–mrad*.

Usually we are dealing with a large population of particles in a bunch, and the emittance is then defined as the area of that ellipse which contains a prescribed percentage of all the particles, as illustrated in Fig. 1.5.

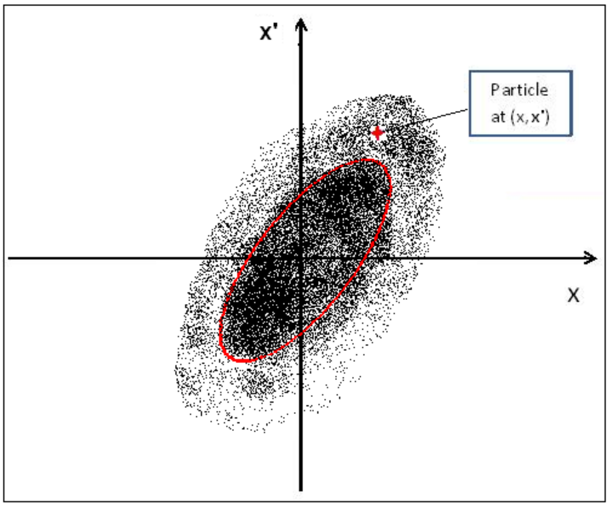

Figure 1.5: This is an illustration of a phase-space (x, x') plot for a bunch of particles at some beam-line position, showing the coordinates of one sample particle. The phase-space ellipse corresponding to the root-mean-square (RMS) emittance is overlaid on the plot (in red).

Matrix Formalism We can represent the transverse phase-space coordinates of a particle in matrix form $\begin{bmatrix} x \\ x' \end{bmatrix}$. The effect of each beam-line element i on the particle can then be expressed by defining a **transport matrix** M_i, for example $M_{\text{Drift}} = \begin{bmatrix} 1 & L \\ 0 & 1 \end{bmatrix}$

for a drift space and $M_{\text{TQuad}} = \begin{bmatrix} 1 & 0 \\ -\frac{1}{f} & 1 \end{bmatrix}$ for a 'thin' focussing quadrupole (where 'thin' implies that focal length $f = \frac{B\rho}{KL} \gg$ effective length L).

To calculate the new phase-space matrix at beam-line position s_2 given its known value at s_1, we have only to apply the full matrix M describing the combined effect of all the intervening elements between s_1 and s_2:

$$\begin{bmatrix} x_2 \\ x_2' \end{bmatrix} = M \begin{bmatrix} x_1 \\ x_1' \end{bmatrix} \tag{1.4}$$

The combined transport matrix M can be expressed simply as a product of the individual M_i matrices:

$$M = M_N M_{N-1} ... M_1 = \prod_{i=1}^{N} M_i \tag{1.5}$$

1.5.2 Practical Diagnostic Techniques

A number of standard methods are in common use by accelerator scientists to measure the Twiss parameters for the transverse phase-space of particles in a bunch. On ALICE, the techniques which have been regularly used include:-

Quadrupole-scanning As the current setting in a suitable quadrupole magnet is varied over a range, the changing beam shape recorded on a downstream screen is fitted to a Gaussian profile [3, p. 199]. The relationship between the Gaussian beam-width and the quadrupole magnet strength is analysed to extract the beam parameters of interest. This method is described in more detail later, in Section 3.2.1.

Slit scanning In the *single-slit* method [9], a series of beamlets are selected by moving a slit in steps across the beam. From the RMS size $\left\langle x_{n(rms)} \right\rangle$ measured at a screen at distance L downstream, the local divergence at slit position n is given by $\left\langle x'^2_{n(rms)} \right\rangle \propto \frac{\left\langle x^2_{n(rms)} \right\rangle}{L^2}$. The whole-beam divergence $\langle x' \rangle$, obtained from the weighted sum for all n beamlets, provides an approximation to the RMS normalised emittance by $\epsilon_{x(rms)} = \beta\gamma\sqrt{\langle x^2 \rangle . \langle x' \rangle^2}$. However, the method relies on assuming a well-behaved elliptical phase-space distribution, and on the beam image being a reasonable fit to a Gaussian function. Values in the range 5 - 10 mm-mrad have been obtained.

The *2-slit* technique is a variant of this method, used on ALICE [10]. Vertical slits 'A' and 'B' are separated along the beam-line by length L. The beam is first centralised on the 2 slits. Slit 'A' is scanned across the beam, measuring currents I_i in a Faraday cup, at a set of 10 positions x_i. A further scan of 'A' over x_i is made, this time also scanning the slit 'B' over a set of positions x_{ij} for $j \sim 10$ at each i, recording currents I_{ij}. From the x_{ij} and I_{ij} datasets, the beam centroids, the divergence, and ultimately the RMS horizontal emittance may be calculated, using Equation 3.1. Problems of the method include the time taken by the multiple slit-scans, and the measurement of small beam currents after attenuation by passing through the 2 slits.

'Pepperpot' measurement A metal plate perforated by a regular grid of fine holes intercepts the beam, generating a series of beamlets which propagate in field-free space, to create a pattern of profiles on a downstream screen [11, p. 249]. For a given screen distance L and estimated emittance ϵ, the hole spacing must be sufficient to avoid overlap of the beamlets, while still adequately sampling the beam area. In the simplified method as used on ALICE [10], a rapid estimate of the transverse emittance is calculated from $\epsilon_x = \frac{\Delta x \Delta u}{4\alpha^2 L}$, where Δx, Δu are the full widths of the beam and beamlet images respectively, and the coefficient α relates the full visible width Δx to the RMS width σ_x by $\alpha = \frac{\Delta x}{2\sigma_x}$.

Phase-Space Tomography The tomographic method covered in this thesis has the advantage that it can reconstruct phase-space without assuming its shape in advance; tomography is particularly useful for direct validation against the phase-space distributions predicted by simulation using particle tracking codes. Nevertheless, the standard tomography theory described in Section 2.1 does rely on some assumptions, notably that:- (a) particle dynamics in the accelerator lattice are linear, with no coupling between transverse horizontal and vertical motions; (b) space-charge effects between individual particles are insignificant, which is only strictly valid in low beam-current regimes.

Correction methods for these effects are available, however, and for accurate results must be applied if the assumptions do not hold. The theoretical background to space-charge is introduced in Section 1.9, and is considered in detail in Chapter 5.

Tomography has been implemented at a number of accelerators worldwide, including PITZ [12], UMER [13], SNS [14], PSI [15], Duke [16], BNL [17], KU-FEL [18].

1.6 Review of Reconstruction Techniques for Phase-Space Tomography

1.6.1 Computed Tomography

Tomography, which literally means 'writing a slice' (from the Greek $\tau o\mu o\varsigma + \gamma\rho\alpha\phi\eta\nu$), may be loosely defined as the process of reconstructing a sectional image through an object, given a set of projections of the object, each recorded at a different angle θ. Mathematically, a projection is the result of taking a series of line integrals of the density function through the object, perpendicular to a line making an angle θ with the x-axis (see Fig. 1.6 [19]). It is also referred to as the 'Radon transform' [20], after the mathematician who defined it. A set of projection data, built into a matrix in order of increasing θ is called a sinogram because of the superimposed wavelike patterns (see Fig. 1.7 [21], where the inset shows an example source object). Tomographic reconstruction is the process of recovering the original density function of an object by computation, from a set of its projections. It is equivalent to performing the inverse of the Radon transform.

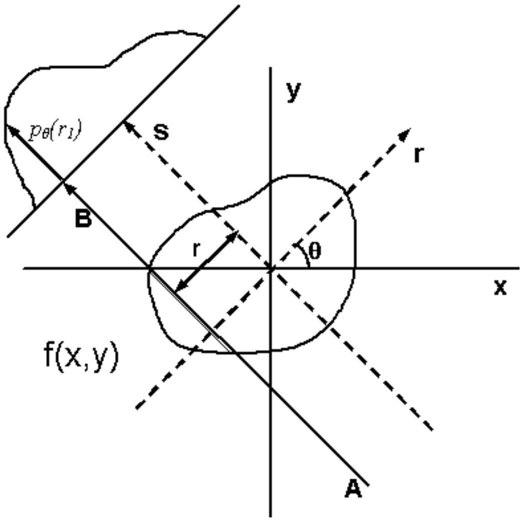

Figure 1.6: In parallel beam geometry, each projection is made up of the set of line integrals through the object, the data being collected as a series of parallel rays at positions r, across a projection at angle θ [19].

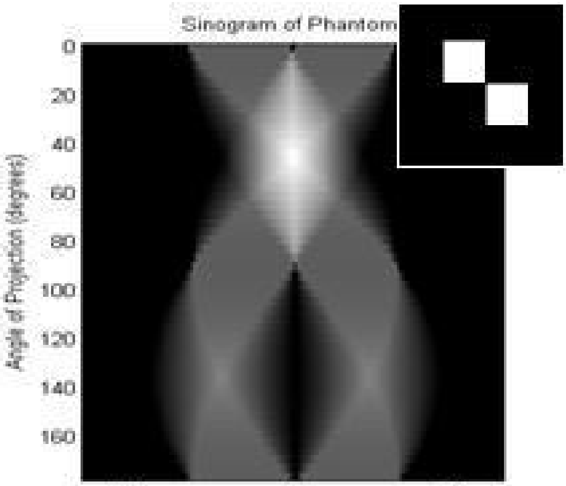

Figure 1.7: An example of a sinogram, formed from the Radon transform of the 'indicator function' of two squares (shown in the top R corner), taken at 50 equal angles spanning 0 to 180 degrees. Lighter regions indicate larger function values, black is zero [21].

One of its best-known applications is in X-ray Computed Tomography (CT), used in medicine (Fig. 1.8 [22]) to visualise slices through the human body. Specialised CT scanners operate by rotating a gantry, containing the X-ray source and diametrically-opposed detector arrays, around the subject, collecting 2-D projection data continuously during the scan. Dedicated computer hardware then simultaneously reconstructs multiple slices (Fig. 1.9 [23]), which become available for display almost immediately after acquisition. Slices may be viewed individually, or as a stack representing a 3-D volume.

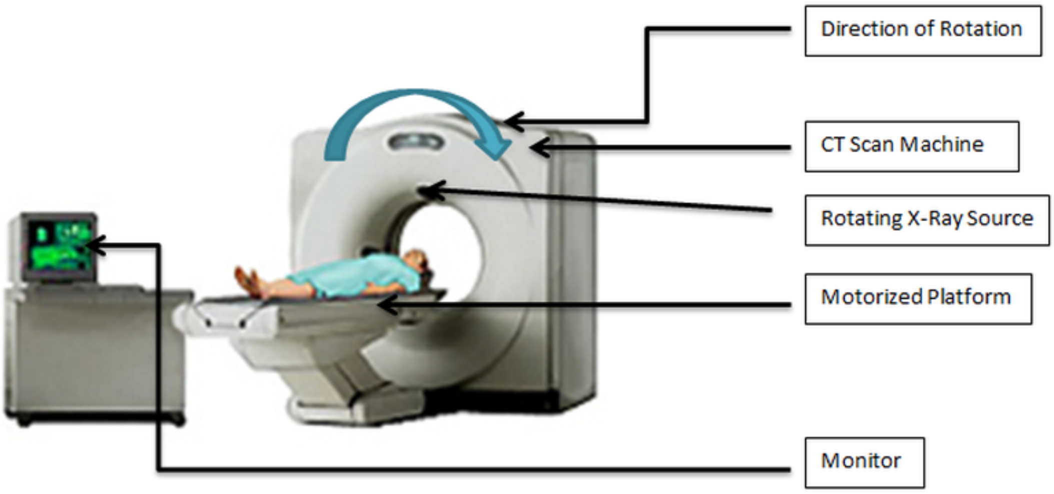

Figure 1.8: During a CT scan a patient is moved slowly through the machine, which has a rotating X-ray tube and opposed detectors in a curved array, simultaneously collecting data representing up to 256 slices through the body [22].

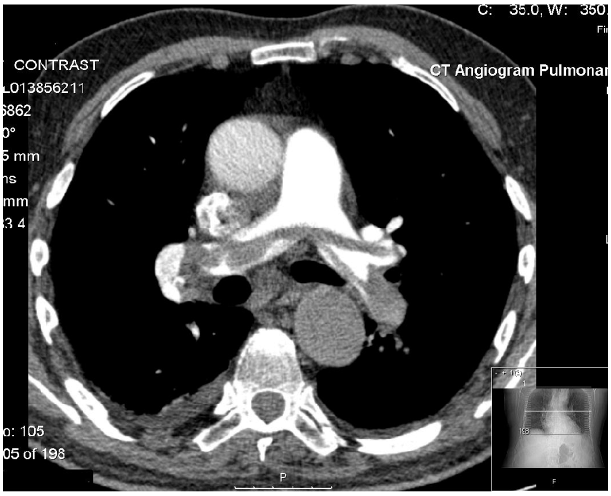

Figure 1.9: An example of a CT slice, this is a pulmonary angiogram, demonstrating a ‘saddle embolus’ (dark horizontal line) occluding both left and right pulmonary arteries (bright white triangle) [23].

1.6.2 Reconstruction Algorithms

In principle, tomographic reconstruction requires the calculation of the Inverse Radon Transform; in practice, however, this is not usually attempted directly, because the process is unstable when noise is present or data is imperfect.

Standard Method

The most commonly-used algorithm is known as Filtered Back Projection (FBP) [24]. This may be understood intuitively as the building-up of a reconstructed image by 'smearing out' (or backprojecting) each of the projections, taken at a different angle, across the plane so that they superimpose to create an approximation to the original. This is a simplification because the filtration step, carried out in the spatial Fourier domain, is key to obtaining an accurate result. FBP has been intensively developed for medical CT scanning and can be made to run very efficiently, especially on dedicated computer systems; indeed, processing may be started even before all projections in a scan have been completed.

Further details of the mathematical basis of the FBP algorithm are given in Section 1.7.

Alternative Methods

As well as FBP, there are other reconstruction techniques, the most important of which may be classified under the heading of 'iterative' algorithms. These work in an entirely different way from FBP. A typical iterative algorithm [25] follows steps such as:

1. Start with an initial estimate of the source distribution (e.g. uniform);
2. Forward-project this estimate along measured projections to work out what would have been measured if the estimate was correct;
3. Compare this to what was actually measured;
4. Update the estimate based on the comparison;
5. Continue iterating until some convergence criterion is met.

This class of method includes Maximum Likelihood Estimation Maximisation (MLEM) [25, 26], and Maximum Entropy Tomography (MENT) [27].

Basic Principles of MENT The Maximum Entropy Tomography (MENT) algorithm was developed at Los Alamos and was applied there to beam tomography [28]. It is based on the premise that from all possible solutions which can give rise to the observed projections, the most likely distribution is that with the highest entropy, that is, the least information content. MENT has the advantage of providing a better quality of result than methods such as FBP, where only a limited dataset is available as in the case of tomography with just 3 or 4 views. However, as it belongs to the class of 'iterative' techniques MENT can be computationally intensive and therefore slower, especially for larger numbers of views, unless it is efficiently coded. It is also susceptible to noise in the input data, which should be filtered before sending it to the MENT routine. Further details of the MENT algorithm will be found in Section 7.1.

1.7 Theory of the Filtered Back Projection Algorithm

The most popular tomographic reconstruction algorithm, which exploits its relationship with the Fourier Transform, is known as Filtered Back Projection (FBP) [24]. In brief, FBP takes the set of projections of the object and applies high-pass filtering in the spatial frequency domain, before 'backprojecting' the values of each projection (in polar or (r, θ) space) across the image space (x, y). This last step implies an interpolation due to the change in coordinate system from polar to Cartesian. The filtering stage is required to suppress the blurring which would otherwise degrade the reconstructed image, and it turns out to be computationally preferable to perform this filtering in 1-D before backprojection, rather than in the alternative order which would be to filter afterwards in 2-D space. Theory predicts that the ideal filter shape is a 'ramp' (Fig. 1.12) [24, p. 72], but in practice others are preferred where data is noisy, as it is in all real images. The algorithm for FBP has been summarised as follows [24, p. 62]:-

For each of the K projection angles θ, between 0° and 180°:

1. Measure the projection, $P_\theta(t)$ where t is the displacement along the direction r at angle θ (see also Fig. 1.6)
2. Fourier transform it to find $S_\theta(w)$ at frequency w
3. Multiply it by the weighting function $2\pi|w|/K$, in the frequency domain
4. Sum, over the image plane, the inverse Fourier transforms of the filtered projections (the backprojection process)

The theory behind these steps is illustrated below:-

1. The starting point is a set of projections in 1-D space of the (unknown) 2-D density distribution $f(x, y)$. Measuring a projection is equivalent to taking the line integrals at a series of discrete positions along a line making angle θ with the x-axis. Figures 1.10 and 1.11 show, as an example, one projection of a simple circle, taken to have uniform density for this illustration.

Mathematically, the parallel projection process can be expressed as

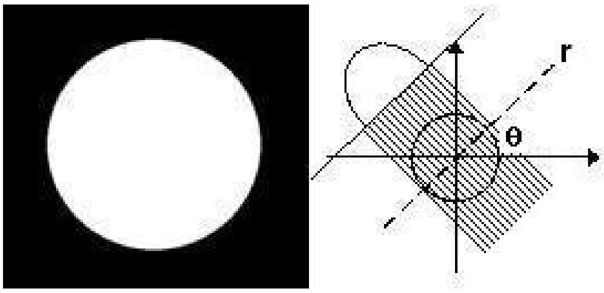

Figure 1.10: The parallel projection (R) of a simple circle with uniform density (L), which is a convenient test object, is shown at a particular angle θ.

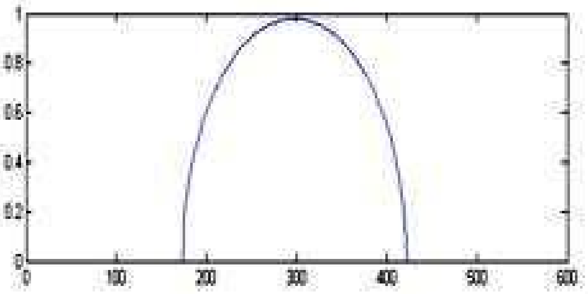

Figure 1.11: The projection of a circle has the same profile at any arbitrary angle, assuming that the axis of rotation is coincidence with the centre. Position r is plotted horizontally and intensity is vertical.

$$P_\theta(r) = \int_{-\infty}^{\infty}\int_{-\infty}^{\infty} f(x,y)\delta(x\cos\theta + y\sin\theta - r)dxdy \tag{1.6}$$

where δ is the delta function.
For computation, it is convenient to assemble the projections into a matrix (a 'sinogram', see Fig. 1.7) over all angles taken, each projection being sampled at the same discrete set of positions (i.e. displacements or values of r in Fig. 1.6) along the line at angle θ.

The unknown function $f(x,y)$ may be written in terms of its Inverse Fourier transform:

$$f(x,y) = \int_{-\infty}^{\infty}\int_{-\infty}^{\infty} F(u,v)e^{j2\pi(ux+vy)}dudv \tag{1.7}$$

where $F(u,v)$ is the 2-D Fourier transform. Under a change of coordinate system from (u,v) to polar (w,θ), we can rewrite as:

$$f(x,y) = \int_{0}^{\pi}\int_{-\infty}^{\infty} F(w,\theta)|w|e^{j2\pi w\rho}dwd\theta \tag{1.8}$$

2. The Fourier transform of the projection $P_\theta(r)$ is taken:

$$S_\theta(w) = \int_{-\infty}^{\infty} P_\theta(r)e^{-j2\pi wr}dr \tag{1.9}$$

3. This allows the 'Fourier Slice Theorem' to be applied, which states that a 1-D Fourier transform of a parallel projection is equal to a slice of the 2-D Fourier transform of the object: $S_\theta(w,\theta) = F(w,\theta)$. So in Eq. 1.8 we can write

$$f(x,y) = \int_0^\pi \int_{-\infty}^{\infty} S_\theta(w,\theta)|w|e^{j2\pi w\rho} dw d\theta \tag{1.10}$$

This represents a filter in the Fourier (frequency) domain, applied as a function of the form $|w|$ for $|w| < \frac{1}{2\tau}$ or 0 otherwise.

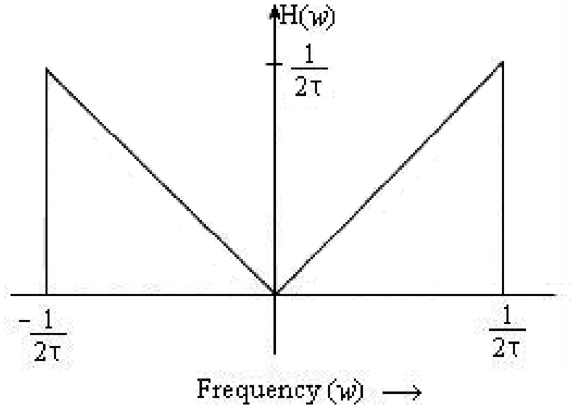

Figure 1.12: The transfer function of a filter in the frequency domain, with which the projections must be processed. It is given by $H(w) = |w|$, band-limited to $1/2\tau$, above which frequency there is negligible energy in the transformed projections.

An Inverse Fourier transform is applied to return to the spatial domain:

$$Q_\theta(r) = \int_{-\infty}^{\infty} S_\theta(w)|w|e^{j2\pi wr} dw \tag{1.11}$$

$Q_\theta(w)$ is called a 'filtered projection', $|w|$ giving the frequency response of the filter.

The filtered 1-D projection is spread out uniformly ('backprojected') across the 2-D region of image space which is the reconstruction plane. At every point (x,y) along a line of constant ρ, such as LM in Fig. 1.13, the projection makes the same contribution to the result, where $\rho = x\cos\theta + y\sin\theta$. The process of transform-filter-inverse-backproject is repeated for all projections in the set, that is for each θ value.

4. The sum of all backprojections Q is taken in image space, and interpolated onto a Cartesian grid (x,y). This constitutes the reconstructed image, represented by:

$$f(x,y) = \int_0^\pi Q_\theta(x\cos\theta + y\sin\theta)d\theta \tag{1.12}$$

It is clear from this example (Fig. 1.14) that to provide acceptable reconstructed image quality, a sufficient number of projections in the range $0^o \leq \theta < 180^o$ should be acquired.

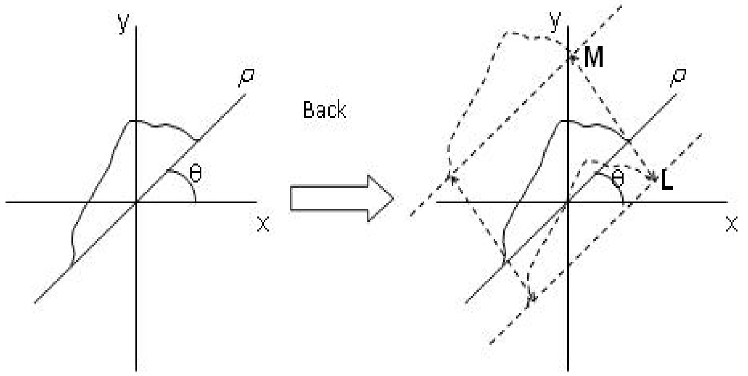

Figure 1.13: A filtered projection is smeared out over the (x, y) plane, along lines parallel to LM for the specific value of θ shown. At points on LM, this projection makes the same contribution. LM is perpendicular to the direction ρ.

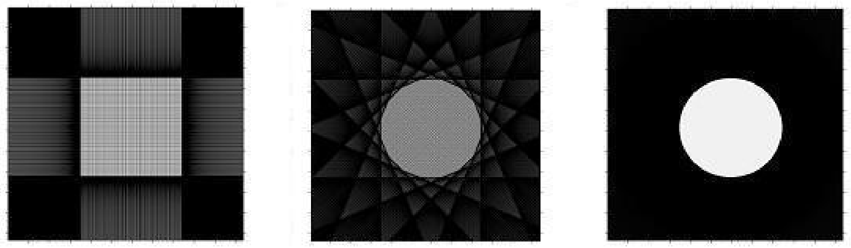

2 8 180

Figure 1.14: Reconstructions of the 'circle' test image (Fig. 1.10) show how increasing the number of projections taken (in this example 2, 8, and 180) very clearly improves the accuracy of the reconstruction and reduces extraneous artifacts.

Example of Reconstruction from a Test Phantom

FBP is capable of fast, accurate reconstructions, provided that a suitable input projection dataset is available, as the example below illustrates.

The **Shepp-Logan** phantom [29] was developed for the medical CT field as a simplified model of the human head, being entirely built of superimposed elliptical shapes having a range of densities and sizes (Fig. 1.15). It was intended to demonstrate the sensitivity of CT for detecting small low-contrast lesions. The choice of geometry allows for the analytical calculation, using simple codes, of the predicted projections at different angles, given the parameters of the constituent ellipses.

Figure 1.15: The Shepp-Logan phantom [29] is entirely composed of a superposition of simple uniform ellipses, which are specified by their centre coordinates, principal axis lengths, rotation angles and densities.

When assembled into a sinogram as in Fig. 1.16, this projection set may then be used as input for testing reconstruction algorithms.

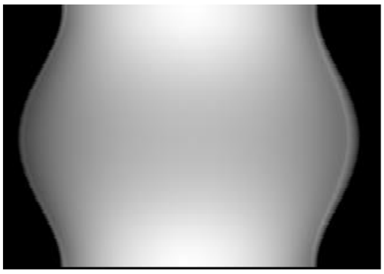

Figure 1.16: The sinogram shows a set of parallel projections of the Shepp-Logan phantom taken at 1^o intervals (180 projections). The vertical axis of the sinogram represents Angle, while the horizontal is Position.

An example of a typical result using the FBP method is shown in Fig. 1.17(a), which may be compared with the original in Fig. 1.15 . It is clear that although the outlines of the reconstruction are a faithful representation of the phantom, there is a noticeable loss of brightness, especially in the interior structures.

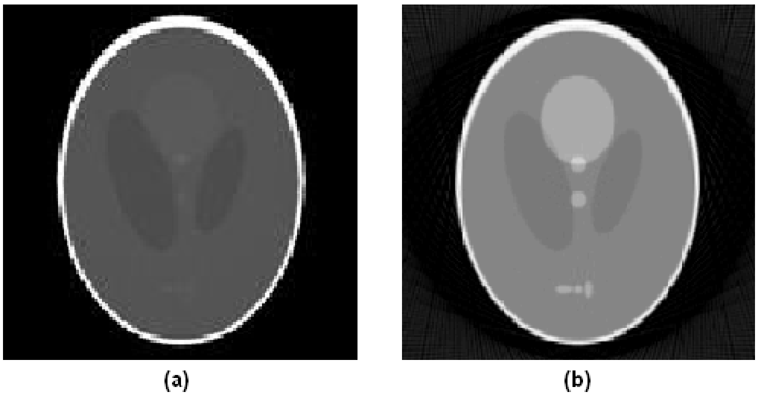

Figure 1.17: (a) Filtered Back Projection reconstruction of the Shepp-Logan phantom, based on the sinogram of Fig. 1.16. (b) Convolution Back Projection reconstruction of the same phantom, for comparison.

From this study [29], it was concluded that an improved algorithm, which is a variant of FBP called the 'Convolution Back Projection' method, could give more accurate results in terms of the reproduction of contrast levels, as can be seen in Fig. 1.17(b).

1.8 Review of Previous Work in Beam Tomography Research

Tomography has been utilised to investigate the phase-space of beams for over 30 years by a number of groups worldwide, and has therefore become a well-established and developed technique. Some representative examples in the field are reviewed here.

- A program based on the Maximum Entropy reconstruction method (MENT) was developed at Los Alamos [28], and was applied to non-interceptive beam diagnostics for prototype accelerators, using small numbers of projections [27].
- Phase-space tomography has also been developed, using the Filtered Back Projection (FBP) algorithm for reconstruction, at Duke University [16] with phosphor screens and the quadrupole tomography scanning method; both non-Gaussian and non-elliptical distributions have been considered.
- Similar studies with FBP on the Brookhaven Accelerator Test Facility [30] used 9 quadrupoles with a 1 mm beam-size, and included phantom studies to estimate experimental errors.
- Further work with the MENT algorithm has progressed in Germany at Deutsches Elektronen-Synchrotron (DESY), for the TeV Energy Superconducting Linear Accelerator (TESLA) Test Facility. It is described in a full mathematical treatment, together with code design, phase-space transformation theory and its application

to both transverse and longitudinal dimensions, including extensions for non-linearities [31].

- At the Paul Scherrer Institute (PSI) [15], an in-house code to implement MENT has been applied to proton beam-lines from 780 keV to 590 MeV, based on varying the optics at a single location, and adding noise reduction by FFT filtering on the measured beam profiles.
- The University of Maryland has relied on FBP to reconstruct 170-180 projection quadrupole tomography scans on intense beams at its Electron Ring (UMER) line, and includes space-charge correction as well as the comparison of experiment with simulation [13].
- More recently, work on the Cornell Energy Recovery Linac (ERL) electron gun [32] has been based on solenoids to give 18 rotation angles, using the Maximum Likelihood Expectation Maximisation (MLEM) reconstruction algorithm. Measured emittances have compared well with ASTRA [33] code simulations and with the alternative slit-screen method.

1.9 Basic Theory of Space-Charge in Particle Beams

A understanding of the theory of space-charge in simple geometries is necessary when considering its effect on measurable beam parameters, and an elementary treatment is therefore presented here.

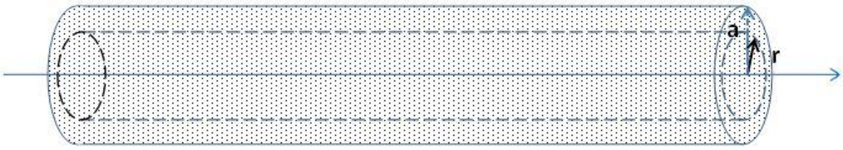

Figure 1.18: In a parallel circular beam, particles at density ρ are assumed to travel in a drift-space region without external fields, along non-intersecting paths at a constant distance from the axis. The cross-section is uniform and of radius a. Space-charge fields are calculated by considering a coaxial cylinder of radius r.

The simplest space-charge model, which is useful in developing the basic theory, is that for a parallel circular-section uniform beam of radius a, of particles with equal energy, coasting in a drift space without external fields (Fig. 1.18). Any effect of the vacuum tube containing the beam is ignored in this analysis, by assuming either that it has infinite conductivity, or that its aperture is large compared with the beam diameter. Gauss' theorem $\int \overrightarrow{E}.\overrightarrow{n}\,\mathrm{d}A = \sum_i \frac{q_i}{\epsilon_0}$ may be applied to determine the flux of the electric

field E due to the charges q_i enclosed, valid at points either inside or external to the beam, where ϵ_0 is the permittivity of free space.
If N is the number of particles per unit length, each with electronic charge q, enclosed by a cylindrical surface of radius r coaxial with a beam of charge density ρ, then

$$\rho\pi r^2 = \frac{Nq\pi r^2}{\pi r^2} = Nq \tag{1.13}$$

Applying Gauss' Theorem, we have the radial electric field

$$E_r = \frac{Nqr}{2\pi\epsilon_0 a^2} \text{ for } r \leq a \text{ or } E_r = \frac{Nq}{2\pi\epsilon_0 r} \text{ for } r > a \tag{1.14}$$

From the electric field we can deduce the force on a single electron of rest mass m_0, which when included in the general equation of transverse motion, in the horizontal (or x) direction, gives Hill's equation with space-charge (which may be compared with Eq. 1.1):

$$x'' + k(s)x = \frac{E_x q}{m_0 c^2 \gamma^3 \beta^2} \tag{1.15}$$

where $k(s)$ is the focussing strength, dependent on position s along the beam direction, β and γ are the relativistic factors, and c the speed of light. Substituting for E_x from Eq. 1.14, and rearranging, gives

$$x'' + (k(s) - \frac{q^2 N}{2\pi\epsilon_0 a^2 m_0 c^2 \gamma^3 \beta^2})x = 0 \tag{1.16}$$

which may be simplified to

$$x'' + \left(k(s) - \frac{K}{a^2}\right)x = 0 \text{ where } K = \frac{2I}{I_0 \beta^3 \gamma^3} \text{ is the `perveance'} \tag{1.17}$$

In the definition of K, $I = Nq\beta c$ is the beam current, and $I_0 = \frac{4\pi\epsilon_0 m_0 c^3}{q}$ is the characteristic (or $'Alfvén'$) current $\approx 17 \times 10^3$ A.

The negative sign of the second term $-\frac{K}{a^2}$ in Eq. 1.17 indicates that space-charge always adds a *defocussing* element to the transverse dynamics.

The very strong dependence of the K term in Eq. 1.17 on the relativistic factors β, γ implies that for highly relativistic, energetic beams, space charge has a rapidly diminishing effect as $\gamma = E/m_0c^2$. The effect on the electric field shape, seen by other particles in the bunch, is a flattening into the plane perpendicular to the longitudinal direction of motion, while the magnetic force tends to cancel that due to the electric field (Fig. 1.19).

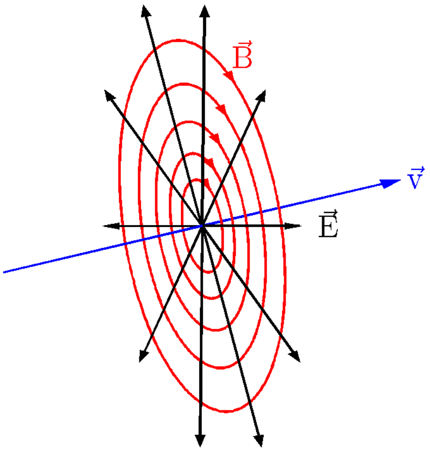

Figure 1.19: Whereas a stationary particle has an isotropic field, at highly-relativistic energies the electric field $\overrightarrow{E}$ of a particle, as experienced by neighbouring particles, becomes flattened perpendicular to the velocity $\overrightarrow{v}$.

Corresponding to Eq. 1.17 but applying more generally to bunches of particles, there is an 'envelope' equation to describe the development of the overall beam size a, which includes a term for the emittance:-

$$a'' + k(s)a - \frac{\epsilon^2}{a^3} - \frac{K}{a} = 0 \text{ where } \epsilon \text{ is the emittance} \tag{1.18}$$

When $\epsilon^2 \gg Ka^2$ the beam is said to be *emittance dominated*; if $\epsilon^2 \ll Ka^2$ it is *space-charge dominated.*

A study of the implications of operating the EMMA Injection Line at 35 MeV, instead of at a typical EMMA injection energy of up to 20 MeV [8], concluded that there would be no space-charge problems at a bunch-charge of 80 pC. This is however significantly higher than the energy of 12.5 MeV planned for beam tomography studies.

Using typical EMMA injection beam parameters of Energy = 12.5 MeV; Bunch Charge = 80 pC; Bunch Length = 2 mm; Bunch Radius = 1.2 mm, it is found that the condition for space-charge effects becomes

$$\frac{\epsilon^2}{Ka^2} = 5.8, \text{ which is } > 1 \text{ but not } \gg 1 \tag{1.19}$$

This indicates that the beam is expected to be 'emittance-dominated' but that space-charge effects cannot be excluded.

1.10 Overview of Contents of Chapters

The remaining chapters are briefly previewed here:-

Chapter 2 opens by relating reconstruction theory in real space to the tomography of phase-space in accelerator physics. The experimental programme for ALICE tomography is then introduced, broken down into phases. The first phase includes screen camera requirements definition and optimisation checks, the generation of input data for tomography scans, the development of a protocol and software processing steps for both multi-screen and quadrupole tomography scan methods. Initial results for horizontal phase-space are presented, with illustrations of the benefits of filtration. The second phase introduces the extension to vertical phase-space tomography, also explaining the significance of dispersion and its measurement, before presenting the results of an early variable bunch-charge experiment. It concludes by reviewing the possible implications of the work for the EMMA project.

Chapter 3 considers the derivation of beam parameters ϵ, α, β based on 2^{nd} moments analysis of the phase-space distribution, and the benefits of image data rebinning. The fitting of ideal Gaussian distributions to measured data is described, and raw results compared with fitted. Further corrections to improve reconstructions, thresholding and projection truncation, are explained. Comparison is made with another standard analysis method, 'quadrupole-scan beam-size fitting', giving an elementary treatment of its theory. The chapter ends by comparing tomographic results for the beam parameters with those from previous measurements using other methods, and with simulations from earlier work.

Chapter 4 introduces the modelling of the tomography beam-line using the particle-tracking code GPT. Essential theory underlying the code and its implementation of space-charge effects is given, and a simple demonstration of space-charge induced beam divergence is shown. A benchmark, set by calculating beam radius space-charge growth analytically, is compared directly with equivalent results from GPT modelling. The GPT user and file interfaces are explained in the context of data exchange with external programs. A detailed GPT model of the tomography beam-line is described, with its use for a systematic study of the dependence of differential beam-size (between high and low bunch-charge) on quadrupole current and screen position, and results are discussed. A convergence check is made to give the minimum particle number per bunch for reliable GPT outputs. A complete model of the tomographic measurement process is then built around GPT, with a discussion of methods of specifying initial particle distributions, based on experimental data. Inputs to GPT are validated against outputs, comparing beam parameters from internal GPT functions with values from independent external analysis.

Chapter 5 continues the description of tomography experiments at the third phase, with a solution to the issue of camera CCD saturation using optical filters. The 'comparative' method of tomography scans is devised, to attempt to demonstrate dependence of horizontal phase-space on bunch-charge over a section of beam-line. After explaining input preparation, results are shown for each quadrupole scanned, over the same range of charges, giving both the raw and the Gaussian-fitted distributions. The fourth phase is based on a new proposal for ALICE experiments, similar to Phase 3 but this time including vertical phase-space and hence new quadrupole tomography scans. Remote filter-changing is added to tomography camera systems. All results for both axes (x) and (y) are displayed. From Phase 3 data, an analysis of the dependence of horizontal emittance on charge is plotted, first for each quadrupole separately and then as a combined plot. Twiss parameters are also plotted and conclusions are drawn. A similar analysis is made of the Phase 4 results, which are directly compared with tomography from simulated GPT datasets. The MENT algorithm is applied to an investigation of anomalies discovered in the 'comparative' measurements of vertical phase-space.

Chapter 6 opens with an introduction to the concept of 'normalised phase-space' and its links to phase advance between fixed screens, relating this to ALICE tomography. Ways of predicting the Twiss α, β values to construct the normalisation transformation matrix are described. Examples comparing 'real' and 'normalised' phase-space are shown and some limitations discussed.

Chapter 7 introduces the Maximum Entropy (MENT) algorithm by outlining its mathematical principles. For the reconstruction of '3-screen' tomography data, comparisons are made between FBP and MENT results. Some possible problems with the reliability of MENT are raised.

Chapter 8 is the conclusion, opening with a general summary before detailing each chapter. Overall conclusions on the success of the project are made. It finishes with a discussion of further possible work and wider applications, under the three headings of:-

- objectives not met;
- extensions to other situations;
- new ideas.

The **Appendices** cover additional material referred to in the main chapters and likely to be of some interest, but not essential for a general understanding. It includes further notes on an example of a model of camera suitable for tomography; a procedure for camera focus setting, with depth-of-field calculation and results; lists of the experimental and simulated data runs; details of the computer processing steps from raw images to phase-space reconstructions; and a description of a freely-available implementation of the MENT code, with test outputs.

A **Bibliography** is the final part, with references to all cited papers, proceedings, manuals and other publications.

1.11 Summary

This chapter has introduced the project by setting out its main objectives, both for the experimental and for the simulation aspects of the work. Particular contributions made to the field of accelerator science are highlighted, specifically in space-charge effects; normalised phase-space; reconstruction correction; and tracking code benchmarking. Modern particle accelerators and their important diagnostic techniques are reviewed and the local ALICE and EMMA projects are introduced, with reference to the specific beam diagnostics on ALICE, especially in phase-space tomography. The principles of computed tomography are briefly described, with the two principal classes of reconstruction algorithm: i) Filtered Back Projection (FBP) and ii) Iterative methods, using MENT as an example.The mathematical theory of FBP is treated in a simplified manner, and basic space-charge theory in particle beams is outlined. Finally a full chapter-by-chapter overview of the remainder of the work is presented.

Chapter 2

Phase Space Measurements at ALICE

Introduction

Phase-space tomography has a theoretical basis which is similar to other applications of tomography. In this chapter, the relationship between tomography in real two-dimensional space and in the transverse phase-space of a particle beam is established. The experimental methods developed to prepare and carry out tomographic measurements on ALICE are then detailed, followed by results of the initial investigations using these methods.

2.1 Relationship between Real-Space and Phase-Space Tomography

In accelerator physics, we are interested in the properties of a population of particles in the beam as characterised by its distribution in phase-space, that is, the relationship between transverse horizontal displacement x and its gradient (or divergence) $x' = dx/ds$, as a particle moves in the direction s down the beam-line. It turns out that there is a direct analogy between 'normal' tomography in real-space, where the density function $f(x, y)$ for a slice through an object may be recovered from measurements of its projections at a range of angles θ, and the equivalent distribution in phase-space, $f(x, x')$. The latter is recoverable from a set of projections onto the x-axis of transverse beam profiles, with respect to effective 'rotation' angles. We can apply exactly the same reconstruction techniques, as described in Section 1.7, once some simple relationships have been established.

Deriving the Parameters relating Phase-Space to Real-Space Distributions

The basic theory necessary to understand and implement tomography in phase-space is presented here, in three parts. Further details will be found in [16].

(a) Rotation of Projections

In phase space, the effect of beam-line elements such as quadrupole magnets (focussing and defocussing), and drift spaces, may be treated as simple linear transformations on the $f(x, x')$ distribution, usually represented in matrix notation as already described in Section 1.5.1.

$$\begin{bmatrix} x_2 \\ x_2' \end{bmatrix} = M \begin{bmatrix} x_1 \\ x_1' \end{bmatrix} \text{ where } M = \begin{bmatrix} R_{11} & R_{12} \\ R_{21} & R_{22} \end{bmatrix} \tag{2.1}$$

(Note that in Eq. 2.1, matrix multiplication with M is implied, and M is required to be non-singular.) As a simple example, a drift space of length L is represented by the matrix

$$M_{\text{Drift}} = \begin{bmatrix} 1 & L \\ 0 & 1 \end{bmatrix} \tag{2.2}$$

The effect on the distribution is a **shear** in the $+x$ direction. This may be illustrated for a hypothetical rectangular distribution of size [1,1] based at (0,0):-

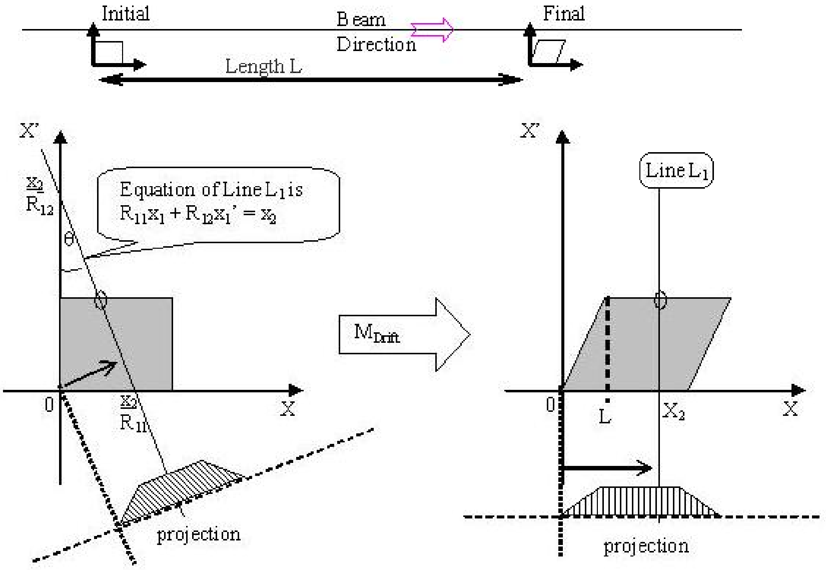

Figure 2.1: Considering the transformation of the line L_1 due to matrix M, the *rotation angle* θ may be derived geometrically from the equation of L_1 before the transform (in the Left-hand figure).

The matrix multiplication in Eq. 2.1 gives the equation of line L1 in Fig. 2.1 as

$$R_{11}x_1 + R_{12}x_1' = x_2, \text{ of the form } \frac{x}{a} + \frac{y}{b} = 1$$

$$\text{with gradient given by } \frac{b}{a} \Rightarrow \frac{R_{11}}{R_{12}} \tag{2.3}$$

Therefore the effective tomographic rotation, θ due to the transformation is obtained from the reciprocal of the gradient, so that

$$\tan\theta = \frac{R_{12}}{R_{11}} \tag{2.4}$$

The result in Eq. 2.4 can be shown to apply to the general non-singular transfer matrix M, representing the combined effect of beam-line components as calculated by Eq. 1.5 [13]. The matrix elements R_{11}, R_{12} then become functions of parameters such as magnetic length l and field gradient g for quadrupole magnets, and length L for drift spaces, depending on the arrangement of these components in the beam-line.

(b) Scaling of Projections

The second required relation is the scale factor s, which relates the projection of phase-space after transformation to the original projection of the distribution. This factor maps the effect on the grid spacing, which is the basis for the positions at which discrete measurements of the projection are taken, when the transformed phase space distribution $f_2(x, x')$ is related to the original distribution $f_1(x, x')$.

Referring again to the line L1 on the Left-hand side of Fig. 2.1, the value of s may be derived from trigonometric considerations as shown in Fig. 2.2:-

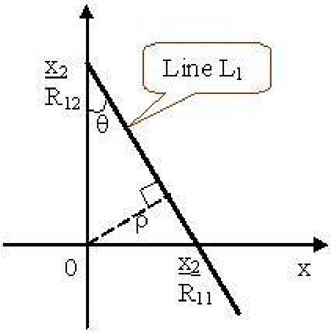

Figure 2.2: The *scaling factor s* describing how a projection is stretched by the transformation, is derived geometrically, by relating a position x_2 back to its corresponding value ρ in the projection before it is transformed by matrix M.

The equivalent displacement ρ, in the original distribution, of x_2 in the transformed distribution is given by

$$\rho = \frac{x_2}{R_{12}} \sin\theta \tag{2.5}$$

or $\rho = \frac{x_2}{s}$ where s is defined as

$$s = \frac{R_{12}}{\sin\theta} = \sqrt{(R_{11}^2 + R_{12}^2)} \tag{2.6}$$

using the relation for tan θ in Eq. 2.4.

As shown in Fig. 2.3, integration over the distributions must give the same result for the total number of particles:

$$\int f(\rho, \theta) d\rho = \int A(x_2) dx_2 = \int A(x_2) \frac{dx_2}{d\rho} d\rho \tag{2.7}$$

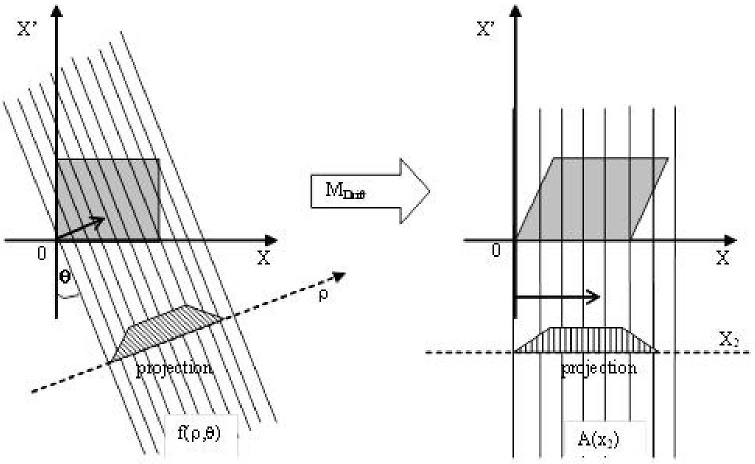

Figure 2.3: The phase-space distribution before transformation is integrated along the ρ direction, and compared with the integral afterwards, along x_2. From this mapping, the scaling factor s arises.

Using the definition $s = \frac{x_2}{\rho}$ from Eq. 2.5, $\int f(\rho,\theta)d\rho = \int sA(x_2)d\rho$
Therefore the projection of phase-space is

$$f(\rho,\theta) = sA(x_2) \tag{2.8}$$

where $A(x_2)$ is the projection after transformation.

(c) Equivalence of Real and Phase-Space Projections

The projection onto the x-axis of the beam profile in real (x, y) space is $\int_x^{x+\delta x}\int f(x,y)dxdy$, which may be equated with $\int_x^{x+\delta x}\int f'(x,x')dx'dx$ the equivalent projection in (x, x') space, as they are just 2 alternative views of the same population of particles in the small spatial interval $[x, x+\delta x]$, illustrated in Fig. 2.4. This implies that we need only measure the projection in (x, y) space to have the projection in (x, x') space, which would not otherwise be directly measurable.

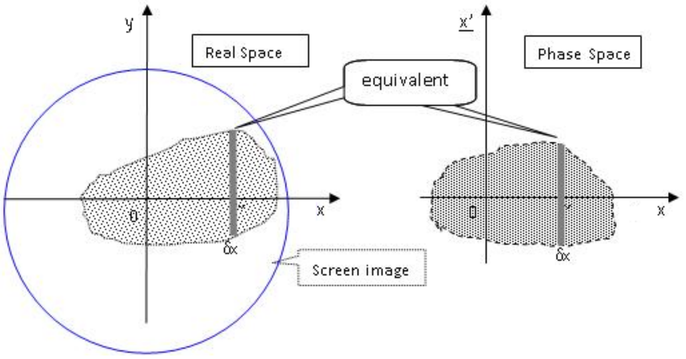

Figure 2.4: Consideration of the x-projections of a small interval δx in real-space and in phase-space shows that the projections can be equated. They represent alternative views of the same population of particles.

In practice, beam intensity (x, y) profiles are obtained from installed fluorescent phosphor screens or metallic Optical Transition Radiation (OTR) foils, appropriately positioned around the accelerator ring, which are driven into the beam path as required. As described earlier in Section 1.2, screen images at each location are acquired on suitable installed CCD cameras.

From these images, projections onto the x-axis (or y-axis) may be derived, and associated with values of θ and s calculated as above from the known transport matrix M.

Together, this information is sufficient to construct a sinogram from the projection set, and therefore to run a reconstruction algorithm to recover the (x, x') (or (y, y')) distribution; both FBP and iterative (e.g. Maximum Entropy) methods have been successfully used by a number of different accelerator research groups, and are reported in [13, 15, 16, 30, 32, 34].

2.2 Experimental Methods for Beam Tomography

Experiment Planning As part of the programme for 'Accelerator Physics' within the ALICE beam-time schedule, a number of experiments were planned and carried out on allocated shifts. Tomographic studies require, in general, exclusive access to the machine, because of the specific magnet settings demanded and also the destructive nature of 'interceptive' imaging where fluorescent screens are used, which prevents the use of the beam downstream. These experiments have provided invaluable information for the development of the technique, but have also yielded useful beam parameter data complementary to other diagnostic methods in routine use on ALICE. As the diagnostic beam-line used for tomography is also designed for injection into EMMA, as shown in Fig. 2.5, it was also convenient to perform tomography experiments during the time blocks allocated to EMMA, in between EMMA experimental shifts. This had the beneficial side-effect of maintaining the machine in continuous operational status during times when it would otherwise be idle, thus promoting better stability.

The planning of all experiments was carried out by the author, in consultation with the ALICE operations manager and the Accelerator Physics group leader. Dr K Hock provided guidance in the general direction of the studies, and suggested methods for the detailed space-charge investigations. Although the vast majority of the tomography data was taken on dedicated shifts summarised in Table 2.1, some images usable for '3-screen' tomography processing (detailed in Chapter 7) were also acquired incidentally, from data collected during other experiments. Besides the author, the team always included a 'key commissioner' to lead the shift, ensuring correct set-up of the accelerator and taking essential safety responsibility.

Total No. of Dedicated Shifts used	15
Shifts on which data was taken	12
Shifts producing referenced datasets	9
Total Hours spent on tomography scanning	35.5

Table 2.1: Of the total shifts used, not all yielded useful data because of equipment breakdowns or software issues. Datasets referenced herein (see Table B.1) have been selected from all the data taken. The duration of each tomography scan (typically ∼160 images) was about 20 minutes.

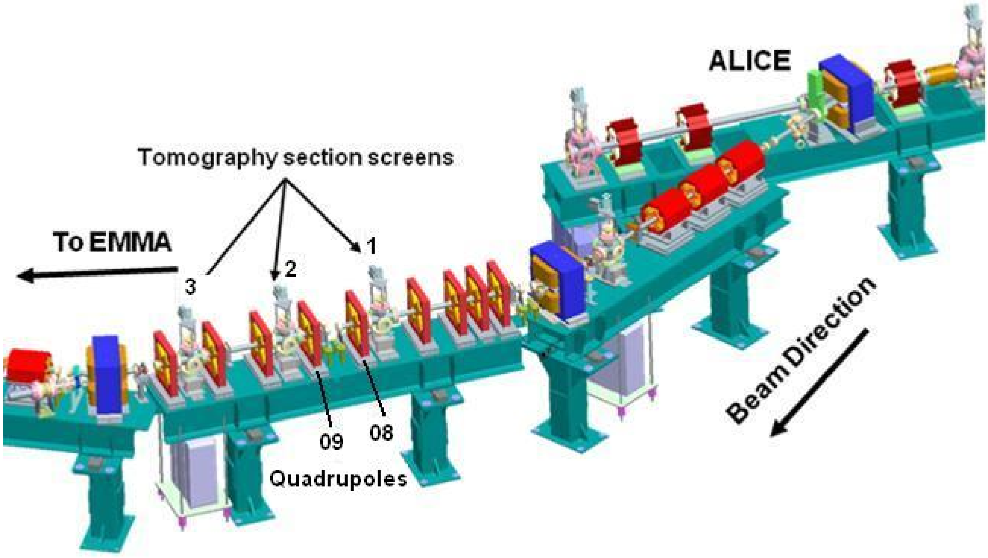

Figure 2.5: For EMMA, the beam is diverted from ALICE into the injection line by a dipole magnet (in blue, at Top Right). The tomography section has 3 screens for beam imaging, with quadrupole pairs between; a pair QUAD-08 and QUAD-09 is identified.

The experimental tomography which has been undertaken may be conveniently broken down into several logical phases:

1. Proof of Concept Experiments.
   Early ‘proof of concept’ work, including the development and testing of methods and processing software, and an initial study of desirable requirements for imaging hardware.

2. Quantitative Measurements.
   Experiments to demonstrate the usefulness of tomography in beam tuning by obtaining quantitative results, also extending the method to vertical phase-space and multiple bunch-charges.

3. Detailed Space-Charge Experiments.
   More detailed investigations to look for space-charge effects and their dependence on bunch-charge and beam energy.

4. Further Space-Charge Studies.
   Follow-on space-charge studies with quadrupole tomography scans, in both horizontal and vertical phase-space, supported by concurrent simulation work using particle-tracking codes.

In this chapter, the experimental methods used are described, under the headings of the first two of the phases defined above. Initial results are presented, but a detailed treatment is postponed until after Chapter 3, which describes the analysis techniques in more detail. The latter two phases, which deal particularly with space-charge investigations, are covered later in Chapter 5.

2.3 Proof of Concept Experiments (Phase 1)

At Phase 1, preferred imaging camera hardware requirements were established, with reference to existing installed screen cameras; performance testing procedures were developed for cameras, to use in the laboratory and with beam; computer software methods were formulated for generating phase-space tomography input data and processing the output; protocols were written for set-up of the beam before experiments; and first outputs were used to improve post-processing and display of results.

2.3.1 Camera Requirements for Tomographic Imaging

Camera performance is a key factor influencing the quality of the beam images, and hence the reconstruction; the essential and desirable features specified in Table 2.2 have been derived by reference to other projects [35], and from experience with the original screen cameras as used on ALICE, which are illustrated in Fig. A.1(a). Further information will be found in [36–39].

To meet these requirements, three options for providing cameras to acquire beam profiles for tomography were developed:

1. Modify/Enhance Existing Cameras.
   The basic ‘ALICE’ type in use has few customisable features; in particular there is no manual gain control, although Automatic Gain Control (AGC) has an ON/OFF selector. Interchangeable optical filters could be fitted in front of the lens, to control saturation in images.

2. Replace selected cameras by a compatible type with more suitable specification.
   No major modifications to camera housings and cabling are required, especially if from the same manufacturer; it may be possible to retain existing acquisition software, with few changes.

Feature	**Reason**	**Notes**
Selectable Gain Control	Optimise use of dynamic range while avoiding saturation	Control in software
Interchangeable Lenses	To provide magnification steps	e.g. C-mount
Optical Zoom	Maximise filling of screen pixels with image of beam (diam $\sim$3mm @ 6σ)	
Variable Aperture	Using Iris control, for intensity adjustment	To f1.8
CCD Bit Depth	Related to the required Signal to Noise Ratio (SNR)	$\geq$ 10-bit preferred
Exposure Triggering	Accuracy/reproducibility of exposure for image quality	Use ALICE laser pulses
Desireable:		
Remote Focussing	To facilitate setup procedure	
Radiation Hardness	Low Background, maintain quality	Shielding required?
Other Considerations:		
Spatial Resolution (Nyquist Criterion)	$\frac{Number of Projections, nproj}{Number of Positions, npos} \sim \frac{\pi}{2}$	Ref. [24] ch5 p186

Table 2.2: Essential and desirable features of an ideal beam imaging camera for phase-space tomography are listed, as a guide to the selection of options for upgrade or replacement of existing cameras.

3. Fit high-specification camera(s) selected for optimum performance.
   Significant redesign of mountings may be required; acquisition systems may need substantial modification; further spares are needed, and it may be prudent to retain fittings and wiring for the current cameras, in case replacement at short notice is required; however, the cost penalty makes their use at all screen locations unlikely.

Considering all requirements, the third option was preferred for the ALICE tomography section; but for initial commissioning, existing ALICE-type board cameras already fitted to the tomography section screens were to be used, while planning the phased introduction of higher-specification cameras. This would allow for the adaptations necessary to replace ‘standard by ‘high-specification cameras, including:

- a new camera mounting tube to allow a direct fit to the screen viewport;
- a fine focus adjuster adapted from current ALICE practice;
- revisions to the LED board, which illuminates the screen in the absence of a beam.

Additional networking to control ‘high-specification tomography cameras was also planned. Software running over the network would allow exposure to compensate for changes in beam intensity, as this varies with both photoinjector laser parameters and magnet settings around the ALICE ring. New cameras could also be triggered on the laser pulse so that exposures were synchronised to the beam repetition rate; whereas the existing cameras acquired asynchronously, relying on multiple exposures to ensure capturing a beam image.

Camera Performance Testing Procedure

The output data of a test is useful in several ways: in comparing individual cameras and lenses; as a benchmark for studies of CCD ageing due e.g. to radiation damage; and in setting camera controls for optimum resolution.

Standard Procedure for Camera Performance Testing The method used is based on a photographic quality optical test card to the ISO 12233 standard [40]. Images of the card taken with the prototype 'high-specification camera assembly are analysed for Spatial Frequency Response (SFR) with the 3rd party MATLAB software 'sfrmat2' [41].

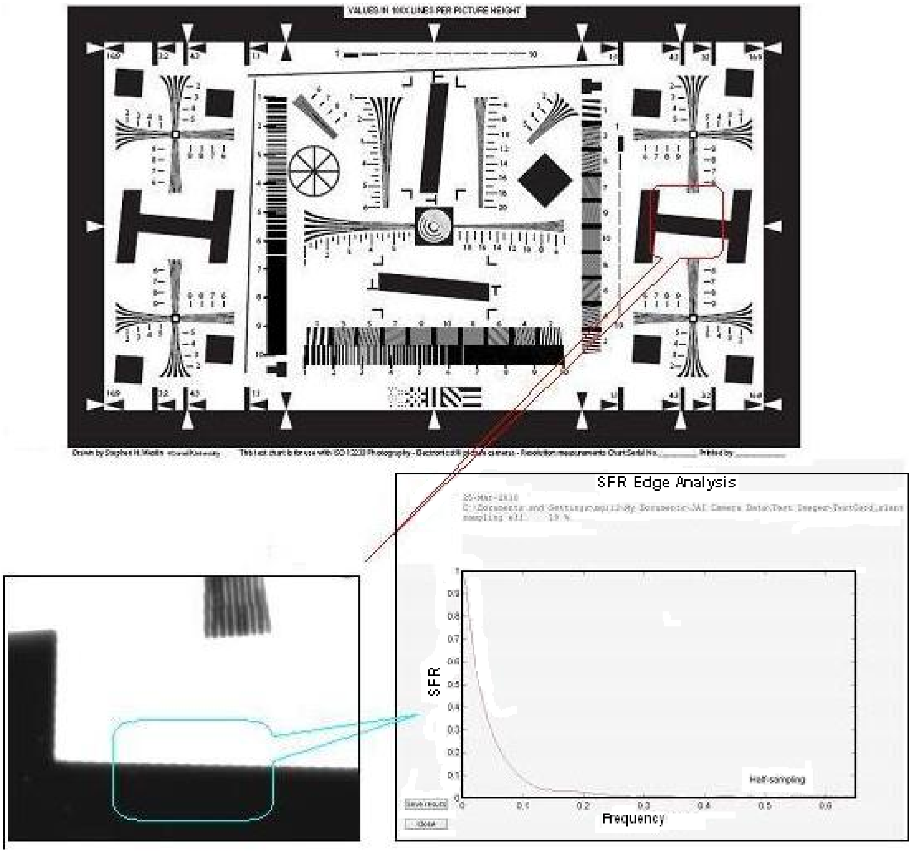

Figure 2.6: Optical performance of cameras may be assessed with a standard test card (conforming to ISO 12233). From an image a suitable slant edge is selected, and analysed by software to produce a plot of the *Spatial Frequency Response.*

The procedure followed is to focus a selected portion of the test card so that a straight edge with good contrast appears in the camera frame, slanted at an angle of a few degrees to the horizontal (or vertical). After capture, the ‘sfrmat2’ software is run, allowing a suitable region of the edge to be selected from the picture file; the SFR analysis of this region is presented as a chart (see Fig. 2.6). This is a measure of how well details in the object are reproduced by the optical system as a whole.

Camera Optimisation before Experiments

Screen Camera Focus Checking For optimum image quality, the screen cameras in the Tomography section are checked for focussing accuracy. This work does not require any ALICE or EMMA systems to be live, and can be carried out whenever there is human access to the machine. Although easier with two operators, one to make adjustments while the other observes the sharpness of the real-time images, it can be carried out alone if a local view is set up on a monitor connected directly to the camera output, the installed coaxial cable at the camera housing having been removed. A more detailed description of the procedure is given in Appendix A.2.

Camera Focus Testing with Beam Calculations indicated that with Depth-of-Field = 26.7mm for the camera lenses in use, a large fraction of the screen (inclined at 45^o) was expected to be in focus (see Table A.1). This prediction was tested with a horizontally well-focussed beam. If there were appreciable defocussing across the screen, an increase in apparent beam width should be seen in the same beam observed at the edges, compared with the centre.

In the experiment, the beam was scanned across the screen using magnets which can bend horizontally. There are correctors located conveniently before the screen, but unfortunately these were found to be lacking in range, deflecting by only a small fraction of the screen width even at their limits. As an alternative, the nearest preceding dipole was used, at such a distance that full deflection was readily obtained with only a minor current variation. Dipoles have a weak horizontal defocussing effect - and, depending on pole-shape, may have some edge-focussing - but these are usually small and have been neglected here.

Both beam size and centroid position were obtained from the screen images using software written by ALICE staff and available on-line in the ALICE Control Room. The plot in Fig. 2.7 shows no systematic size increase away from the centre, and the trend for a smaller beam-size near the edges of the screen is almost certainly due to losses from beam clipping in the pipe, at larger deflecting angles.

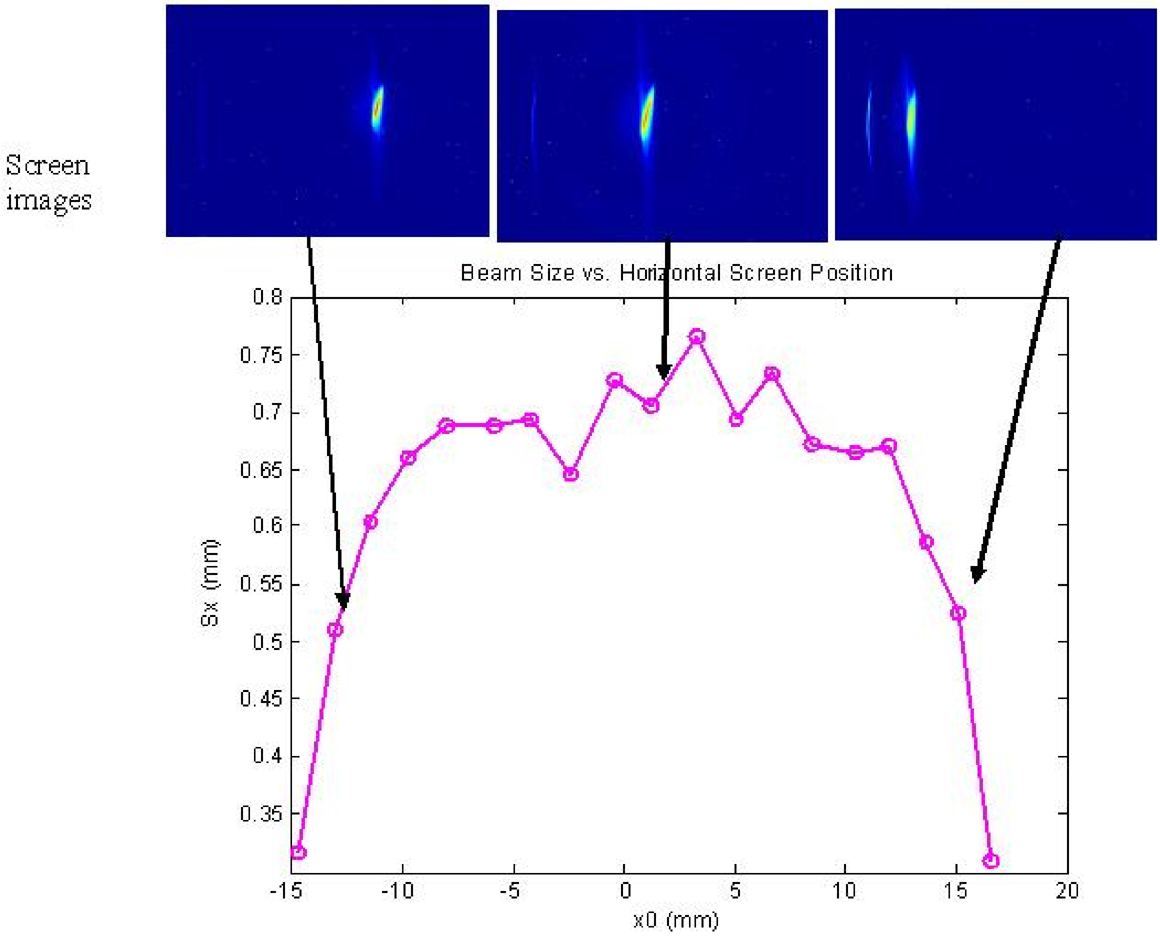

Figure 2.7: Horizontal beam size is plotted against beam centroid, as the beam is made to move across the screen by a bending magnet. Representative screen images are shown, at the centre and at the extremities of the range scanned.

2.3.2 Phase-Space Measurement by Standard Techniques

Preparation of Tomography Scan Input Data

The following steps must be taken when preparing for beam tomography by the 'quadrupole tomography scanning' technique, as illustrated in Fig. 2.8:

1. Make initial selection of the quadrupole(s) for scanning of magnet current (Horizontally and/or Vertically-focussing as required), having a suitable imaging screen downstream of the quadrupole, and taking account of the desired 'reference' position for reconstruction of phase-space.
2. Obtain parameters for all other beam-line elements, from reconstruction position to imaging screen, including the quadrupole to be scanned.
3. Calculate transport matrices as described below, and by interpolation find the quadrupole currents, which give equally-spaced tomography projection angles θ.

4. Review the quadrupole selection made at Step 1, in view of the range of projection angles available.

5. Repeat Steps 1-4 for alternative beam energies, if required, scaling magnet strength with particle momentum where feasible.

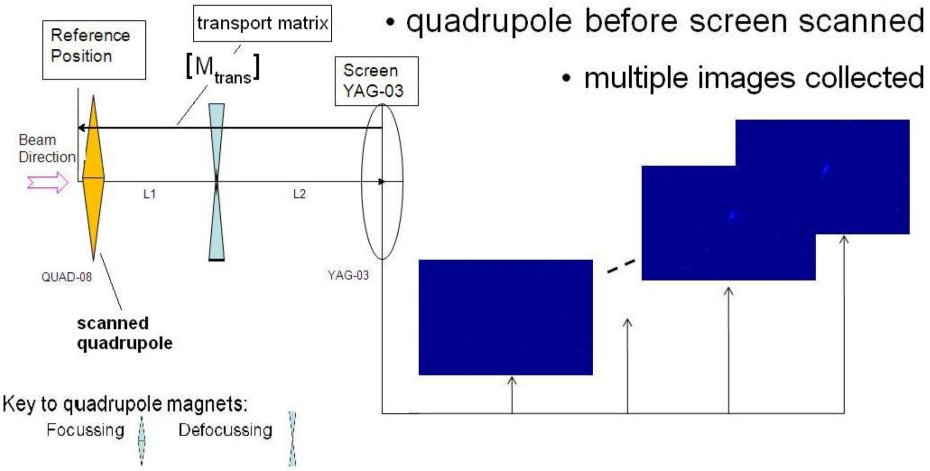

Figure 2.8: For horizontal phase-space tomography, a focussing quadrupole magnet is usually chosen for the scan, though other quadrupoles between reference position and screen will contribute to the full transport matrix M_{trans}. An image is taken at each setting, giving equal projection angle intervals θ.

For tomography, a set of projections are required at specific angles, θ. At any particular θ, the elements of the transport matrix

$$M = \begin{bmatrix} R_{11} & R_{12} \\ R_{21} & R_{22} \end{bmatrix} \tag{2.9}$$

must therefore be determined, by solving the equation $\tan\theta = R_{12}/R_{11}$ (see Equation 2.4 above), to obtain the appropriate values of the variables which parameterise R_{11} and R_{12}.

Solutions have been calculated for three cases of interest: (a) is of purely theoretical interest, (b) is a practical and specific case, and (c) is general. The range of angles where solutions exist has also been investigated.

(a) Drift Space In this, the simplest (but theoretical) case, the matrix is $M_{\text{Drift}} = \begin{bmatrix} 1 & L \\ 0 & 1 \end{bmatrix}$ giving $\theta = \arctan(R_{12}/R_{11}) = \arctan(L/1)$ where $L =$ drift length, considered here to be a variable; in practical beam-lines, it has of course a fixed value. Therefore, solving for parameter L,

$$L = \tan\theta \tag{2.10}$$

As seen in Fig. 2.9 there is a continuous solution on the interval $[-90^o < \theta < +90^o]$, asymptotic at $+90^o$.

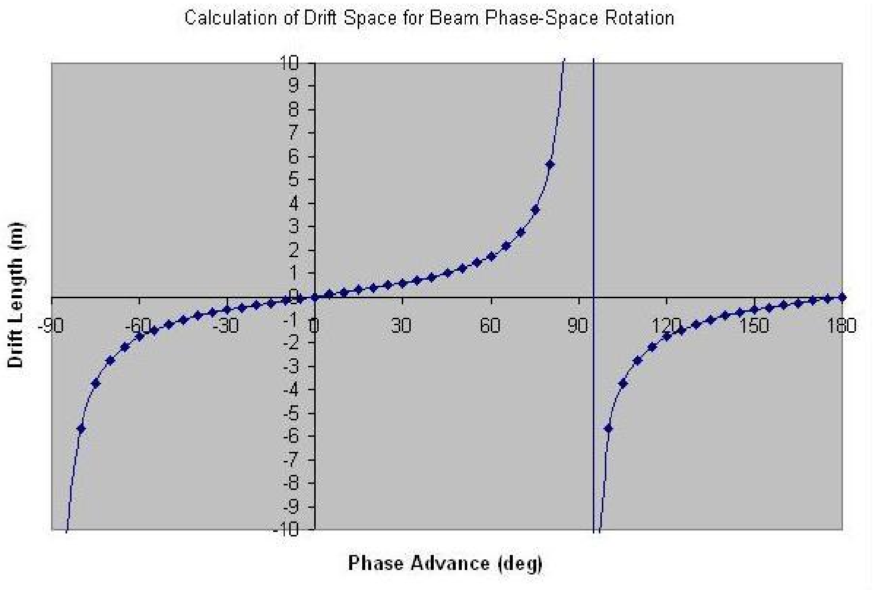

Figure 2.9: Varying the length of a drift space $L = \tan\theta$ between reference point and imaging screen gives a simple - if impractical - way of providing a range of projection angles θ close to 180^o, except near the asymptotes where $\tan\theta \to \infty$.

(b) Focussing Quadrupole with Drift Space For this practical case, the combined matrix is

$$M_{\text{FQuad+Drift}} = M_{\text{Drift}} M_{\text{FQuad}} \tag{2.11}$$

which leads to

$$R_{12} = \sin(\sqrt{K}s)/\sqrt{K} + L\cos(\sqrt{K}s) \text{ and } R_{11} = \cos(\sqrt{K}s) - L\sqrt{K}\sin(\sqrt{K}s) \tag{2.12}$$

With fixed values of drift length L and quadrupole magnetic length s, the value of focussing strength K is found as a solution of the following equation, for a given θ:

$$\tan(\sqrt{K}s)/\sqrt{K} + L + \tan\theta(L\sqrt{K}\tan(\sqrt{K}s) - 1) = 0 \tag{2.13}$$

Numerical methods are used for solving this equation in K.

There is a continuous solution for K only over ($\delta < \theta < 180^o$) where $\delta > 0^o$. The value of the lower cut-off δ depends on both L and s, and the Fig. 2.10 plot shows examples for 2 different quadrupole-drift locations in the EMMA Injection Line, where drift space length L in Eq. 2.13 refers to either QUAD-08 → Screen 2 or QUAD-09 → Screen 2, identified in Fig. 2.5.

Using a MATLAB function, the Equations 2.10, 2.13 are solved for each angle θ in the sequence, the parameter thus determined being then applied in the transport matrix to propagate the phase-space distribution to the measurement screen.

(c) General Case If the beam-line section of interest for tomography, from reconstruction position through scanning quadrupole to screen, is more complex than Case

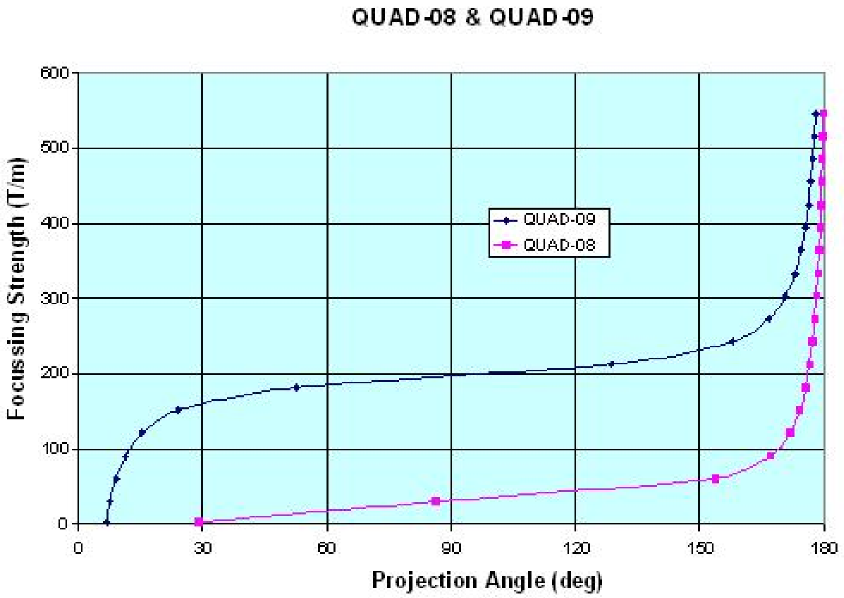

Figure 2.10: Changing the focussing strength K by adjusting the current in the quadrupole gives access to a range of projection angles θ, subject to power supply limitations. Plots of required K for a given θ for quadrupoles QUAD-08 and QUAD-09 show the effect of their different drift spaces to the screen.

(b), it is not possible to write down a general analytical solution to find the required values of K; a method of linear interpolation has therefore been developed in MATLAB [Hock K, 2010], according to the following scheme:-
Firstly, an array of values for theta at equal K (or quadrupole current) intervals is generated using the full transport matrix.

$$\theta = \arctan\left(\frac{R_{12}}{R_{11}}\right) = f(K) \tag{2.14}$$

Secondly, the values of current for an equally-spaced array of theta values having a range of 180^o is interpolated on the first array, thereby solving $K = f^{-1}(\theta)$, to provide the required quadrupole tomography scan input dataset.

Experimental Protocol

The procedure for tomography experiments was developed at the same time as the image data processing software, and was later refined in the light of operational shift experience. For the simplest scan sequences it follows this scheme:

1. Background images (i.e. with no beam) are acquired from the Tomography Section screens. These are necessary to correct beam images for background levels from any essentially 'fixed' sources, including faulty CCD pixels and the

steady low-level radiation generated during normal machine operation, present even without beam. An example is shown in Fig. 2.11.

2. A stable beam into the EMMA Injection Line (EMI) at the required energy is obtained. This can usually be achieved by fine tuning after restoring appropriate established settings from backup files.
3. The beam is centred on the axis of the selected EMI quadrupole magnet to be scanned, adjusting magnetic correctors as necessary. Centring is achieved when the beam screen image centroid remains stationary at all quadrupole magnet current settings. It should be noted that because of variations in camera alignments, the image may not necessarily appear central in the image, even when the beam is correctly centred through the quadrupole.
4. Beam position and size is confirmed on the screen over the full range of magnet scan currents to be used. It is important, especially at large currents when it becomes rather diffuse, that as much of the beam image remains in view as possible.
5. Tomography scans are performed using prepared magnet current data files as input to the control program. The software automatically sets the current value and acquires, names and saves the image file, before advancing to the next setting. In Fig. 2.12 are shown low, medium and high-current beam images taken from a typical horizontally-focussing scan.
6. Images collected are checked for correctness and quality, repeating scans as necessary if there has been a loss of beam or other malfunction.

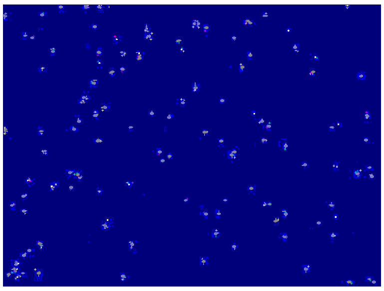

Figure 2.11: Typical features in a non-beam background screen image are scattered bright spots, due either to permanently damaged pixels (in fixed positions) or to cosmic/terrestrial radiation interactions with the camera CCD (randomly distributed). In this example they are enhanced for greater clarity.

Processing of Screen Image Data for Tomography

Computer codes have been written in MATLAB to automate, as far as is possible, the sequence of reading in and processing the raw camera images, before the prepared data

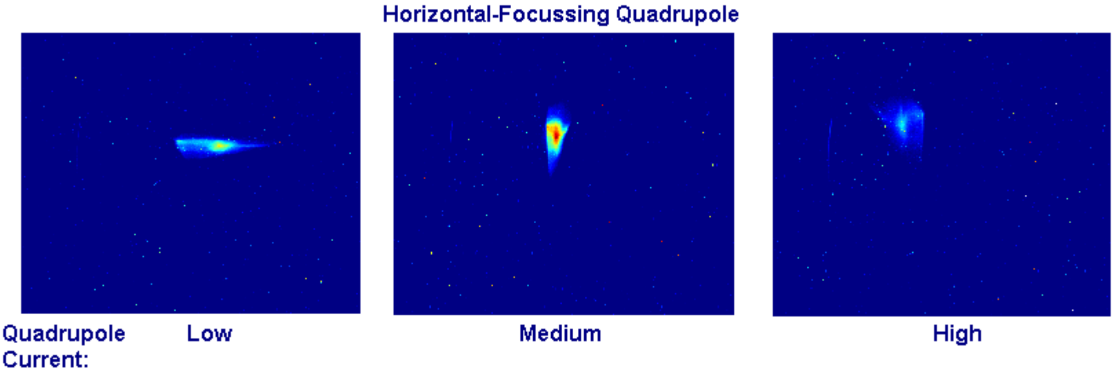

Figure 2.12: Samples taken from a set of screen images recorded at low, medium and high quadrupole currents show changes as the beam is more strongly focussed horizontally and defocussed vertically. The beam centroid would ideally stay the same.

is passed on to the reconstruction algorithm and the resulting phase-space distribution saved. Control is provided through a combination of (a) simple graphical user interface tools, and (b) parameter files, holding variables such as filenames and flags, which are set up beforehand and automatically read in at run-time.

Preparation Screen images are stored in a standard location, from which they may be individually selected by the User at run-time; alternatively, if processing a set from a full quadrupole tomography scan, all images found in the designated directory are automatically selected for loading. In Fig. 2.12, three representatives have been chosen from a typical scan set of about 150 images.

Backgrounds For each screen camera, background images are stored; the baseline background level across each image has been found to be fairly uniform spatially, apart from isolated 'bad' pixels caused by damage or defects in the CCD, but it does vary slowly with time. It is therefore advisable to collect fresh backgrounds at each tomography session; Fig. 2.11 shows an example. Several alternative user-selectable background subtraction schemes exist.

Generation of Reconstructions from Raw Images

The computer processing code implements the theory described in Sections 1.7 and 2.1. A more detailed description of the various stages in the processing is given in Appendix C.1; however, the principal steps, including images of some of the key screens displayed, are summarised here to aid understanding.

Note: Any step marked as an 'option' is run at the user's discretion.

- *Data and Parameter Loading*
  Transfer matrix array (one matrix per projection)

Image set (if quadrupole tomography scan) or individual screen images

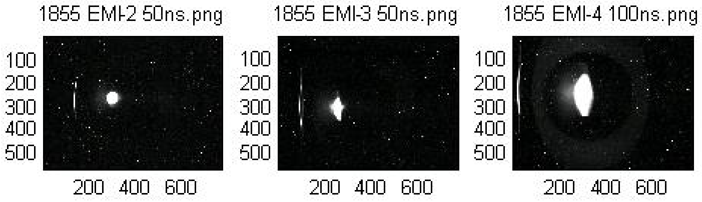

Figure 2.13: This example shows images of an 3-screen tomography dataset as displayed after loading from files. Headings are actual filenames and axes scales are in pixels.

Background image(s) (one per screen)

Calibration data (one set per screen)

Control flags (for switching of later processing)

- *Image Correction*

  Subtract background(s) from beam images

  Renormalise for intensity

  Apply screen calibration(s)

  Set a window around the beam region (option)

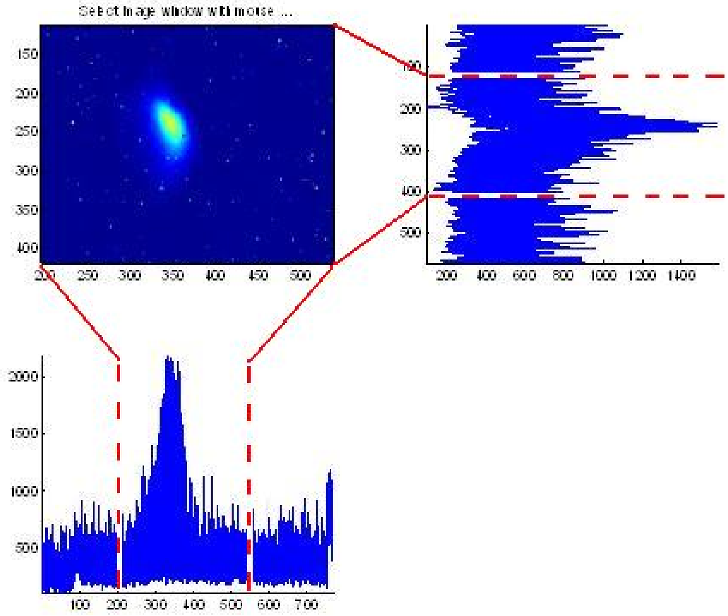

Figure 2.14: The full beam image set is displayed in overlay, with composite H and V projections below and R. The user selects a beam window, to include the peak.

Select and reject any images of low integrated-intensity

- *Projection Processing*

  Project onto x (horizontal) or y (vertical) axis

  Correct baseline, by peak-fit method or constant level (option)

  Scale projections

  Determine centroid of each projection

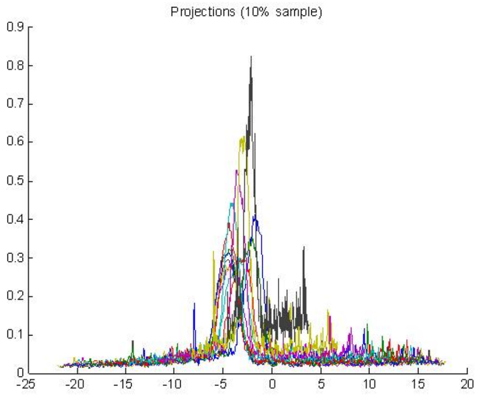

Figure 2.15: A superimposed sample of projections is displayed, in colours, confirming that the baseline is about zero, and only the main 'beam' peak is present.

Calculate weighting for irregular angle intervals (option)

- *Reconstruction from Sinogram*

  Set limits of reconstruction region in phase-space

  Run tomography algorithm (the standard is FBP)

  Save reconstructed phase-space results, i.e. image files and array datafile (option)

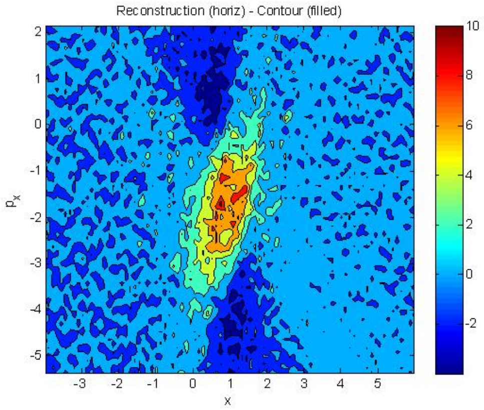

Figure 2.16: Reconstructed phase-space is displayed in contour plot form. Axis units are mm (x horizontal) and mrad (x' vertical).

Results of Phase-Space Reconstructions - Horizontal

The example shown in Fig. 2.17 is the phase-space distribution reconstructed from a quadrupole tomography scan based on 153 projections at 1^o angle intervals. The scanned quadrupole is QUAD-08 and the reference location for the reconstruction is the entrance of the same magnet. It has undergone all of the above processing stages but no further post-processing treatment.

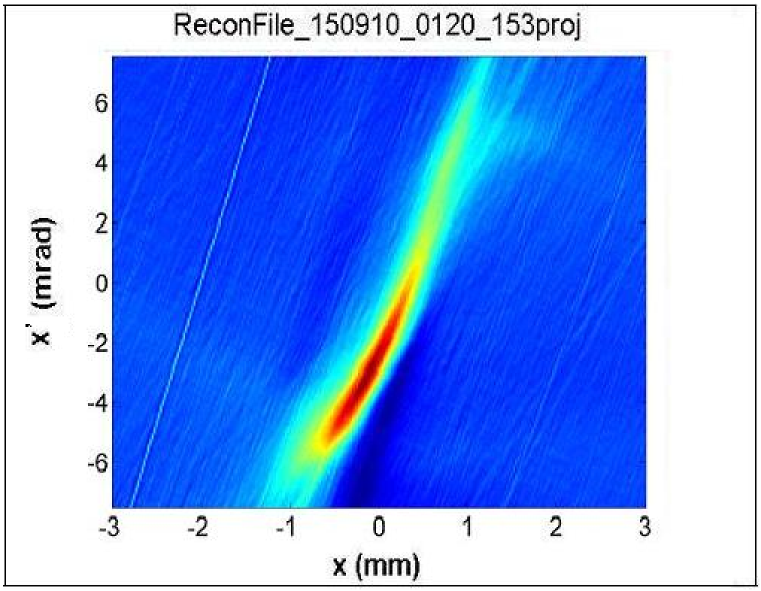

Figure 2.17: This reconstruction of horizontal phase-space from a quadrupole tomography scan of 153 projections in 1^o steps is typical with its roughly elliptical central region. The surrounding linear features are mainly reconstruction artifacts.

Delineation of the central distribution is reasonably clear, but the surrounding background region also has significant high-frequency noise which can confuse the picture.

Benefits of Filtering on Reconstructions The raw output of the Reconstruction algorithm shows the effects of input noise, as well as minor artifacts resulting from a limited dataset, which very often does not have all the projections for the ideal range of angles (0^o to 180^o). A moderate level of smoothing, e.g. with an $n \times n$ median filter which replaces each pixel with the median of its $n \times n$ neighbours, often helps to reduce high-frequency features and to emphasise the overall trends in the distribution. It is important, however, to avoid excessive smoothing, which tends to remove smaller details of possible interest.

Fig. 2.18 show the effect of increased levels of filtration, more obviously seen in contour plots. At 2 x 2, much of the high-frequency noise has been removed. At 8 x 8 what remains, outside the much better-defined outline of the central distribution, is a residual low-frequency element. Any significant residual noise which could cause a problem may be treated by other methods, one of which will be described later in Section 3.1.4.

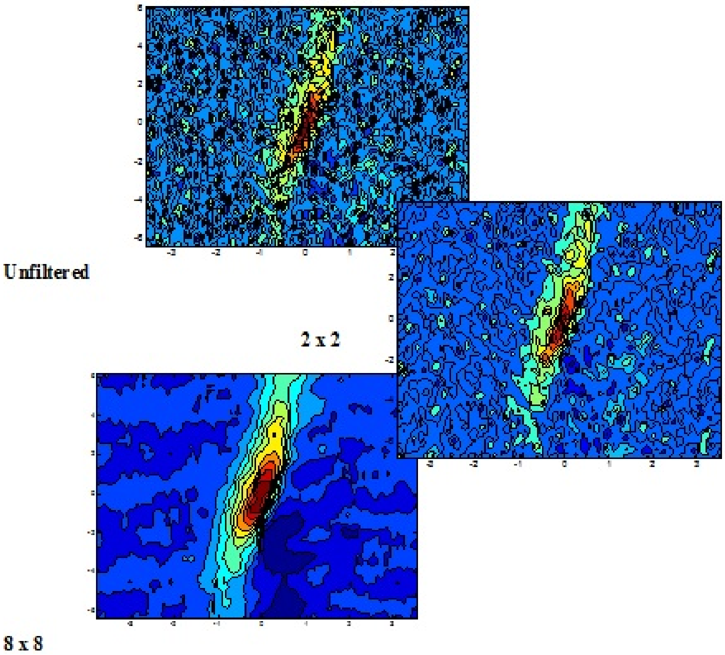

Figure 2.18: Applying an '$n \times n$' Median Filter at progressive levels to a reconstruction contour plot shows how higher-frequency noise is reduced by the smoothing effect, with much better definition of the central region of the distribution.

2.4 Quantitative Measurements (Phase 2)

For Phase 2, the screen camera pixel calibration was checked using established procedures; beam-line conditions, particularly the dispersion at the measurement position, were confirmed; and tomography experiments in both the horizontal and vertical planes were performed. An initial study of the effect of varying bunch charge on reconstructed phase-space was performed.

2.4.1 Screen Camera Calibration

If any camera lens corrections have been made to optimise screen focussing, maximum reconstruction accuracy will be maintained only if screen cameras in the Tomography section are recalibrated for Horizontal and Vertical magnification (in mm/pixel for the beam). This can be carried out using non-beam images, collected with the LED illuminators turned on so that the screen holder edges are visible, as in Fig. A.3. Software written in the 'Mathematica' code [42] is available for the calculation, which is based on the known dimensions of the screen. New calibration values are recorded in an EXCEL sheet, stored in a standard location so that they are available to all users.

2.4.2 Horizontal and Vertical Tomography Experiments

Tomography in the Vertical plane is exactly analogous to the Horizontal case. When the capability to reconstruct both Vertical and Horizontal phase-space was added, the potential then existed for processing existing image datasets in both planes. However, quadrupole tomography scan magnet current settings for the projection angle range selected for horizontal scanning (using a horizontally-focussing quadrupole) give a range of angles for vertical reconstruction which are far from optimal, as illustrated in Fig. 2.19. The clear difference between horizontal and vertical phase-space reconstructions is a result of the very restricted, irregular angular range of projections in the vertical, the quadrupole tomography scan settings having been chosen for a uniform, almost complete coverage (153×1^o) in the horizontal. On the other hand, the vertical range is non-uniform and only 23^o for this example. Specific vertical tomography experiments were therefore planned, using a suitable defocussing (i.e. vertically-focussing) quadrupole, with current settings calculated appropriately for the magnet.

Vertical Data Processing The dimensions of the tomography transfer matrix set, which is prepared along with the experimental input data, need only be $[2 \times 2 \times n]$ where n = number of projections, if just horizontal processing is carried out, but must be $[4 \times 4 \times n]$ if the vertical elements $R_{33n}, R_{34n}, R_{43n}, R_{44n}$ are included as well. The first stages of processing, where complete (x, y) images are handled, are common to both horizontal and vertical cases. It is at the stage when the data is projected, either onto the 'x' axis (horizontal phase-space) or the 'y' (vertical phase-space), that processing differs, through to the generation of sinograms and their associated 'position' and 'angle' arrays.

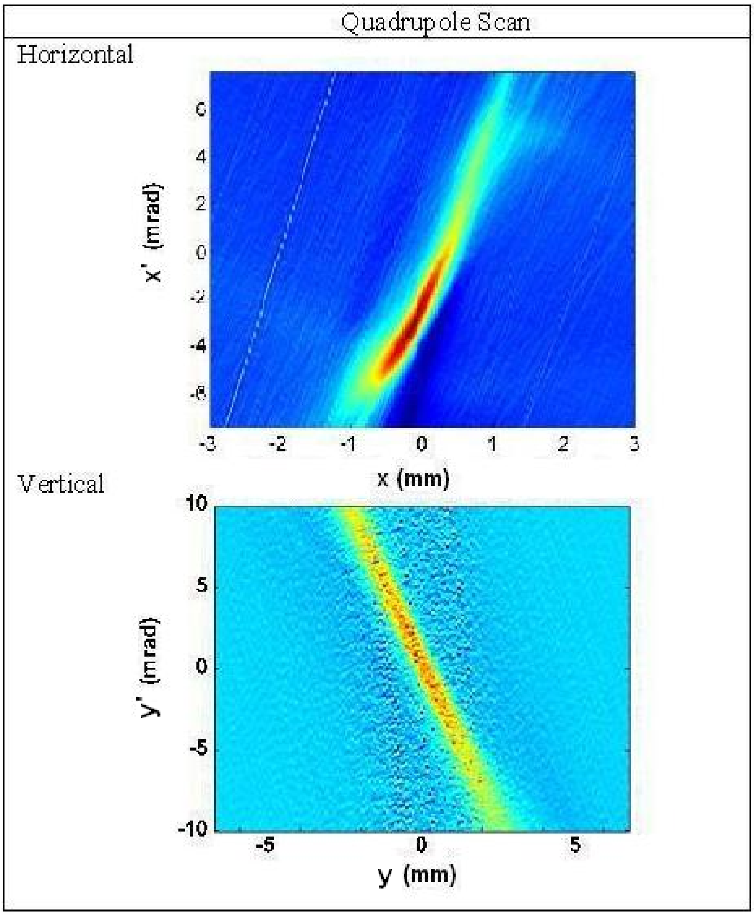

Figure 2.19: Using data from a scan optimised for Horizontal phase-space reconstruction, results are compared with the same data set processed for Vertical phase-space. Quality is poorer, as the Vertical projection angle range is much smaller & non-uniform.

2.4.3 Dispersion

In general the particles of a bunch do not all have exactly the same energy but are distributed about a mean. In a magnetic dipole field, the horizontal trajectory will vary with the energy; this is an example of 'dispersion'. In the presence of dispersion η_x, an energy spread σ_δ in a beam of emittance ϵ_x with beta function β_x adds a contribution to the horizontal RMS beam size σ_x, described by

$$\sigma_x = \sqrt{\beta_x \epsilon_x + \eta_x^2 \sigma_\delta^2} \tag{2.15}$$

and this would be reflected in the reconstructed phase space. Dispersion has been designed to be ≈ 0 in the tomography section, as there are two preceding dipoles whose effect is arranged to cancel out. The 2^{nd} term in Eq. 2.15 may then be ignored; this condition has been checked by measurement.

Dispersion Measurement Based on a known dispersion at position AR1-1 on ALICE, its value has been estimated at screen EMI-3 in the tomography section, as shown in Fig. 2.20. The procedure is to measure the deflection of the beam centroid when the energy is changed, in the region of known dispersion AR1-1; this gives a measure of the actual energy change. The energy difference dE can then be correlated with the linac settings used. With this data, together with the deflections dx observed for known energy changes, we can calculate the dispersion η at the position of interest EMI-3, using:-

$$\eta = \frac{E_0 \times dx}{dE} \tag{2.16}$$

where E_0 is the reference energy, in this case $\approx 12\,\mathrm{MeV}$.

Energy is adjusted by setting the accelerating gradients in the cavities LC1 and LC2 of the main linac, which is located upstream of the start of the EMMA injection line, indicated on Fig. 2.20. Using the value $\eta = 0.82\,\mathrm{m}$ (at AR1-1) established in previous ALICE calibrations, we obtain $\eta = -0.06\,\mathrm{m}$ (at EMI-3).
This result was close enough to zero to indicate that no adjustment to the three quadrupole magnets indicated in Fig. 2.20 was necessary.

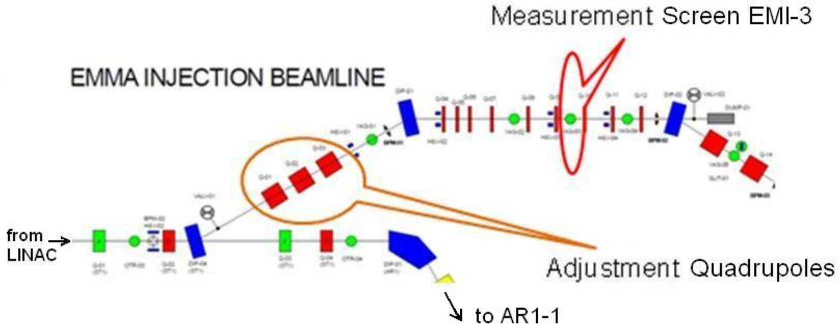

Figure 2.20: The dispersion η, known from previous measurements at AR1-1 in the ALICE ring, is used to calibrate the LINAC energy change, which in turn allows the dispersion at the position of interest (the EMI-3 screen) to be deduced.

2.4.4 Variable Bunch-Charge Experiments

After initial tomography work at an average charge per bunch of 40 pC, a series of experiments was planned specifically to investigate the effects of higher charges, as measured by the Faraday cup (see Section 1.4). Bunch charge is controlled by adjusting the attenuation of the photoinjector laser beam which initiates emission from the caesium-activated photocathode. The starting point would be the minimum charge which could be reliably imaged on the screen, given the fixed exposure of the installed ALICE cameras. At the other end of the scale, the maximum charge is that obtainable with zero laser attenuation, the governing factor being the quantum efficiency (QE) of the cathode. There is a gradual deterioration in QE with current drawn and intensity of use, and consequently the upper bunch-charge limit varies, typically between 80 pC when ‘fresh’ down to 55-60 pC near the end of its usable life. The achievable charge therefore depends upon the point in the re-caesiation cycle when the tomography experiment is scheduled.

Results of Experiments

Preliminary measurements using the quadrupole tomography scan technique, with QUAD-08 capturing images on screen EMI-YAG-03, were made to reconstruct horizontal phase-space.

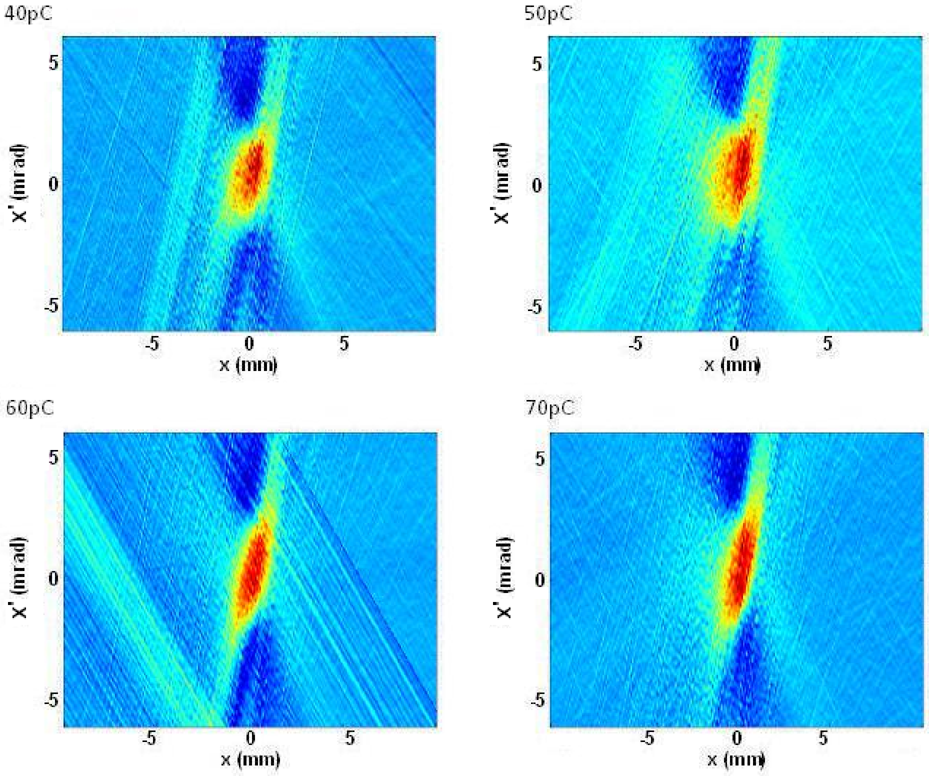

Figure 2.21: A series of quadrupole tomography scans, with QUAD-08 on screen EMI-03, has been made at a number of bunch charges up to the maximum obtainable. Reconstructed horizontal phase-space shows a gradual evolution with increasing charge.

An evolution of the phase-space distribution with increasing bunch-charge from 40 pC to 70 pC, is evident in Fig. 2.21. It is clear that in all cases the general shape and orientation is very similar. However, it is difficult to make any conclusions purely by inspection of the raw plots, which show significant noise in the regions surrounding the central core of the distributions. Methods of analysis which extract useful quantitative information are described later, in Section 3.1.1.

2.5 Beam Tomography: Applications for EMMA

Successful acceleration in the EMMA ring has been reported [5]. Characterisation of the transverse phase-space distribution at the injection line would assist in the quantification of the effects of decoherence on the electron bunch structure as it makes turns in the ring; to do this, equivalent beam tomography measurements may be made in the EMMA extraction line, which has been designed with a diagnostics section similar to the injection line. Unfortunately the commissioning of the extraction line came too late for any tomography experiments within the scope of this project. Such measurements would be complementary to the longitudinal phase-space information deduced from BPM and time-of-flight data, which is routinely taken.

Within the EMMA ring itself, the only instruments available for possible tomography are the YAG screens installed at two locations; these are used primarily for injection setup. However, with modification to the power supplies to appropriate ring quadrupoles to allow independent scanning of the current-strengths, these screens could potentially be used for tomography; but being destructive, data could be taken only on the first turn of the beam in the ring.

2.6 Summary

Initially, this chapter has treated the theoretical basis of the FBP algorithm, giving examples. This ‘real-space’ tomography is then related to phase-space using a geometrical approach. The experimental programme is introduced, broken down into four phases. For the first phase, the ideal imaging camera requirements are laid down, with practical optimisation measures. The preparatory steps for calculating input data to run a quadrupole tomography scan are given, in simple and general cases. The experimental protocol is listed, with notes on screen image and background data collection. The principal data processing steps are summarised, with notes and example displays and plots. After showing typical reconstruction results, the beneficial effects of median filtering are presented. In the second phase of experiments, vertical phase space is covered, with screen camera recalibration and dispersion measurements. Results of varying bunch-charge on reconstructed phase-space are shown. In conclusion, some possible future applications of beam tomography for the EMMA project are mentioned.

Chapter 3

Detailed Analysis and Parameter Extraction from Phase-Space Reconstructions

Introduction

To obtain useful information from distributions in phase-space reconstructed by tomography measurements, we can perform quantitative analysis by calculating parameters of interest. In this chapter these parameters are defined, and the theoretical basis for their estimation is presented, with some practical considerations and correction techniques to improve measurement precision with non-ideal, noisy data.

3.1 Principles of Analysis Techniques based on Linear Beam Dynamics

3.1.1 Parameters derived from 2nd Order Moments

For the case of an uncoupled distribution of particles, it is possible to define the **horizontal emittance** ϵ_x by:

$$\epsilon_x = \sqrt{\langle x^2 \rangle \langle p_x^2 \rangle - \langle x p_x \rangle^2} \tag{3.1}$$

where $\langle x \rangle$ denotes the expectation value of the quantity x. ϵ_x is conserved along a beamline under the condition that transport is linear, symplectic and uncoupled [43]. Having obtained, by tomography, an estimate of the distribution $f(x, p_x)$ we can therefore calculate ϵ directly, from the 2nd order moments. The 1st order moment of position $\langle x \rangle$ is just the beam centroid.

In addition, the three Twiss parameters, β, α and γ, interpreted as representative of the local size of the bunch, are related to these quantities by:

$$\begin{aligned}
\left\langle x^2 \right\rangle &= \beta_x \epsilon_x \\
\langle x p_x \rangle &= -\alpha_x \epsilon_x \\
\left\langle p_x^2 \right\rangle &= \gamma_x \epsilon_x
\end{aligned} \tag{3.2}$$

A MATLAB code has been written to perform the analysis. Using the Twiss parameters β, α, γ and the emittance ϵ, calculated in this way from the 2nd moments of the distribution, the equation relating these quantities

$$\epsilon = \gamma x^2 + 2\alpha x x' + \beta x'^2 \tag{3.3}$$

which describes the *RMS phase-space ellipse* according to the principles established in Section 1.5.1, may be plotted on the (x, x') axes. The software displays this ellipse as an overlay on the distribution.

As an example, the parameters have been calculated for a typical reconstructed phase-space distribution, after applying various kinds of preliminary processing; the effects of 'filtering' have already been shown in Figure 2.18.

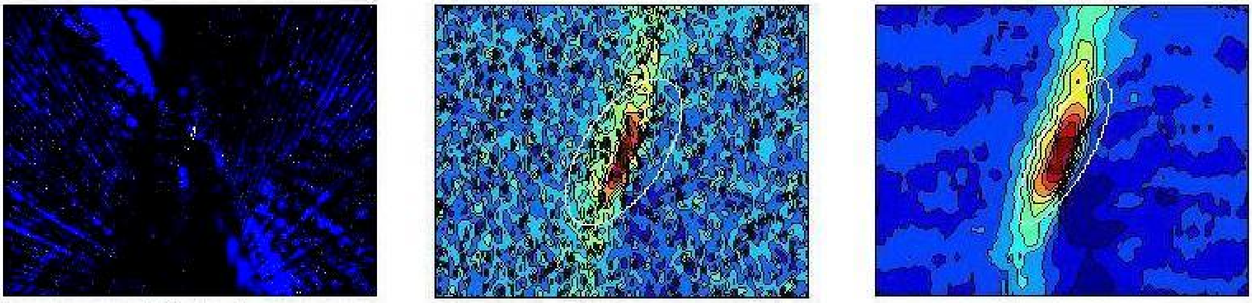

Filtered

Zoomed

Filtered/Zoomed

Figure 3.1: An example of the effect of image processing is shown. *Filtered:* A 5×5 filter has been applied onto a raw reconstruction. *Zoomed:* The original has been zoomed by 8 × 8 into a region of interest. *Filtered/Zoomed:* Both processes are combined.

In Fig. 3.1 the RMS ellipse described by Eq. 3.3 is overlaid (in white) onto the processed reconstruction.

Processing	ϵ	β	α
Original(not shown)	187.2155	0.66407	-0.16294
Filtered 5x5	0+115.1274i	0-1.5174i	0+0.25739i
Zoomed 8x8	2.9667	0.45304	-0.72093
Filtered/Zoomed 8x8	1.9408	0.45855	-1.1604

Table 3.1: Emittance and Twiss parameters are calculated from 2nd order moments of a reconstructed phase-space distribution. Various kinds and levels of preprocessing (filtering/zooming in) have first been applied to the raw data. (Note: 'i' denotes the complex part of a value.)

Comparing the results in Table 3.1, it is clear that the estimation of all parameters, but especially emittance, is a very strong function of the distribution in the region included around the central core, as well as the size of that region.

In the second case, it may be seen that the calculation has effectively failed because the result, which is complex, indicates that the value under the square-root of Equation 3.1 has become negative. This is forbidden by the Cauchy-Schwarz inequality:

$$\left\langle x^2 \right\rangle \left\langle y^2 \right\rangle \geq \langle xy \rangle^2 \tag{3.4}$$

This condition arises because the region surrounding the core of the beam distribution is dominated by prominent reconstruction artifacts, producing negative values. In the fourth case, these are significantly reduced by filtering.

Parameter Stability To study the stability of the parameters ϵ, β, and α as a function of the post-processing applied, reconstructed phase-space data from a similar dataset to that shown in Table 3.1 was subjected to increasing levels of $n \times n$ pixel filtering, before running 2nd moments analysis. In Figure 3.2 all three parameters are plotted against n. There is a clear fall in both ϵ and α, with a slight rise in β, up to 8 × 8; a plateau region then persists until about 16 × 16, beyond which a steady rise continues through 64 × 64. Although this study is very limited, it indicates that the optimum for the filter level lies between 5 × 5 and 10 × 10 pixels, supporting the hypothesis that initially there is a smoothing out of higher-frequency reconstruction artifact and camera noise components. Excessive filtering will begin to degrade the central distribution, smearing it out across phase-space and increasing the measured ϵ value.

For a more comprehensive treatment, the study could be repeated using particle tracking simulation (as described in Chapter 4) to simulate image noise and artifacts. Such an approach would ensure that ϵ, β, and α had well-defined values, for ease of comparison with the parameters as extracted after processing.

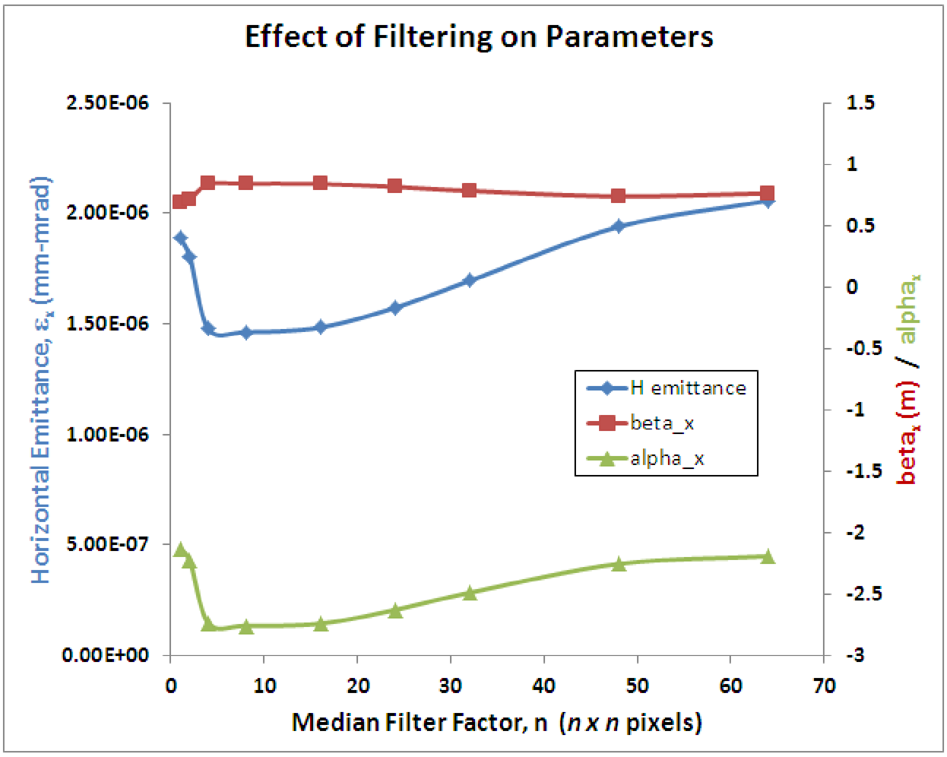

Figure 3.2: Horizontal emittance ϵ_x, and Twiss parameters β and α, calculated from 2nd moments of a distribution which has been processed by an $n \times n$ median filter, are plotted against n. The clear and consistent trends indicate an optimum of $5 < n < 10$ in this case.

3.1.2 Rebinning of Image Data before Reconstruction

Confidence in analysis results may be improved if reconstruction artifacts, due to deficiencies or incompleteness in input data, can be eliminated or suppressed. Theory indicates that **’aliasing’** artifacts from the Filtered Back Projection (FBP) reconstruction method may be reduced when the Nyquist criterion [24, p. 186] is satisfied:

$$N_{proj} \sim \frac{\pi}{2} N_{pos} \tag{3.5}$$

For a fixed number of projections N_{proj}, the number of positions N_{pos} can be adjusted by ‘binning’, combining adjoining pixel values, to meet this requirement.

As a test, a screen image set from a quadrupole tomography scan was pre-processed through the graphics program ‘ImageJ’ to rebin it (by aggregating every 4 pixels into 1). Standard tomographic processing was then carried out, making due allowance for the effective reduction in screen resolution (in pixels/mm).

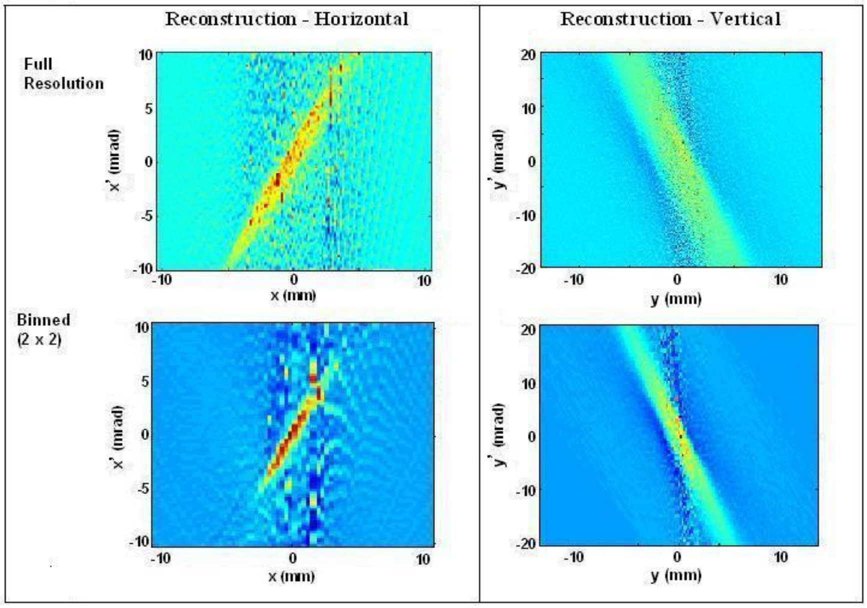

Figure 3.3: The screen images used at 'Full' resolution to reconstruct the upper phase-space distributions were rebinned by aggregating adjoining 2 x 2 pixels into one. Reconstruction was then repeated using this 'binned' data, to produce the lower results.

In Fig. 3.3, the upper plots are horizontal and vertical phase-space at the original 'full' resolution; the plots below are the same distributions after rebinning. Some reduction in the extent of the central distributions is evident, but the general shapes are preserved. Clearly some artifacts persist, however, though at a lower spatial frequency; it is not obvious that there has been any very significant improvement overall.

3.1.3 Fitting of Idealised Distributions

For many charged particle sources, and specifically the photoinjector type used in ALICE, a reasonable approximation to the beam distribution in phase-space is a 2-dimensional Gaussian function. Under this assumption, a function parameterised in the form

$$f'(x,x') = Ae^{((a(x-x_0)^2+b(x-x_0)(x'-x'_0)+c(x'-x'_0)^2))} \tag{3.6}$$

may be fitted to the reconstructed distribution $f(x,x')$ by the method of 'least-squares', for some values of A, a, b, c, and x_0, x'_0.

This functional fitting has been implemented as a MATLAB code. The algorithm works by first calculating estimated starting values for the 6 fitting parameters, based on assuming initially that the centre is at (0,0), and finding the position of the maximum value in the distribution. From this, the full-width at half-maximum (FWHM) in both x and y is derived, and hence an estimate for the angle of the principal axis obtained. These initial values are passed to a standard least-squares functional fitting routine, which returns a new set of 'best-fit' parameters as well as a new (fitted) distribution; this may be used for display and further analysis.

Having obtained the fit, it is instructive to apply the '2nd order moments' analysis described in Section 3.1.1 to both the fitted function and to the original distribution, and to compare the results. In the example (Fig. 3.4) the data was derived from a quadrupole tomography scan of 153 projections at 1^o intervals.

It will be seen from the analysis results in Table 3.2 that the 'fitted' emittance is much smaller than the 'raw', whereas the horizontal beta function is comparable in the two distributions. This appears to be due primarily to the effect of the artifacts in the region outside the main distribution, arising from the reconstruction algorithm. For distributions which are far from Gaussian, parameters calculated after fitting could be significantly different from the original 2nd order moments values. The code used is linked to that described in Section 3.1.1 above.

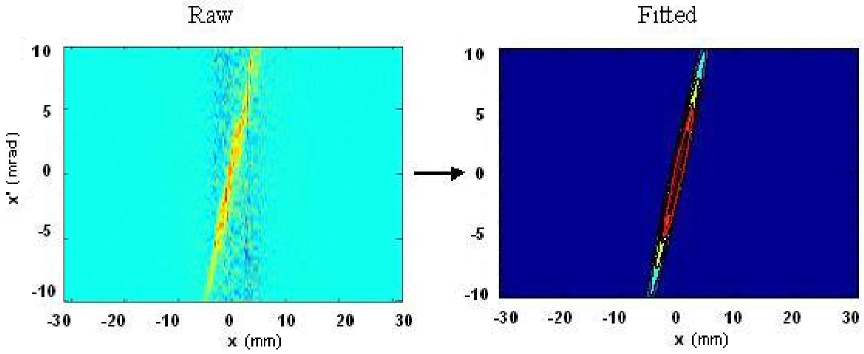

Figure 3.4: The 'raw' reconstruction data in the left-hand plot has had a Gaussian surface in 2-D fitted to it by a least-squares method. The 'fitted' result is shown on the right as a contour plot.

Horizontal	**Emittance** (mm-mrad)	**Beta** (m)	**Alpha**
Raw	45.6925	1.7822	-0.19867
Fitted	3.6129	1.6878	-3.2654

Table 3.2: The calculation of emittance ϵ_x and Twiss parameters β, α is made by 2nd moments analysis, for a raw reconstruction and for the same distribution after Gaussian fitting. The two sets of results are compared.

3.1.4 Additional Corrections in Tomography Data Processing

Further techniques have been applied to raw image data during processing, to correct for some instrumental effects which have been shown to introduce systematic errors into estimates of parameters - such as emittance - from tomography data [1].

Applying Threshold Levels in Projections Raw projections from screen images typically show a relatively sharp peak, due to the beam itself, superimposed onto a 'pedestal' or noise floor which is relatively uniform across the pixels of each projection. Selecting a level to use as a threshold, defined as a fraction of the peak projection value, the same chosen threshold is subtracted from all projections. As an additional correction, any value in a particular projection which falls below the threshold is set to zero. Although it appears somewhat arbitrary, this step effectively suppresses random noise and camera pixel defects which would otherwise perturb the image, and hence confuse the reconstruction algorithm.

The effect of thresholding on the emittance ϵ derived from this corrected data is shown when ϵ is plotted against threshold, as seen in Fig. 3.5; an appropriate threshold to choose is a value slightly beyond the foot of the initial steep down-slope, where there is a sharp easing of the gradient as ϵ then falls only slowly with the chosen threshold.

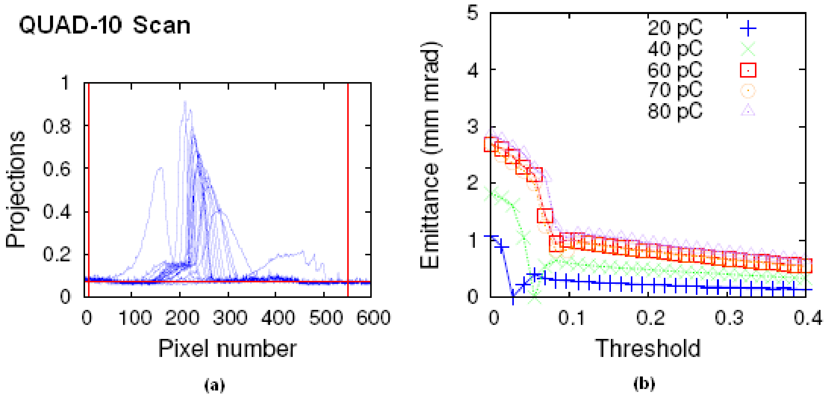

Figure 3.5: (a) A set of superimposed projections shows the noise floor, with the red horizontal line as an suitable threshold. (b) As the threshold subtracted from projections as a background correction is increased, the calculated emittance first drops steeply before levelling off. The plot is repeated at different bunch charges.

Suppressing Background after Reconstruction It has already been noted that the region around the main distribution is very often noisy due to reconstruction background, which contributes significantly to the uncertainty in the calculation of parameters by the 2nd moments analysis of Section 3.1.1. It would be possible to remove this background by arbitrarily applying a single threshold across the whole distribution. Instead, it is preferable to use the individual 'projection' thresholds, as already defined above, at each angle. This truncates the projections, setting the background to zero at variable distances out from the centre, depending on the angle of each projection, as shown in Fig. 3.6. It is possible that in the process, minor structural details close to the noise level, such as beam halos, could be lost; comparing the reconstructed phase-space with and without this background suppression is therefore a useful precaution.

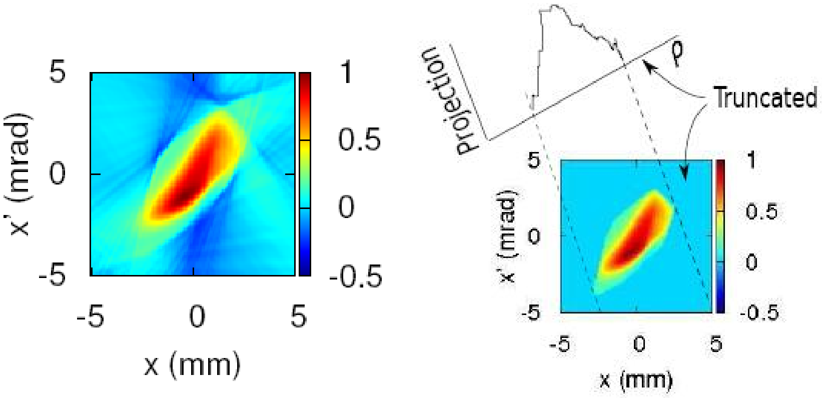

Figure 3.6: Truncation is applied by setting each projection to zero when it falls below the threshold. Applied to all projections, this effectively removes background noise in reconstructed phase-space, in this example a QUAD-07 scan at 80 pC bunch charge.

3.2 Alternatives to Tomography: Other Beam Diagnostic Methods

It is clearly of great benefit to have available, for comparing with tomography, an independent method of extracting beam parameters, especially if a common set of screen images can be shared as the raw input dataset.

3.2.1 Quadrupole-Scan Beam-Size Fitting Analysis

In this method, the strength of a suitable quadrupole is scanned using a range of current values, capturing corresponding beam images on a downstream screen [3, p. 199]. The RMS beam-size σ is calculated for each image, and its square σ^2 is plotted against the quadrupole focussing strength k. The plot is then fitted to a parabola described by

$$\sigma^2 = A(B - kl)^2 + C \tag{3.7}$$

where l is the effective (magnetic) length of the quadrupole.

Using the fitting parameters A, B and C, with the known transport matrix S between the scanning quadrupole and the screen, the geometrical (non-normalised) emittance ϵ and Twiss parameters α, β may be derived from the equations:

$$\begin{aligned} \epsilon &= \frac{\sqrt{AC}}{S_{12}^2} \\ \beta &= \sqrt{\frac{A}{C}} \\ \alpha &= -\beta\left(B - \frac{S_{11}}{S_{12}}\right) \end{aligned} \tag{3.8}$$

It should be noted that for a good parabolic fit, σ^2 should go through a well-defined minimum, using at least 20 points; sufficient of these should be plotted on each side of the minimum. Also, the analysis assumes that the 'thin-lens' approximation is valid for the scanned quadrupole; this may not be strictly true for all ALICE magnets.

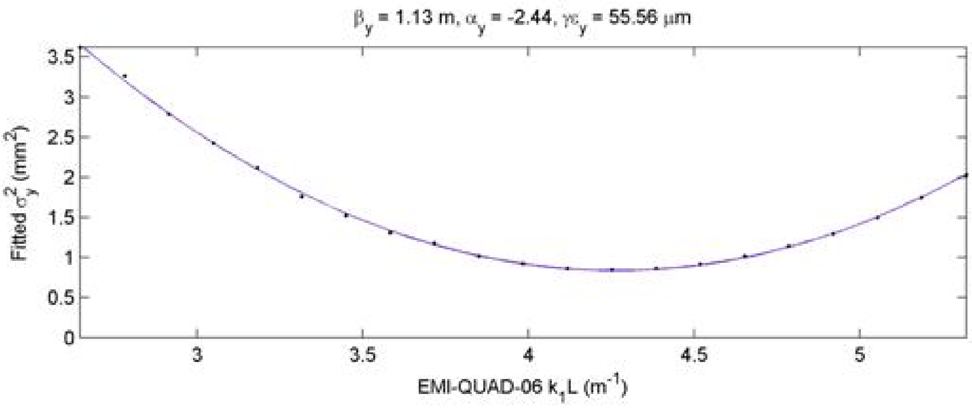

Figure 3.7: While the current in quadrupole EMI-QUAD-06 is scanned in regular steps, vertical RMS beam-size σ_y is measured from screen images. σ_y^2 is plotted against kL, where k is the focussing strength; from the parabolic fit, β_y, α_y, and $\gamma\epsilon_y$ are calculated.

An example of the application of this method for a vertically-focussing quadrupole (using simulated data from methods described in Chapter 4) is shown in Fig. 3.7, which plots Eq. 3.7 with Kl on the x-axis and σ^2 on the y-axis.

3.3 Application of Analysis Techniques to Experimental ALICE Data

Using a full record of the tomography datasets taken during experiments, maintained in MS-EXCEL format, the following sequence of analysis of the reconstructed phase-space distributions is carried out. Thus a cross-reference is maintained between the various files and input parameters used and the results extracted by the processing software.

1. Zooming and Filtering. Applying an arbitrary zoom-in factor (to the x and/or y axes), the new distribution may be viewed and saved, with the display recentred on (0,0) if necessary; as a separate process, a median $n \times n$ filter may be applied, as previously shown in Fig. 2.18. Zooming is not required if the appropriate region of interest in phase-space has already been established by the limits set during reconstruction.

2. Gaussian Fitting - a 2-D Gaussian best-fit to the distribution (by a least-squares method, described in Section 3.1.3) is made and plotted.

3. Calculation of Parameters. The Twiss parameters and emittance (geometrical) are calculated by 2nd moments analysis of the distribution, as in Section 3.1.1.

4. Display Ellipse as Overlay. The parameterised RMS phase ellipse is plotted as an overlay onto its underlying distribution (raw, filtered or fitted).

3.3.1 Comparison of Experimental Beam Parameter Results

Results from repeat measurements of horizontal phase-space made on different ALICE shifts, using scans of the same quadrupole QUAD-08 and screen YAG-03, under nominally similar beam conditions with an energy of 12 MeV and bunch-charge of 40 pC, are compared in Table 3.3 [44].

	ϵ_x	β_x	α_x
Date	**(mm-mrad)**	**(m)**	
16.02.11	1.51	1.31	-0.20
27.02.11	0.71	0.40	-0.96
09.03.11	0.67	0.38	-0.94

Table 3.3: A series of tomography experiments were made on several ALICE shifts. The horizontal emittance ϵ_x and Twiss parameters β, α listed have been extracted by analysis from the reconstructed phase-space distributions.

Method	ϵ_x	ϵ_y
Single Slit	0.86	n/a
Slit Scan	0.72	n/a
Quad Scan	1.19	0.31
Measurement Average	0.92	0.31
GPT Simulation (Elliptical)†	0.75	0.15
GPT Simulation (Real Spot)†	1.39	0.30

Table 3.4: ALICE emittance measurements made prior to the start of tomography work, using other methods and simulations, are listed for comparison with Table 3.3. The first 3 experimental results are averaged, as all are considered of equal merit.
† Note: In the General Particle Tracer (GPT) simulations, the laser spot on the cathode, which has a significant bearing on the electron source emittance, is assumed to be either elliptical or derived from a real measurement. It should also be noted that these GPT simulations were carried out earlier [45], and are not directly related to the modelling within this project as described in Section 4.1. (All values quoted are in mm-mrad.)

It is notable that for the latter two tomography datasets in Table 3.3, all 3 parameters are in good agreement. For the first one, it was observed in the distribution that phase-space seemed to be split into two distinct regions or sub-beams, each with different properties. In such a case, it is obviously inappropriate to attempt to fit a single Gaussian function, and so the emittance is likely to be overestimated.

Further comparisons with different measures of transverse emittance, made earlier and based on the alternative methods mentioned in Section 1.5 and on simulations, are shown in Table 3.4. There is remarkably good agreement in the horizontal emittance

ϵ_x, especially with the latter two tomography results in Table 3.3, given the probable difference in prevailing measurement conditions. While these few results do not have great statistical significance, they do offer some confidence that the tomography technique can give reproducible and meaningful results.

3.4 Summary

This chapter has opened by stating the results of linear beam dynamics theory relating the transverse emittance ϵ and the Twiss parameters β, α, γ to the various second moments of the beam distribution in phase-space. Their relationship to the RMS phase-space ellipse is quoted, and an example used to show how different types of post-processing can strongly affect the derived parameters. The effect of 'rebinning' in matching projections to positions, and so reducing aliasing artifacts in reconstruction, is demonstrated. A two-dimensional Gaussian fitting procedure for raw reconstructions is described, with an illustrated example. Correction techniques in tomography processing are explained, one based on applying a user-selected threshold assessed as a fraction of the projection peak value, the other based on truncation of each projection to flatten the otherwise noisy background region around the central distribution. Quadrupole-scan beam-size fitting is introduced as an alternative means of extracting beam parameters, using a common beam image dataset to compare with tomography. Finally, experimentally-determined beam parameters from horizontal phase-space tomography are tabulated and compared with earlier emittance measurements from other methods, indicating good agreement.

Chapter 4

Space-Charge Simulation Studies

Introduction

Simulation is now a fundamental tool in accelerator research and development, enabling most of the structures and the effects of interest to be modelled in detail and reducing the need for experimental beam-time, which is usually strictly limited. The predictions from a model are useful indicators of the type and magnitude of the effects to be expected in the results of experiments. This chapter describes the use of the advanced particle tracking code GPT, with its built-in support for space-charge effects in the particle bunch. After initial studies including a simple quantitative validation exercise, a complete model of the full beam tomography process on ALICE, incorporating GPT, is presented with an analysis of the results.

4.1 Modelling with Space-Charge using Particle Tracking Codes

4.1.1 Particle Tracking Simulations using GPT

General Particle Tracer (GPT) is a mature software code for tracking charged particle motion in 3-D through arbitrary electromagnetic fields; it is primarily a tool for accelerator beam-line design. All the commonly-used beam-line elements are included in the standard product, and user-defined elements may also be incorporated.

The GPT capability for switching on space-charge interactions has specific relevance for investigating the particular conditions of the ALICE tomography experiments which are described later in Section 5.1.2. By simulating the experiment in GPT, it would be possible to predict experimental findings, particularly the magnitude of expected effects, or to suggest further experiments which might be required.

4.1.2 Fundamental Principles of the GPT Code

For the user, GPT resembles the older tracking code PARMELA, but improves on it in several ways, especially in the choice of step-size. Initial particle distributions in 6 dimensions are represented by 'macro-particles' (typically a few thousand) which are grouped so as to have the same mass/charge ratio, and therefore equations of motion, as elementary particles such as electrons. Coordinate sets may be user-specified from a file outside GPT, or may be adapted by built-in GPT routines in any combination.

The relativistic equations of motion for position and normalised momentum

$$\begin{aligned} \frac{d\gamma\beta_i}{dt} &= \frac{q(E_i + v_i \times B_i)}{mc} \\ \frac{dx_i}{dt} = v_i = \beta_i c &= \frac{\gamma\beta_i c}{\sqrt{\gamma\beta_i^2 + 1}} \end{aligned} \tag{4.1}$$

where the position x and the normalized momentum $\gamma\beta = p/mc$ are used as the coordinates of a particle, are solved at time-steps which adapt themselves automatically to the prevailing field gradients, to maintain accuracy. The integrator in GPT is a 5^{th} order Runge-Kutta solver. The primary output mode gives all particle coordinates at a specified **time**; however it is often more useful to obtain output at an interpolated **position**, where particles cross a 3-D plane which users may define as a 'non-destructive screen'.

4.1.3 Application of Space-Charge Theory in Particle Tracking Codes

The physical theory outlined in Section 1.9 is implemented in the code GPT in a number of different ways, which may be selected as appropriate to match the problem in hand.

3-D Point-to-Point Full particle-particle interactions are modelled by relativistic calculation of electromagnetic fields. We calculate the fields E due to a particle j of charge Q, at particle i's position r'_{ji} in j's rest frame, where there is only an electric field:

$$E'_{j\to i} = \frac{Q r'_{ji}}{4\pi\epsilon_0 |r'_{ji}|^3} \tag{4.2}$$

where β, γ are the relativistic factors and ϵ_0 is the permittivity of free space. By summing over all particles and converting back to the laboratory frame, we find the total fields:

$$\begin{aligned} E_i &= \sum_{j\neq i}^{N} \gamma_j \left[E'_{j\to i} - \frac{\gamma_j}{\gamma_j + 1}(\beta_j . E'_{j\to i})\beta_j \right] \\ B_i &= \sum_{j\neq i}^{N} \frac{\gamma_j \beta_j \times E'_{j\to i}}{c} \end{aligned} \tag{4.3}$$

The main disadvantage of this model is the long processing time, of order N^2 for N particles, which in practice restricts problems to a few thousand particles.

2-D Point-to-Circle Where there is cylindrical symmetry in the beam, particles may be modelled as uniform charged circles interacting with other 'point' particles. The fields acting on particle i due to the circle of charge for particle j are calculated from the electrostatic potential. The gradient is then taken, to calculate the electric field using $E' = -\nabla V'$, and converted to cylindrical coordinates. Relativity can be neglected in the transverse if we assume that the circle only moves longitudinally. We then transform back to the laboratory frame, adding all particle contributions:

$$\begin{aligned} E_x &= \sum_{j \neq i}^{N} \gamma_j E'_{x,j} \\ B_x &= \sum_{j \neq i}^{N} -\gamma_j \beta_{z,j} E'_{y,j}/c \end{aligned} \tag{4.4}$$

2-D Point-to-Line For continuous beams or very long bunches, particles may be treated as complete moving lines of charge.

Both of the 2-D methods improve performance by removing one dimension from the problem, which therefore requires far fewer particles for good statistics.

3-D Mesh It is stated in [46] that by dividing the beam into discrete volumes (x_n, y_n, z_n), processor time is scaled down to order N, allowing a standard PC to track up to $N = 10^6$ particles. Particle fields are interpolated and simulation noise is smoothed out in the meshes. The method fails when bunch particle velocities have significant spread.

Selection of Space-Charge Model to be used

In applying space-charge in GPT to ALICE tomography modelling, the full 3-D routine has been used throughout, for accuracy. It was found that with 10,000 particles, for the most complex beam-line model having six quadrupoles, run-times increased from 10 minutes to $3\frac{1}{2}$ hours when space-charge was switched 'ON'. This was accepted as the practical limit, and has been confirmed by the convergence checks illustrated in Figure 4.8.

4.1.4 Initial Demonstration of Space-Charge in GPT

The study of the effects of space-charge interactions using the GPT software code was begun with a very simple drift-space model, particles being initiated in the z direction

(i.e. along the beam-line) with no transverse momentum.
Input Parameters to GPT Drift-Space model:

- Energy of particles = 12 MeV
- Number of Particles = 1,000
- Bunches: Radius = 0.6 mm (Gaussian), Length = 1 mm
- Divergence = 0 (parallel to 'z' direction)
- Drift Length = 1.5 m

In the absence of interactions, all particles follow independent parallel tracks, and the transverse (x-y) beam profile does not change with z position. When space-charge is switched on, however, divergence is observed in the beam, increasing with the size of the charge.

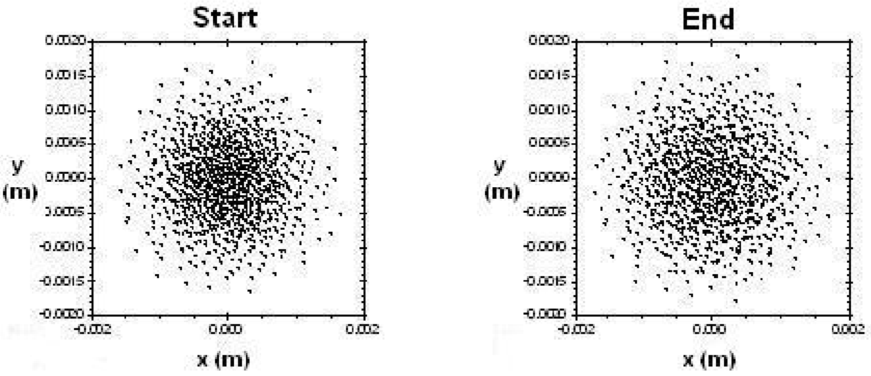

Figure 4.1: A circular section 200 pC beam of Gaussian profile, initially parallel with the beam-line axis, propagates down a 1.5 m drift space. Spreading of the transverse (x-y) profiles from start (L) to end (R) shows the divergence due to space-charge.

Transverse profiles in (x, y) show a perceptible increase in beam spread from the start to the end of the drift space, as seen in Fig. 4.1. The RMS beam-width in both x and y increases from (0.58 ± 0.02) mm to (0.65 ± 0.02) mm.

4.1.5 Benchmarking the Magnitude of Space-Charge Effects in GPT

To increase confidence in the GPT output results obtained, the simple drift-space model used for the initial demonstration test was benchmarked for a range of bunch parameters, enabling a direct quantitative comparison to be made with results from 'analytical' codes in terms of RMS beam-sizes (σ_x, σ_y).
Bunch Parameters (including all combinations of values where applicable):

- Energy of particles = 12 MeV (kinetic)

- Number of Particles = 10,000
- Bunch properties:
  Distribution = Gaussian / Uniform (cylindrical)
  Radius = 0.3 / 0.6 / 1.2 mm
  Length = 0.5 / 1.0 / 2.0 mm
  Charge = 0 / 20 / 80 pC
- Divergence = 0 (initially parallel to z-axis)
- Drift Length = 1.5 m

Analytical Space-Charge Codes

For simple beams, basic space-charge theory may be used to predict beam-size evolution by solving the equations of particle motion, as described in Section 1.9, without recourse to particle tracking codes. In principle, such codes can provide an independent benchmark for GPT results, in the case of uniform or Gaussian beams. Codes in both MATLAB (by K Hock) and Mathematica (by A Wolski) have been used in testing.

For a simple drift-space model where there is no focussing, we set $k = 0$ in Eq. 1.17. The differential equations then become

$$\bar{x}\text{''} - \frac{K}{4\bar{x}} = 0 \text{ [Gaussian beam] and } \bar{x}\text{''} - \frac{K}{\bar{x}} = 0 \text{ [Uniform beam]} \qquad (4.5)$$

where K is the *'perveance'* as defined in Eq. 1.17. These equations are solved for a range of values of distance z down the beam-line between 0 and 1.5 m, the length of the tomography section. Results as summarised in Fig. 4.2 confirm the prediction that as particles are closer to each other on average, space-charge forces are greater. The proportional effect on the RMS radius is increased for shorter, smaller and higher-charge bunches. The behaviour of beams with both uniform and Gaussian distributions has been investigated in this way, using scripts written in MATLAB.

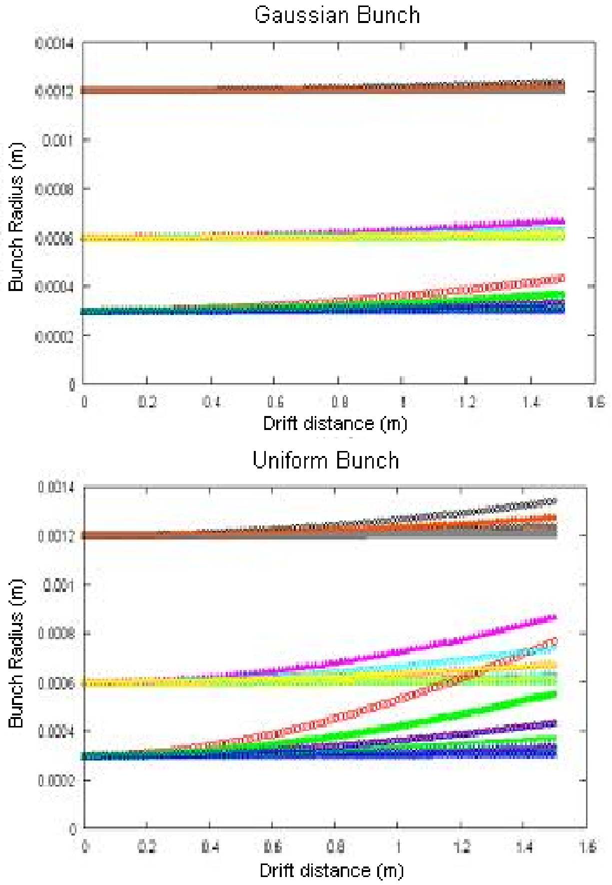

Bunch Radius, Initial (m)	Bunch Length (m)	Bunch Charge (pC)	Key
0.0012	0.0005	80	◇
0.0012	0.001	80	◆
0.0012	0.002	80	+
0.0012	0.0005	20	✱
0.0012	0.001	20	□
0.0012	0.002	20	■
0.0012	0.0005	5	●
0.0012	0.001	5	△
0.0012	0.002	5	▲
0.0006	0.0005	80	▲
0.0006	0.001	80	▽
0.0006	0.002	80	▼
0.0006	0.0005	20	◆
0.0006	0.001	20	+
0.0006	0.002	20	×
0.0006	0.0005	5	□
0.0006	0.001	5	■
0.0006	0.002	5	○
0.0003	0.0005	80	○
0.0003	0.001	80	●
0.0003	0.002	80	△
0.0003	0.0005	20	▽
0.0003	0.001	20	▼
0.0003	0.002	20	◇
0.0003	0.0005	5	+
0.0003	0.001	5	×
0.0003	0.002	5	✱

Figure 4.2: Using analytical codes with space-charge, bunch radius is calculated at 100 positions down a simple drift beam-line, for Gaussian (top) and uniform (bottom) transverse bunch distributions. Results for all 27 combinations of 3 different initial bunch radii, lengths and charges are plotted, with colours/styles listed in the key corresponding between the plots.

Within each of the two graphs, the 3 groups of plots represent different initial bunch radii. In each group are 9 plots, comprising the 3 bunch lengths × 3 bunch charges listed above. Each of the 27 plots has a unique colour/marker, and these correspond between the 'Gaussian' and the 'Uniform' graphs for the same parameter combinations as listed in the key.

The plots emphasise the much stronger effect of space-charge in uniform beams, where the mean inter-particle distance is smaller compared with the Gaussian case. For similar reasons, space-charge is also more effective in shorter and in smaller-radius bunches, for the same total bunch charge. Also evident is the onset of the major influence of bunch-charge above 20 pC, and the typical length of drift - about 40 cm - before a significant increase in bunch radius is seen.

GPT Space-Charge Model

The GPT space-charge routine solves Poisson's equation in 3-D for all particles of the bunch, taking proper account of relativity, as described in Section 4.1.3. In the GPT case, data is collected at 100 points uniformly distributed between the $s = 0$ and $s = 1.5\,\mathrm{m}$ positions along the drift space. As for the analytical codes, all 27 combinations of the selected bunch parameters were run in the GPT model and the results for RMS bunch radius collated for display in Fig. 4.3.

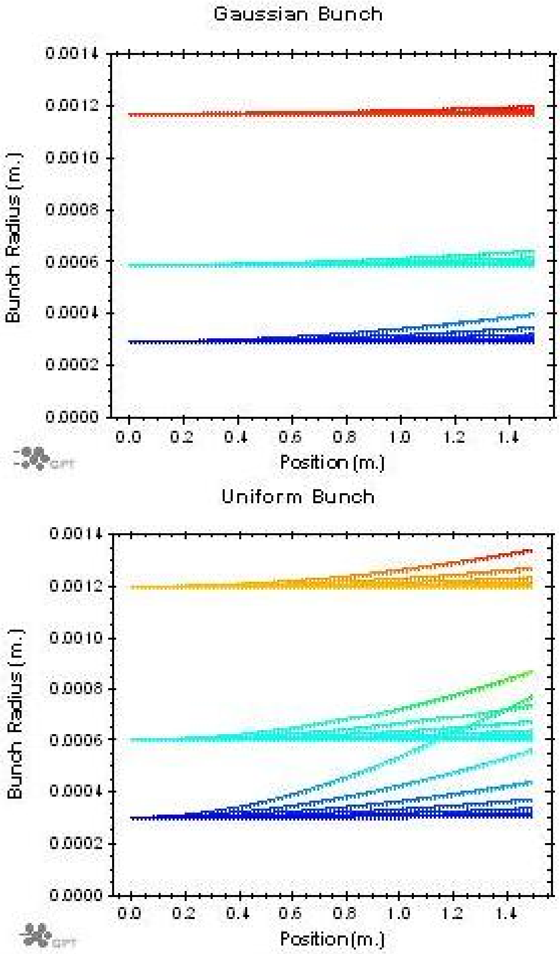

Figure 4.3: As for the analytical codes, the drift-space model is run in GPT, with the same combinations of bunch radius, length and charge, again for Gaussian (top) and uniform (bottom) distributions. RMS bunch radii at 100 positions down the line are extracted using built-in GPT functions.

Analytical and GPT Space-Charge Models compared

Comparing the analytical code results in Fig. 4.2 with the GPT model in Fig. 4.3, very good agreement is seen in the shape of all corresponding plots having the same values for the parameters *bunch radius*, *length* and *charge*. This is observed both in the Gaussian (top) and in the uniform (bottom) cases. Because the analytical results are based on well-established theory, we have increased confidence that GPT simulations with space-charge would provide accurate results in more complex situations, such as a detailed model of the ALICE tomography section.

4.1.6 Description of GPT Processing and Interface Features

The GPT engine or 'kernel' is accessed via a Windows interface called 'GPTWin', which is used firstly to build input files defining the characteristics of the problem in a structured language, and secondly to compose simple command scripts to run the problem. GPTWin also controls the post-processing analysis programs, 'GDFA' and its accessories.

The following file types, indicated as 'Inputs' in Fig. 4.4, are necessary to define and run a GPT model:-

'inputfile'.**in** - definition of the particle bunch and beam-line configuration;

'scanparametersfile'.**mr** - multi-run parameter values (i.e. scanned variables such as quadrupole currents), which refer to identifiers in the '.in' file, but are not needed if parameters take only single values;

'batchfile'.**bat** - batch file of commands for runtime control, which calls the GPT engine and if required the analysis programs, also specifying any intermediate filenames.

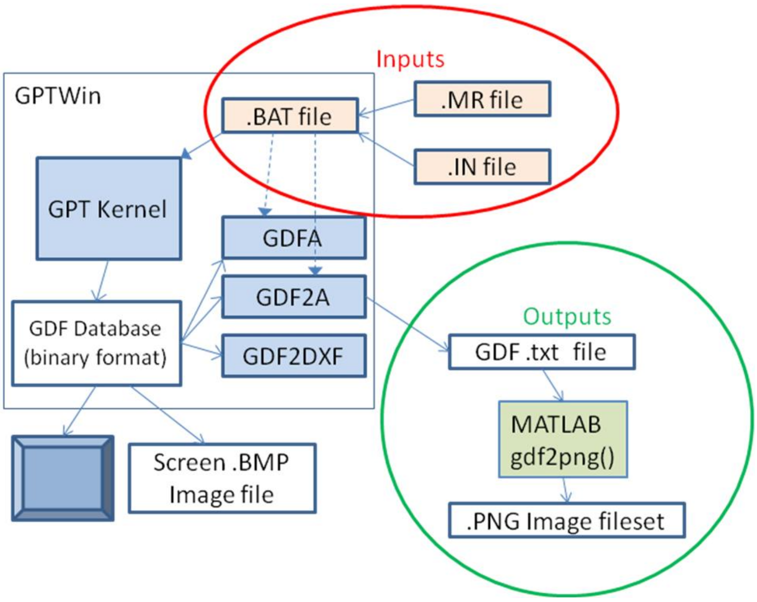

Figure 4.4: The Windows interface for GPT provides access to the kernel, and to analysis functions such as GDFA. A script editor for input .BAT, .IN & .MR files is built in. GPTWin also visualises output from binary GDF output files, and external programs can use data exported in text form e.g. for image file creation.

The output of a run is generated in a single GPT Data Format (GDF) database file which has a binary format, and may be interpreted through the GPTWin interface for viewing results graphically. Individual screens corresponding to selected parameter values may be viewed in scatter-plot or density-map displays (which may be saved as image files such as '.bmp' bitmaps).

To process the screen (x, y) data for preparing a tomography simulation, e.g. a complete quadrupole tomography scan set, the GDF native file is first converted to ASCII text format by a built-in GDF utility 'GDF2A'. Now outside GPTWin, the text file is readable by a custom-made MATLAB function 'gdf2png', which automatically generates a full set of screen image files (in PNG format). These images are available for detailed viewing and comparison, if required, and especially for processing and reconstruction by existing MATLAB tomography codes (see Fig. 4.4).

4.1.7 Detailed Space-Charge Modelling in GPT

The ALICE tomography section, with its three screens and four quadrupoles, was modelled in detail using GPT, with the addition of quadrupole QUAD-07 which is at the end of the preceding 'matching section'. QUAD-07 forms part of the configuration proposed for experiments on space-charge, to be used for horizontal phase-space tomography scans in conjunction with screen YAG-02. As a further development, the defocussing quadrupole QUAD-06 was added to model tomography-scan experiments for vertical phase-space, which would also use YAG-02. The arrangement is shown in Fig. 4.5.

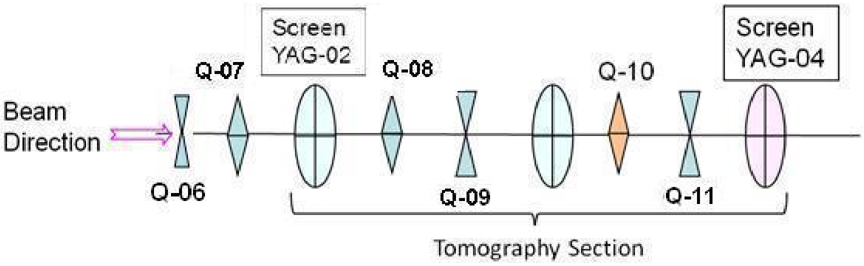

Figure 4.5: A schematic of the ALICE tomography section shows quadrupole magnets and 3 screens, identified by shorter versions of their ALICE project names. Conventional symbols distinguish focussing quadrupoles (e.g. Q-07) from defocussing (e.g. Q-09).

Space-Charge Effect: Beam-Size Difference Analysis

The horizontal RMS beam-size σ_x (and σ_y vertically) was selected as a suitable metric for observing space-charge effects, as it was anticipated that beam-size would be suitable as a parameter for the sensitivity of tomography reconstructions to space-charge. 'Screens', which in GPT are defined as virtual planes for tallying particles when they cross, and can optionally correspond to physical devices such as YAGs, are specified appropriately along the beam-line. It is at screens that particle positions (and momenta) are computed by GPT; from these, the beam-size may be readily derived either within GPT, or by calculation.

A bunch-length of 4 ps in time - equivalent to 1.2 mm at light-speed - was taken as representative, based on typical measurements made after the LINAC. Preliminary data taken with a 9 mm bunch - a typical value at the ALICE gun - predictably gave effects two to ten times smaller; however, it is quite realistic to expect significant compression of bunches both in the buncher cavity and in the LINAC itself, which follow the gun.

Input parameters were specified in a separate '.mr' file (see Fig. 4.4); this method supports nested loops for scanning multiple parameters, such as 'quad current' and 'bunch charge'. Quadrupole currents used corresponded to the same range of values as in the original tomography experiments to produce appropriate projection angles.

After running the GPT simulation itself, the analysis program GDFA was used to extract σ_x and σ_y from the raw $(x, y)_z$ data in the GDF output file. This data could be plotted within GPT, and also exported in text format. As effects on beam-size were small in absolute terms, the σ_x and σ_y data was processed outside GPT in 'text' form, to determine the **fractional** differences $\Delta\sigma_x/\sigma_x$ between the 0 pC case with no space-charge, and 80 pC which was the maximum charge obtainable experimentally.

Combining realistic initial phase-space parameters, as measured by tomography experiments, with the established GPT model, a series of runs was made at both 0 pC and 80 pC bunch charge, with quadrupole currents for QUAD-07 and QUAD-10 scanned over the range of tomography settings as before.

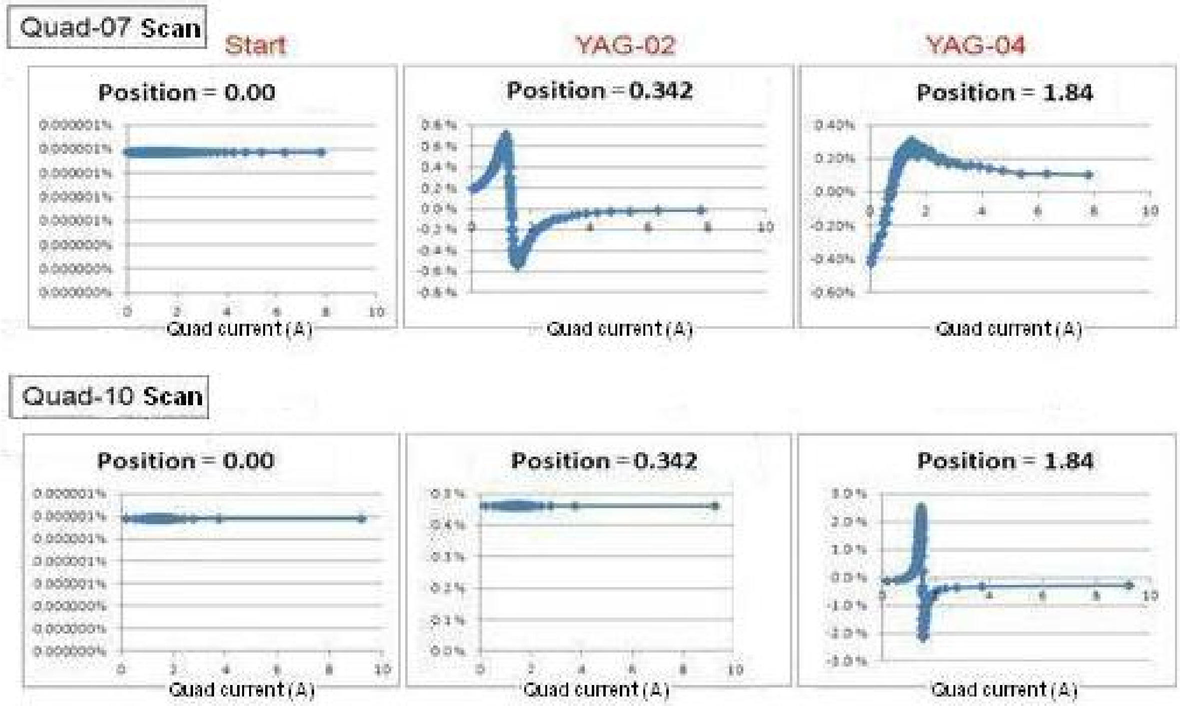

Figure 4.6: As the current in quadrupole QUAD-07 and then in QUAD-10 is scanned, the fractional horizontal beam-size difference, related to space-charge effects, is plotted at three screen positions, recorded in m., in the line.

Beam sizes were extracted to find the percentage differences between 0 and 80 pC, $\Delta\sigma_x/\sigma_x$, which are plotted against current for each screen position in Fig. 4.6. At the first screen position after the scanned quadrupole (i.e. at YAG-02 after QUAD-07, or at YAG-04 after QUAD-10), $\Delta\sigma_x/\sigma_x$ was found to be a strong function of magnet current, and a significant but less marked trend was seen at the screen further downstream. A very small but positive effect was even observed at a position almost immediately after the bunch was started, i.e. just before QUAD-07 or QUAD-10.

The peaked structure of the beam-size difference plots, seen at YAG-02 for a QUAD-07 scan, and at YAG-04 for a QUAD-10 scan, has been correlated with the absolute beam-size σ_x, which in Fig. 4.7 is plotted in red for the 'zero charge' (0 pC) case and in broken green for the 'high charge' (80 pC) case. As the absolute difference $\Delta\sigma_x$ between 0 pC and 80 pC is small, the red and green plots almost coincide. In the same figure, there is a rapid change of sign in the fractional beam-size difference $\Delta\sigma_x/\sigma_x$, plotted in blue, which occurs exactly at the point where the strength of the quadrupole focussing causes a minimum in σ_x. It is here that the largest effect from space-charge would be expected in the plane of focus, which in this case is horizontal, due to the closer proximity of the particles in the bunch. It has been postulated [1] that the rapid beamwidth increase over a small range of quadrupole strength occurs when the focussing is such that the horizontal beam waist coincides with a vertical waist, suddenly forcing the electrons much closer together. Confirmation of the exact mechanism would however require further work.

QUAD-07 Scan, observed at YAG-02

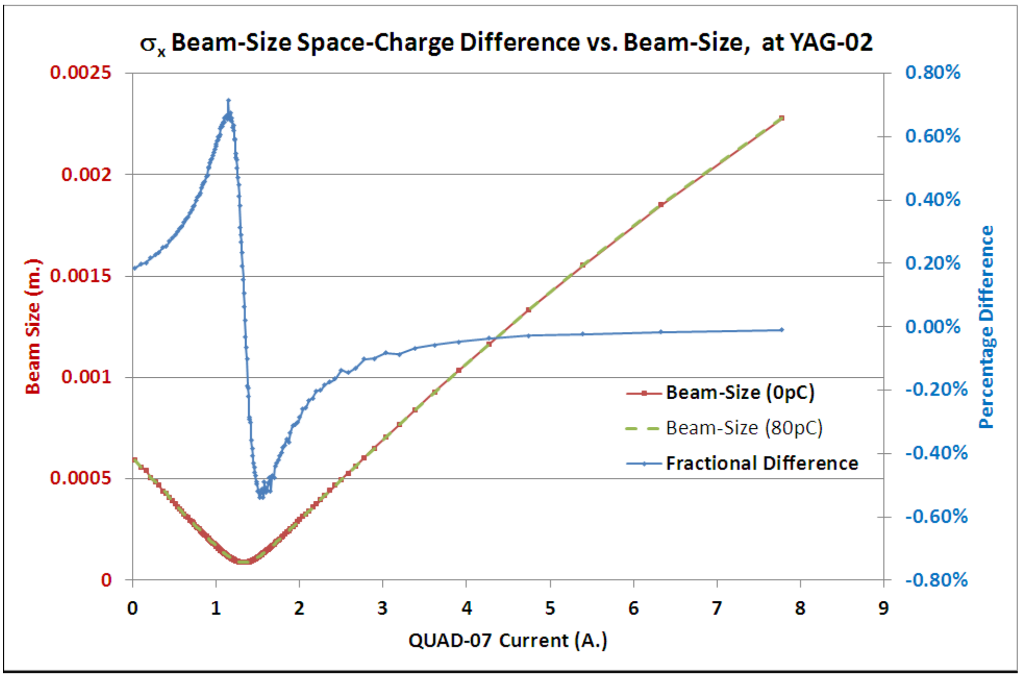

QUAD-10 Scan, observed at YAG-04

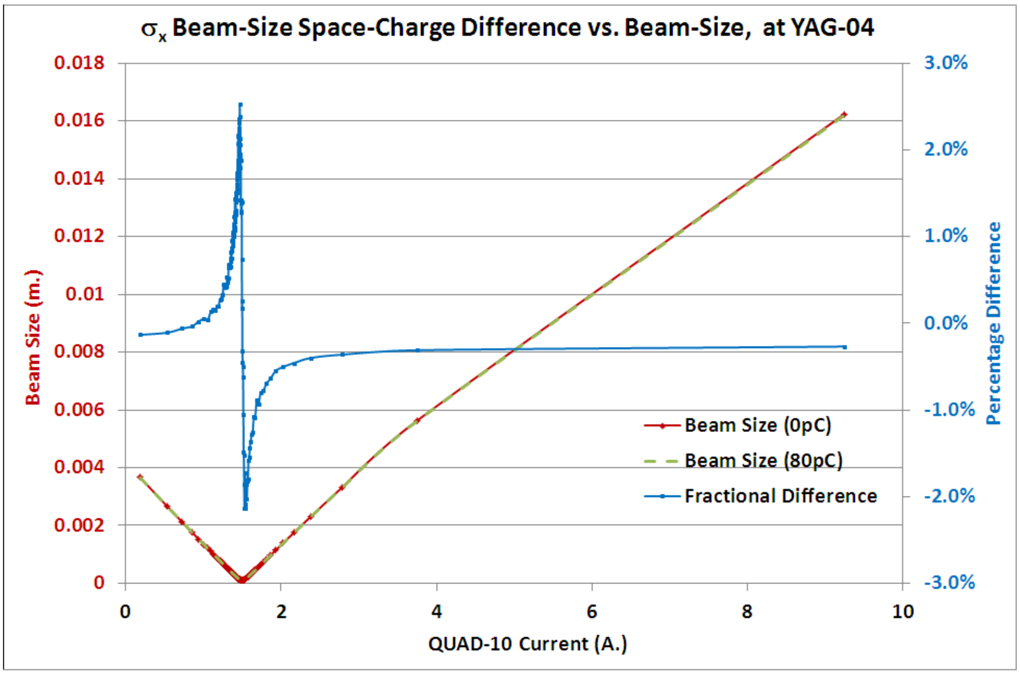

Figure 4.7: Details of the simulated effect of quadrupole current on horizontal beam-size difference due to space-charge, for QUAD-07 observed at the YAG-02 position and for QUAD-10 at YAG-04. Absolute beam-size at 0 pC and at 80 pC is plotted on the primary axes (red/green), with fractional beam-size difference on the secondary (blue).

Convergence Check of Beam-Size against Number of Particles Simulated

When a macroscopic parameter is calculated from the results of a simulation code such as GPT, there is a possibility of statistical effects due to the finite sample of particles modelled. For the ‘beam-size-difference with bunch-charge’ metric, its dependence on Number of Particles (*nps*) in the bunch was estimated by making a series of GPT runs with ‘*nps*’ as an additional multi-valued parameter.
Selected setting for the check (shown at left of Fig. 4.8, taken from Fig. 4.6) was:-

QUAD-07 current = 1.149 A

σ_x calculated at screen YAG-02, at Position = 0.342 m

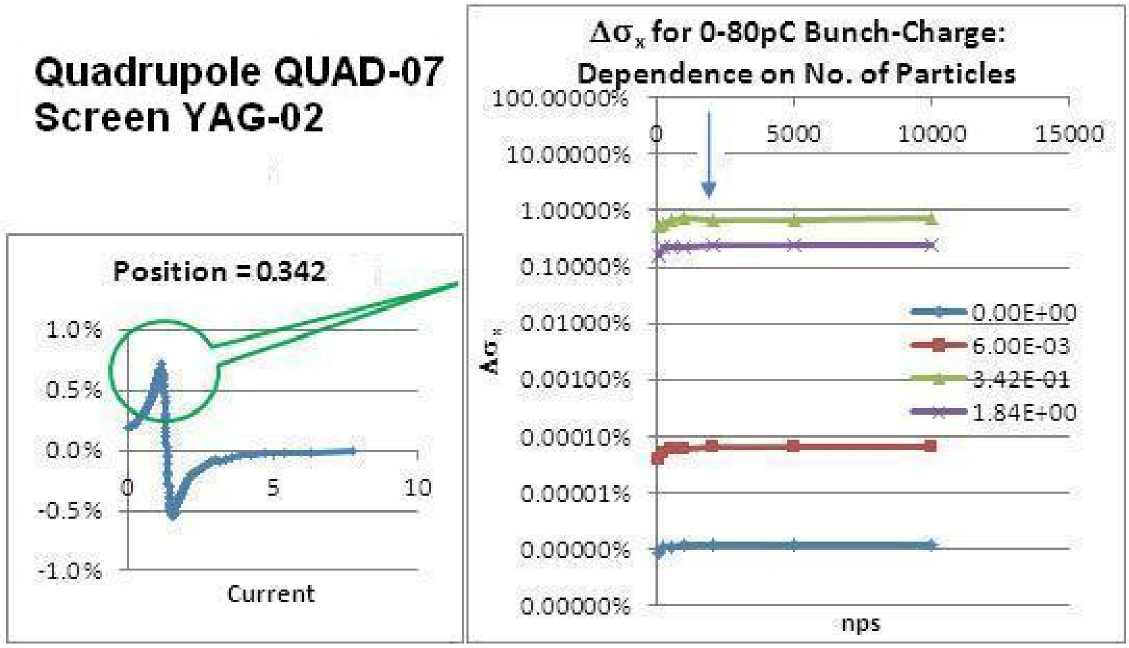

Figure 4.8: Choosing appropriate quadrupole current/screen position settings, the dependence of fractional beam-size difference on number of particles simulated *nps* is plotted, to confirm convergence and establish a working minimum for *nps* (arrowed).

These representative results indicate that the minimum number of macro-particles for convergence is about 1000. To provide a suitable margin, an appropriate choice is therefore 2000, unless time constraints indicate running a reduced number.

4.2 GPT Modelling for Tomography Studies

4.2.1 Investigating Observed Differences in Reconstructed Phase-Space

A detailed GPT model of the ALICE tomography section as shown in Fig. 4.5 was used to predict the results of experiments to reconstruct horizontal phase-space from quadrupole tomography scan data, looking for any differences which might be seen between results from QUAD-07 → YAG-02 scans and from QUAD-10 → YAG04 scans.

Actual experimental results are tabulated later, in Fig. 5.5.

The process was planned as follows:-

1. Start with a particle set based on measured phase-space at QUAD-07 entrance, using existing experimental data as available.
2. Use a GPT model to transport the beam to YAG-04.
3. Run GPT scans of QUAD-10 (horizontal) and QUAD-11 (vertical), and collect the simulated YAG-04 screen data.
4. Based on this data, reconstruct phase-space at QUAD-07 entrance.
5. Repeat GPT runs with (a) space-charge OFF, and (b) space-charge ON.
6. Compare simulated phase-space with experimental results.
7. Vary beam-line parameters, e.g. magnet strengths, to investigate the sensitivity of the measurements to errors in these parameters.
8. Repeat the procedure for vertical phase-space, using measurements from QUAD-06 and QUAD-11 scans (when available from later experiments).

This approach would allow a detailed investigation of how perturbations in the beam-line elements between QUAD-07 and QUAD-10 might account for any discrepancy observed in phase-space distributions, calculated with QUAD-07 entrance as the common reference point, using QUAD-07 data as compared with QUAD-10 data; there was some evidence from existing experimental results.

The data flows through the model are illustrated in Fig. 4.9.

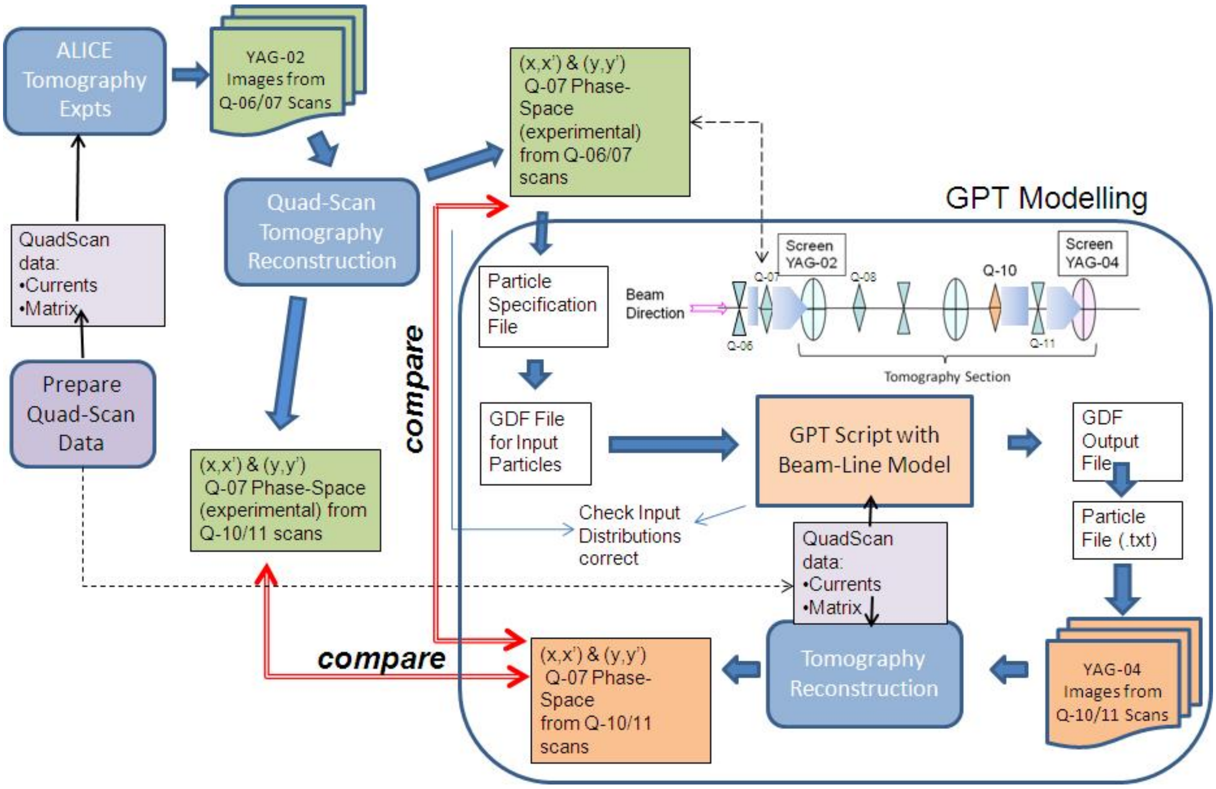

Figure 4.9: Data flows for the integration of the GPT tomography section model into an overall simulation of the tomographic measurement process are illustrated, indicating where comparisons with experimental results from ALICE may be made, particularly between QUAD-06/07 and QUAD-10/11 scans.

4.2.2 Generating Input Particle Specifications for GPT

To use GPT for investigating tomography results from measurements taken at different points along the ALICE to EMMA Injection Line, it was decided to feed back existing experimental data by converting it into realistic input for the GPT model of the line. In this way, the outputs generated by GPT, in particular the simulated screen profiles, could be used in their turn as inputs for full tomography measurement simulations, enabling studies to be made of the sensitivity of the method to various beam-line parameters, as shown in Fig. 4.9.

Input Data Earlier tomography experiments had provided measurements of both horizontal and vertical phase-space distributions (x, x') and (y, y') under similar beam conditions. Beam profiles had also been taken from screen YAG-02, which is reasonably close to the chosen reconstruction location for phase-space, and could therefore be used to approximate the (x, y) distribution matching the (x, x') and (y, y'). Several processing schemes were considered, based on using some or all of the available experimental data; however, it was found difficult to reconcile the measured (x, y) and the $(x, x'), (y, y')$ distributions simultaneously into a single consistent (x, y, z, x', y', z')

assembly (where the longitudinal coordinates z and z' are not correlated with x or y).

Processing Stages A MATLAB code (based on original work by K Hock) was developed to read in phase-space distributions and beam profiles, in their original formats, and produce output of particle specifications, as a text file. This text data could then be suitably formatted for a GPT utility program to convert into internal representation, making it available for import by a GPT simulation script. The principal steps in the code are as follows:-

1. Read in and prepare files for the (x-y) beam image, and the x and y phase-space distributions
2. User selects a window, to include the beam image region only
3. Apply filter and threshold, to smooth and suppress background
4. Find common x and y ranges in (x, y) and (x, x'), (y, y') distributions
5. Calculate Cumulative Distribution Function (CDF) for x in (x, y) distribution
6. Derive the CDF for y in (x, y), as a function of x
7. Similarly, determine the CDF(x) from (x, x'), and CDF(x') for x, and correspondingly CDF(y) and CDF(y')
8. Choose a random value from the x distribution, then choose a random x' corresponding to the chosen x
9. Repeat the above 2 steps for random y and y'
10. Display a scatter plot of (x, x') and (y, y') for random particles, as a check (see Fig. 4.10)
11. Adjust units if needed, and output $[x, y, z, x', y', z']$ for each particle, as a text file

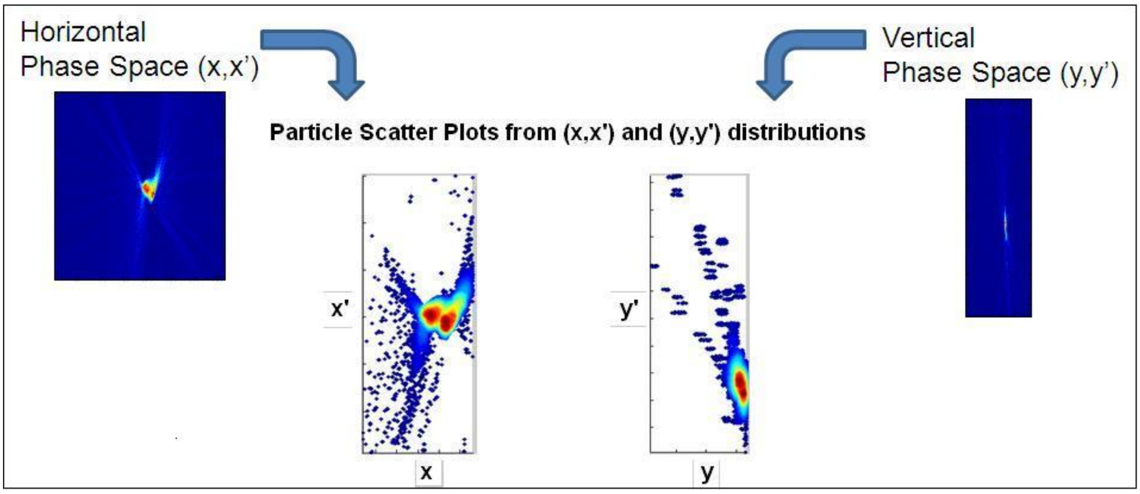

Figure 4.10: (x, x') and (y, y') phase-space distributions from separate experiment are combined to generate particle specifications suitable for input to GPT. As a check, the resulting particle set is visualised as two scatter plots.

A GPT batch file then converts the text representation of the particle set (Table 4.1) into internal (GDF) format. Here, columns x, y, z are coordinates for individual particles uniquely identified by 'ID', and GBx, GBy, GBz are the corresponding momenta conventionally known as x', y', z'. In this form, particles can be read in by the GPT script which describes the beam-line, and the resulting GPT output plotted at a position near the start of the line. This is to check that the phase-space distributions are as expected, given the known input of specified particles.

# GPT Particle File: E:\...\GPT\GPT2mat\ImageFileDir\0403 EMI-2 12ns.PNG						
ID	x	y	z	GBx	GBy	GBz
1	-1.242e-03	-5.015e-05	0.000e+00	-2.601e-04	1.068e-03	0.000e+00
2	-5.354e-04	-1.034e-04	0.000e+00	9.444e-04	-1.455e-04	0.000e+00
...						
99999	-5.445e-05	1.726e-04	0.000e+00	1.561e-03	-1.341e-03	0.000e+00
100000	-1.014e-03	-9.200e-04	0.000e+00	-7.407e-05	3.410e-04	0.000e+00

Table 4.1: In GPT, a particle set for input may be specified in a standard text format, giving values for (x, y, z, x', y', z'). In this example, the header and the start and end of a 100,000 particle set are shown.

Limitations in the Method The conversion of phase-space measurements into particle descriptions for GPT is subject to a number of uncertainties, which would reduce confidence in the results of GPT simulations based on them.

i) Quality of Measurements. Reconstruction resolution should be as high as possible, given the number of projections and the image pixels available.

ii) Positional Discrepancies in Data. (x, y) profiles are of necessity measured at a screen position, whereas (x, x') and (y, y') phase-spaces are typically reconstructed at a quadrupole entrance, such as QUAD-07. In this situation, profiles and phase-spaces cannot be reconciled directly, and a specification based purely on phase-space distributions might be preferable.

The availability of further ALICE experimental tomography datasets would enable some of these effects to be estimated, and provide options for their reduction.

iii) Correlating (x, y) and (x, x'), (y, y') Distributions. It is found from the GPT output, derived from the generated particles, that the resulting (x, y) profile does not correspond to the original experimental (x, y) profile. This effect is shown in Fig. 4.11.

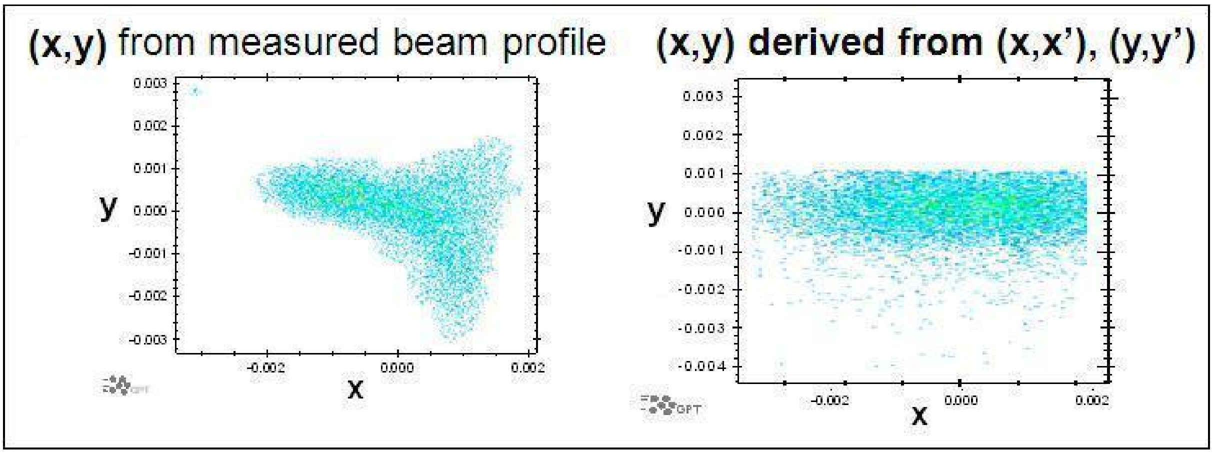

Figure 4.11: Using the output of GPT, a direct comparison is made between the (x, y) profile, measured experimentally, and (x, y) for the particle set as derived from the (x, x'), (y, y') distributions. They are distinctly different.

Possible Solution The issue of the unknown correlation between (x, x') and (y, y') could be addressed if the results of a full **4-dimensional** tomography measurement were available, yielding the (x, x', y, y') distribution directly. The theory of such measurements has already been investigated, and future experiments based on it are planned [47].

GPT Particle Input: the Approach Selected

In view of the problems encountered in specifying input particle sets, it was decided that as a simplification, Gaussian distributions would be assumed for both (x, x') and (y, y') phase-space, which are supported as standard by GPT. The transverse distributions would thus be fully characterised by the Twiss parameters $\beta_x, \alpha_x, \beta_y, \alpha_y$ and the emittances ϵ_x, ϵ_y. Realistic estimates of the parameters were already available from analysis of experimental tomography data using the methods described in Section 3.1.

4.2.3 Validation of Method of Input of Particles to GPT

A number of tests were carried out to verify that the specification of particles input to the GPT model were as expected. This was to increase confidence in the tomography model as a whole, illustrated in Fig. 4.9, of which GPT was a key component. These test methods included:-

1. Comparison of GPT inputs with measured outputs from GPT utility programs (known as GDFA modules) which calculate emittance ϵ and Courant-Snyder (Twiss) parameters β, α directly
2. Empirical analysis of GPT particle data (exported in text format), extracting emittance and Twiss parameters by applying the equations of Section 3.1.1
3. Analysis of tomographic reconstructions of phase-space, from screen image sets generated by GPT quadrupole tomography scanning, using the Section 3.1.3 method
4. Independent beam-size quadrupole-scan analysis (fitting a parabolic function) using the method described in Section 3.2.1

Table 4.2 shows the results of testing GPT Output against Input, using Method 1; values in the ‘GPT Input’ column should match corresponding values in the first ‘GPT Output’ column (at the Start):

	GPT Input:	GPT Output (from GDFA):		
Position	Start	Start	QUAD-07	YAG-02
(m)	at 0.006	at 0.006	at 0.295	at 0.631
Parameter				
α_x	0.1139	0.0678	-2.46	-2.66
β_x (m)	0.1295	0.128	0.851	2.32
α_y	-2.2797	-2.31	-1.62	-6.55
β_y (m)	1.109	1.14	1.99	5.28
ϵ_x (m-rad)	4.33 x 10^{-7}	4.51 x 10^{-7}	4.51 x 10^{-7}	4.51 x 10^{-7}
ϵ_y (m-rad)	9.03 x 10^{-8}	9.40 x 10^{-8}	9.41 x 10^{-8}	9.42 x 10^{-8}

Table 4.2: Set values for parameters $\beta_x, \alpha_x, \beta_y, \alpha_y$, and ϵ_x, ϵ_y, are input to GPT at the Start position. The function GDFA is used to calculate the parameters at other positions; specifically, ϵ_x, ϵ_y are expected to be conserved.

Table 4.3 contains the results of testing with Method 4. It should be noted that in this case, only the vertical (y) data is meaningful, as the quadrupole scanned (QUAD-06) is vertically-focussing; also, to reduce uncertainty the input emittances have been increased by a significant factor from the realistic values in Table 4.2. Good agreement is seen in all 3 parameters, within the limits of precision of the fitting technique used in the quadrupole-scan method, and its assumption of a ‘thin-lens’ model for the quadrupole, probably not fully justified in this case.

	GPT Input:	Quadrupole-Scan Beam-Size Analysis
Position (m)	Start at 0.006	
Parameter		
α_x	0.1139	
β_x (m)	0.1295	
α_y	-2.2797	-2.44
β_y (m)	1.109	1.13
ϵ_x (m-rad)	1.084 x 10^{-5}	
ϵ_y (m-rad)	2.256 x 10^{-6}	
$\gamma\epsilon_y$ (m-rad)	55.19 x 10^{-6}	55.56 x 10^{-6}

Table 4.3: For a given set of input parameter values, GPT is used to scan a vertically-focussing quadrupole (QUAD-06). Beam profiles from extracted (x, y) GPT particle data are used in the 'quadrupole-scan beam-size analysis' method to derive β_y, α_y and $\gamma\epsilon_y$, to provide independent validation by comparison with the known inputs.

Because GPT keeps track of all particles as they move along the beam-line, it provides for output, at any selected position, in terms of particle coordinates in phase-space. In this way, a visual check may be made to ensure that the developing beam is as expected, according to the beam input parameters. For the ALICE tomography line, a reference position at the entrance to the quadrupole QUAD-07 was chosen, for all four types of quadrupole tomography scan modelled. Plots are shown in Fig. 4.12, where 'H' in the Scan column refers to Horizontal phase-space (x, x') and 'V' to Vertical (y, y'). Quadrupole magnets are identified in Fig. 4.5.

	Scan	**QUAD-06**	**QUAD-07**	**QUAD-10**	**QUAD-11**
GPT	V	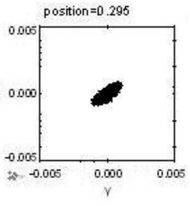			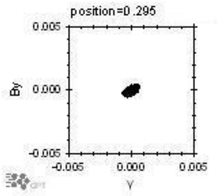
GPT	H		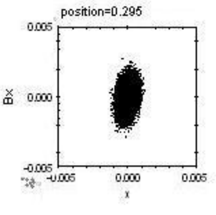	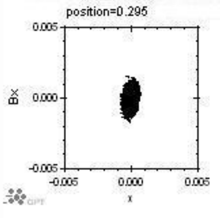	

Figure 4.12: GPT supports the visualisation of phase-space at any selected 'screen' position, here chosen as the QUAD-07 entrance. Checks are made that distributions related to different quadrupole scans are similar, both in the horizontal and the vertical.

It will be seen from Fig. 4.12 that as expected, the shape of the horizontal phase-space is the same in case of both QUAD-07 and QUAD-10 scans, as is the shape of the vertical for QUAD-06 and QUAD-11 scans. The size of the distribution appears reduced for the two quadrupoles further down the line (QUAD-10 and QUAD-11).

4.3 Summary

In this chapter, the particle tracking code GPT has been introduced and its fundamental principles briefly described, with the various built-in models for incorporating space-charge effects. After a first simple demonstration of space-charge causing an initially parallel beam to diverge along a drift-space, a more rigorous benchmarking exercise based on bunch radius is reported. This directly compares the results of an analytical calculation with the equivalent GPT results, for a uniform and for a Gaussian bunch. The required inputs and outputs for running GPT models, and the user interface, are outlined. A systematic investigation of space-charge, using the RMS beam-size as a metric, applied to a full ALICE tomography section model in GPT, is presented. Plots of high/low charge beam-size difference against quadrupole current and screen position are shown, highlighting regions of rapid change. A check is also made to see the expected convergence of beam-size difference with number of particles simulated, setting a lower limit for accurate modelling.

GPT is then incorporated into a comprehensive model of the phase-space tomography process, starting with the generation of initial particle specifications based on previous experimental results. Detailed steps in the creation of GPT input particle files are given, and some limitations of the process discussed. The methods used to verify that inputs are actually as specified, by matching to outputs, are summarised with tabulated examples. GPT plots of phase-space made from its internal data are included. Discussion of simulated reconstructed output is postponed until Chapter 5, where it is compared with the corresponding experimental data.

Chapter 5

Space-Charge Experiments and Data Analysis

Introduction

To carry out experimental investigations of the effects of space-charge in ALICE, which had already been predicted in simulation, preparations were made for a systematic study. The phase-space tomography experiments were to use some or all of the facilities of the diagnostic section of the ALICE to EMMA injection line. To support these experiments and to improve the quality of results, a number of modifications were also proposed to the camera systems used for screen image capture. This chapter describes the preparation and experiments, and discusses the findings, including investigatory work into an important anomaly discovered between results from sets of scans expected to be consistent.

5.1 Detailed Space-Charge Experiments (Phase 3)

In Phase 3, screen imaging cameras were prepared by fitting optical filtration for intensity control. Tomography experiments were planned and performed to measure horizontal phase-space in detail for a study of space-charge effects, using analysis results for calculating emittance and Twiss parameters.

5.1.1 Camera Filter Installation

Saturation Problem Increased bunch charge gives rise to higher peak image intensity on the cameras viewing YAG screens. Limited storage capacity of individual pixels (with 8 bits $\equiv$ a maximum of 256) can lead to 'saturation' if the maximum is exceeded. The resulting distortion of image projections due to this peak truncation, shown in Fig. 5.1, will invalidate tomographic reconstructions derived from these images; saturation is therefore to be avoided. Unfortunately this is not easily achieved on the very simple ALICE cameras due to their fixed aperture and exposure settings, and optical filtration is therefore required if the beam intensity itself cannot be reduced.

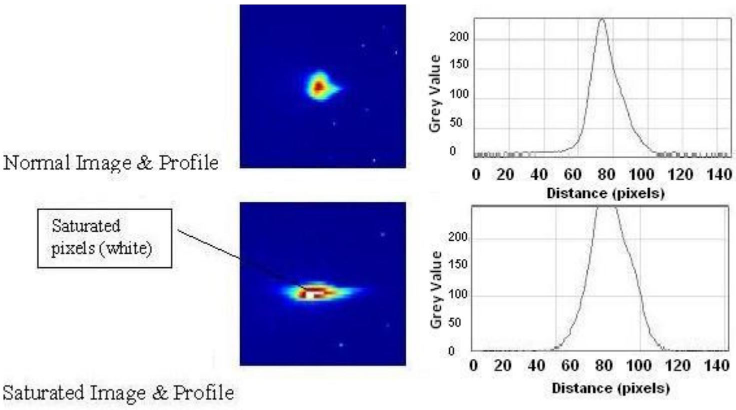

Figure 5.1: In the upper beam image, the plot of the profile through the intensity maximum has a well-shaped peak. The lower image, however, shows a distinctive white central region which appears in the profile as a flattened (truncated) peak. This is a characteristic sign of pixel saturation.

Beam Image Intensity Installation of fixed filters with 1% transmission, attached directly to the camera lens mountings, was tried but this reduced the signal/noise ratio in images excessively, as shown in Fig. 5.2. The intensity could be recovered only by operating with increased bunch train length (multi-bunch mode), whereas single-bunch was the preferred mode. One reason is that in a train the first bunches are typically of lower intensity than later ones; this effect causes a problem in estimating the 'effective' bunch charge.

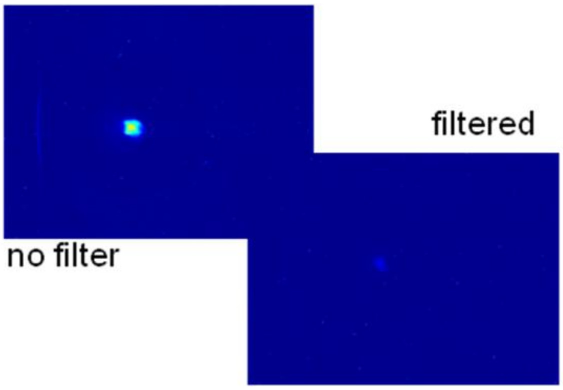

Figure 5.2: For the upper left image the camera has no optical filtration. In the lower right there is a filter over the lens, through which the transmission of visible light at 546 nm is only 1%.

5.1.2 Measurement Design and Setup

Comparative Scan (Bunch-Charge Dependence) Experiments: Theory

A 'comparative' method of using quadrupole tomography scans was devised, to demonstrate that space-charge could have observable effects within the Tomography Section

itself. At the same time, space-charge effects in the earlier sections of ALICE, which were to be expected in any case, would be compensated for.
The principle is as follows:

- Scan at 2 different quadrupole/screen combinations within the section, designated 'A' and 'B', having a significant separation down the beam-line.
- Repeat the A and B measurements at a range of bunch charges (from Lowest to Highest attainable).
- Reconstruct phase-space from A and B data at the **same** reference location, and compare the A and B results (see Fig. 5.3.

The expected outcome is:

- A and B should produce similar phase-space distributions at low charge.
- Increasing differences between A and B at high charge should be observed, due to effects such as space-charge in the region between the 2 measurement screens.

Configuration of Beam-Line The reference position for reconstruction of phase-space, which must be the same for both scans, is chosen in conjunction with the two quadrupole-screen combinations. Of course, the scanned quadrupoles must have the same polarity, e.g. both 'focussing' for horizontal phase-space measurements.

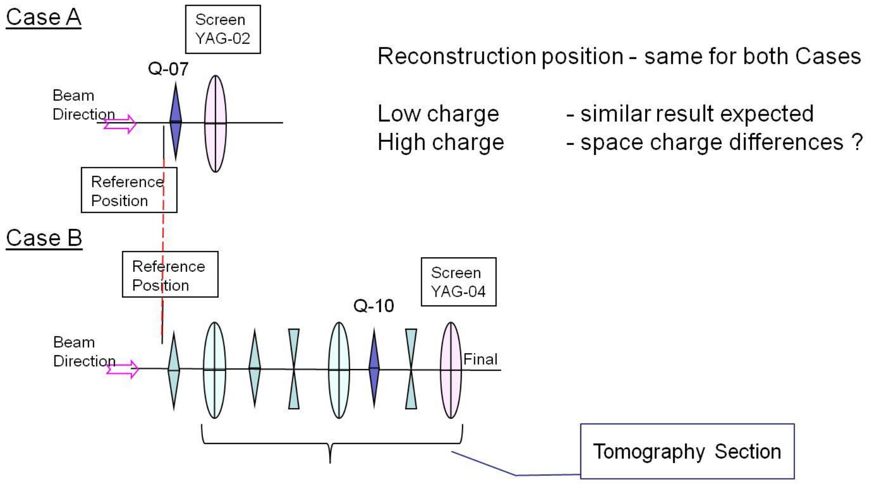

Figure 5.3: In the comparative scan experiment, the quadrupole chosen to be scanned for Case A is at the start of the tomography section (QUAD-07). For Case B, a quadrupole of similar orientation, but later in the line, is selected (QUAD-10). In both cases, the reconstruction reference position is the same.

Selection of Optimum Quadrupoles for Scans The best two combinations found for quadrupole, screen, and reference position, at the standard beam energy of 12 MeV (kinetic), are listed in Table 5.1.

Case	Quadrupole ID	Screen ID	Reference Position
A	QUAD-07	YAG-02	entrance of QUAD-07
B	QUAD-10	YAG-04	entrance of QUAD-07

Table 5.1: The best combination of scanning quadrupole and imaging screen has been selected for the two experimental cases: 'A' = short beam path; 'B' = long beam path. The reference position for reconstructing phase-space is the same for both.

Input Data Preparation As part of the selection process for suitable quadrupoles/screens, calculations were also made to determine the quadrupole currents required to provide sets of regularly-spaced tomographic projection angles, using the methods of Section 2.3.2. For the best reconstruction quality, these projections attempt to cover, as nearly as possible, a full 180^o range. Angle and current plots for the quadrupole selections in Table 5.1 appear in Fig. 5.4 and actual ranges achieved are shown in Table 5.2.

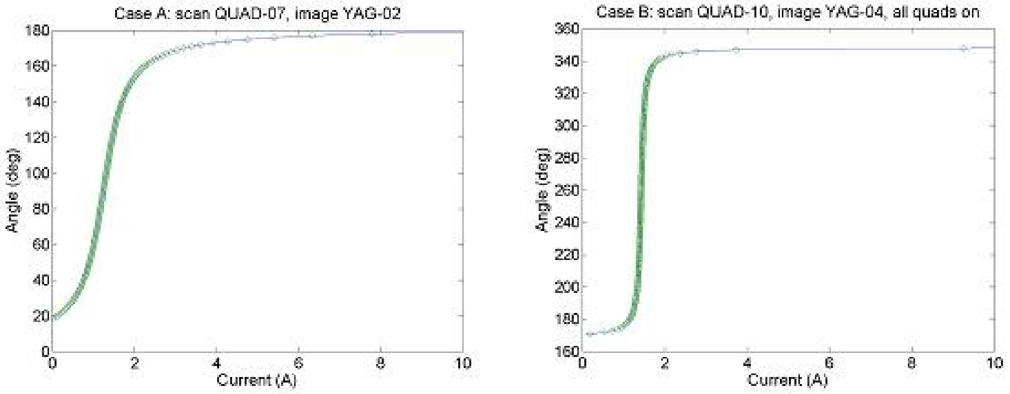

Figure 5.4: For each of the quadrupole/screen combinations (Cases A and B), tomographic projection angle θ is plotted against scanned quadrupole current. General curve characteristics are similar, although the actual angular ranges achieved ($\Delta\theta < 180^o$) are somewhat different.

Scan	QUAD-07/YAG-02	QUAD-10/YAG-04
Angles	$18.55^o - 178.91^o$	$170.83^o - 348.04^o$
Range	160.36^o	177.21^o

Table 5.2: Minimum and maximum projection angles, and angular ranges, have been calculated for the two quadrupole tomography scans (Cases 'A' and 'B') corresponding to the plots in Figure 5.4.

Results of Reconstruction

For all quadrupole tomography scan dataset reconstructions, the FBP algorithm has been used exclusively. Results are tabulated, by scanned quadrupole and by bunch-charge, in Fig. 5.5. In the columns for the 'fitted' distributions, which are derived from the 'raw' phase-space using the method of Section 3.1.3, their RMS phase ellipses as described by Eq. 3.3 are overlaid in white.

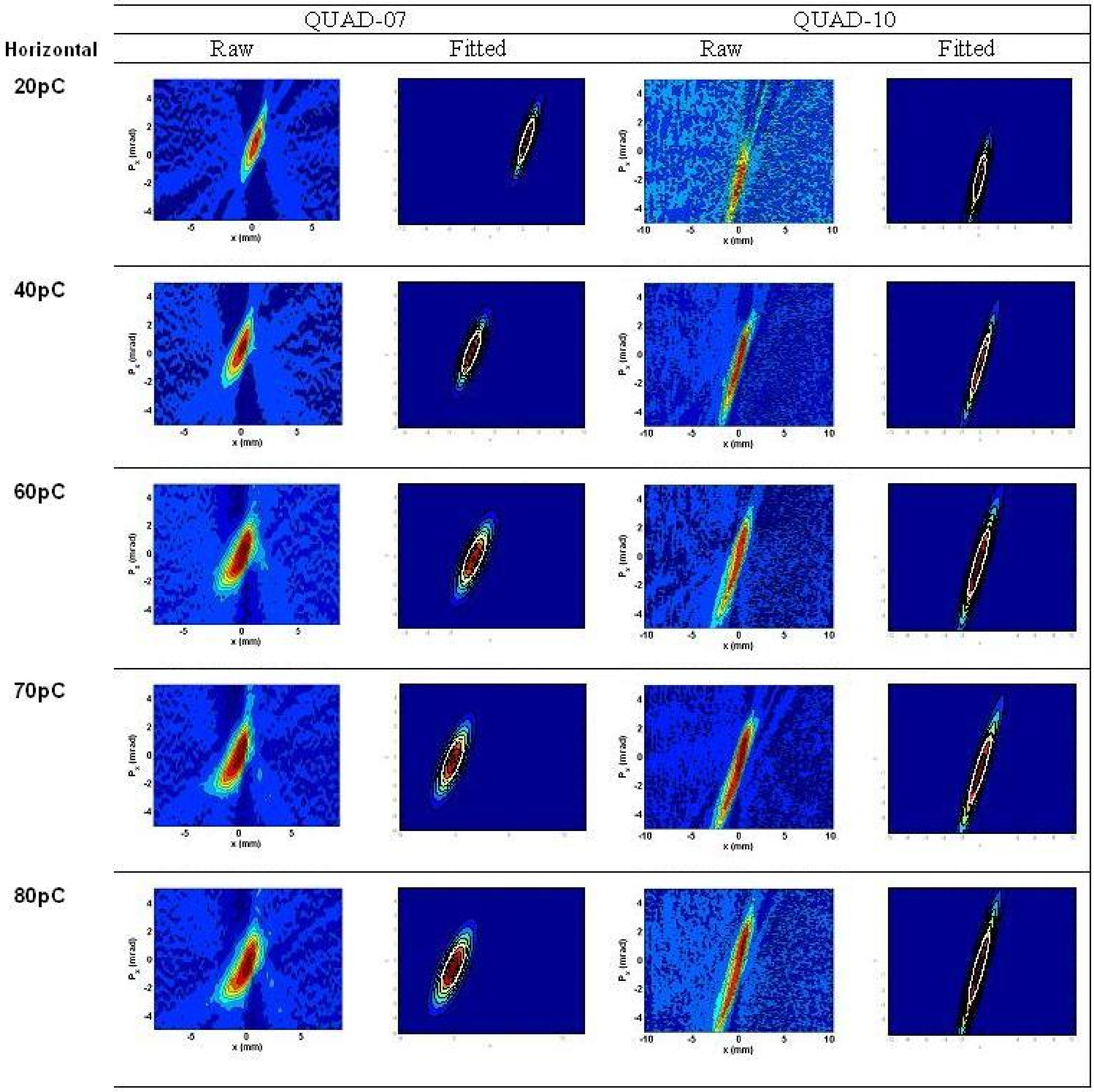

Figure 5.5: Reconstructed phase-space distributions from experiments are tabulated by quadrupole scanned (columns) and by bunch-charge (rows). Raw data on the L has the Gaussian-fitted result on its immediate R, overlaid with a white RMS ellipse.

5.1.3 Analysis of Space-Charge - Part 1: First Evidence from Tomography Experiments

The initial series of experiments within Phase 3, designed to detect space-charge effects through tomography have been described in Section 5.1.2; the phase-space reconstructions are tabulated in Fig. 5.5, in which the bunch-charge increases from top to bottom.

For all reconstructions, the emittance ϵ and Twiss parameters β and α were extracted from the distributions by fitting 2-D Gaussian functions to the data, using the method of Section 3.1.3. These plotted fits are shown in separate columns of Fig. 5.5, headed 'Fitted'.

5.1.4 Results of Analysis of Bunch-Charge Study Experiment

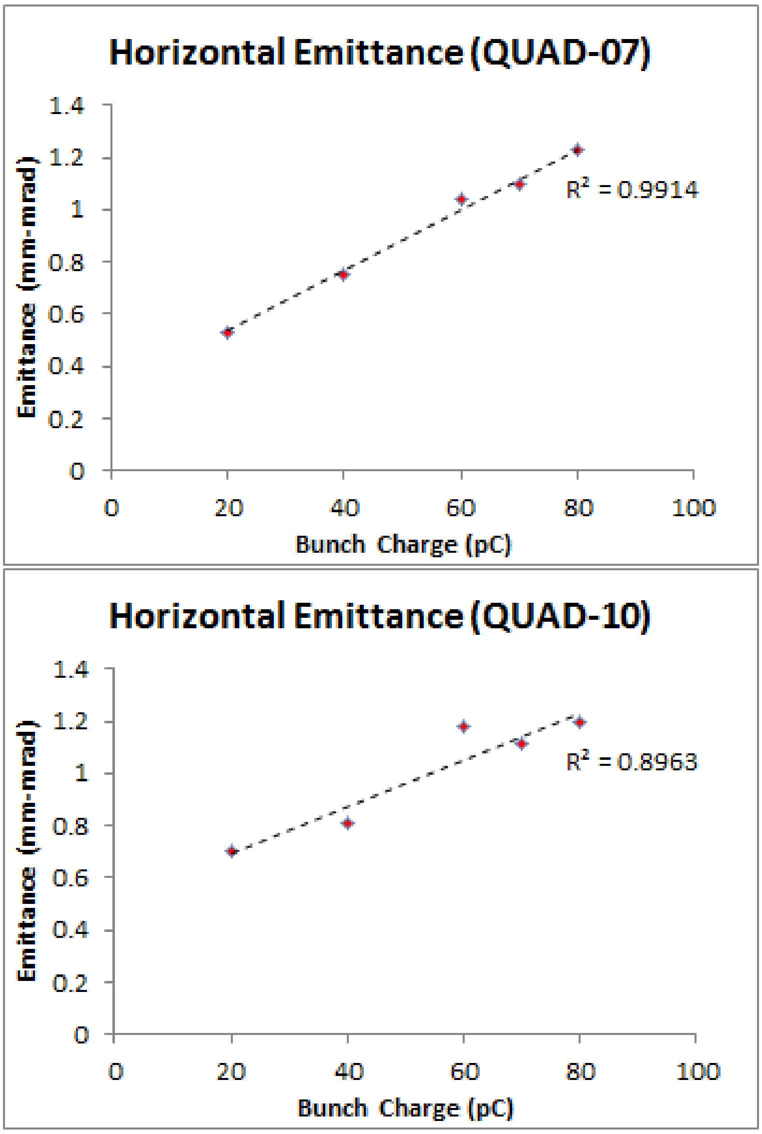

Figure 5.6: Horizontal emittance, derived from fitted distributions, is plotted against bunch-charge to compare results of QUAD-07 tomography scans with QUAD-10 scans. Straight-line fits have been added for trend indication only; R^2 indicates goodness of fit, with $R^2 = 1$ being perfect.

A systematic rise in emittance, measured at QUAD-07, is observed in both the QUAD-07/EMI-02 and the QUAD-10/EMI-04 screen data, as bunch-charge at the ALICE injector is increased. The trend in the data points of Fig. 5.6 suggests that straight-line fits are appropriate, although this has no specific theoretical justification.

For both of the quadrupole measurement datasets (QUAD-07 and QUAD-10) the horizontal emittance as determined by tomography demonstrates a rising trend with increasing bunch charge, as illustrated when they are plotted together in Fig. 5.7. However, the difference between the two cases has no statistical significance, the plots appearing to converge above 70 pC charge. For lower charge, image intensity is reduced and noise has a greater contribution to measurement uncertainty.

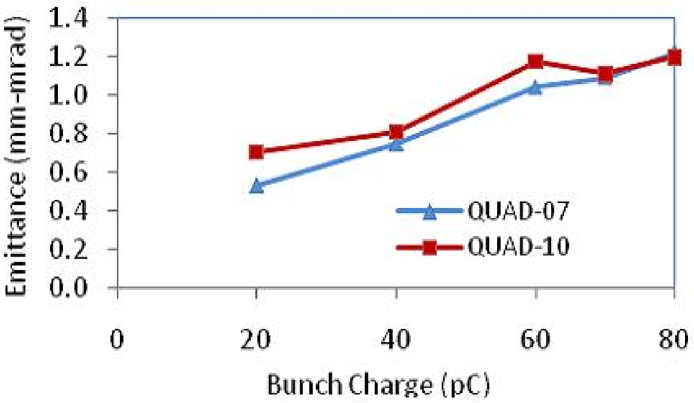

Figure 5.7: Horizontal emittance ϵ_x from analysis of tomography using QUAD-07 is compared directly with ϵ_x from QUAD-10 tomography scans, plotted on the same axes against bunch charge. The trends are clearly similar and there is an apparent convergence at higher charge.

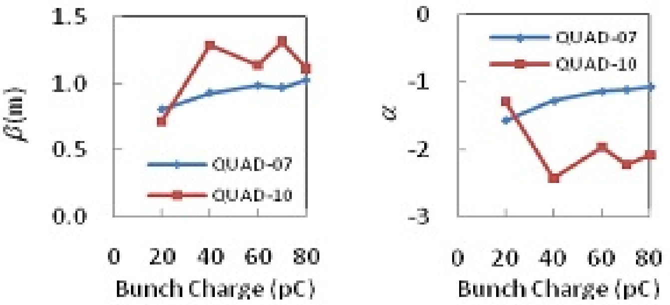

Figure 5.8: The Twiss parameters β (L) and α (R) from tomography data analysis are compared for QUAD-07 and QUAD-10 results, plotted against bunch charge. For QUAD-07 the trend is more obvious than for QUAD-10.

In Fig. 5.8, the Twiss parameter data for QUAD-07 in both α and β has a slow and consistent rising trend with bunch charge; however the QUAD-10 values show much more scatter. One possible explanation could be the accumulation of uncertainties - in the case of QUAD-10 - in the various quadrupole current values which combine in evaluating the transfer matrix between the position of reconstruction (QUAD-07 entrance) and the imaging screen (YAG-04). It is not possible to conclude that there is a systematic difference in the α and β values (evaluated at the same reference point) for the two quadrupole tomography scans.

From this tomography study there is no detectable evidence for the dependence of emittance on space-charge effects in the tomography section itself, which would be supported by a significant difference in the two plots in Fig. 5.6. It was concluded that further more sensitive experiments would be required to detect any subtle effects of space-charge on the phase-space distribution.

Incidentally, these results did suggest that it could also be useful to carry out further investigations into the relationship between bunch-charge and emittance growth at the ALICE electron gun and in the beam-line just beyond. It would be of interest, moreover, to define the best procedure for optimisation of emittance with respect to bunch-charge in the ALICE injector optics, particular for key parameters such as solenoid SOL-01 current and buncher gradient settings. Such work was considered, however, to be outside the immediate remit of the current tomographic study.

5.2 Further Space-Charge Studies (Phase 4)

At Phase 4, camera image acquisition was improved by fitting remote filter-changers. The study of the effects of space-charge using the same method as Phase 3 was extended to include vertical phase-space tomography, experiments being designed to complement simulation work being performed in parallel, in the particle tracking code GPT.

5.2.1 Experimental Proposal

Further tomography experiments were planned as part of ALICE operations within the Accelerator Physics beam-time allocation. The principal objectives were:-

i) to verify the results of earlier tomography work and demonstrate reproducibility and consistency;

ii) to investigate the effects of space-charge in detail, in both horizontal and vertical phase-space;

iii) to improve measurements with '3-screen' tomography (as illustrated in Fig. 6.1 and described in Chapter 7, and so allow a fair comparison with other methods (e.g. quadrupole tomography scanning).

The same approach of 'comparative scans', as in the previous experimental Phase and described in Section 5.1.2, was to be adopted.

Data Preparation To meet Objective ii), new input data to support quadrupole tomography scans was prepared, by adapting existing codes to generate new magnet current settings for different quadrupoles, imaging screens, and tomographic reconstruction positions, as summarised in Table 5.3. This allowed measurements to be made of phase space in both the horizontal (H) and the vertical (V), based as in earlier experiments on scans at the start and the end of the ALICE tomography section.

Phase Space	Quadrupole	Imaging Screen	Reconstruction Position	Angles
H	QUAD-07	YAG-02	QUAD-07 Entrance	160
V	QUAD-06	YAG-02	““	167
H	QUAD-10	YAG-04	““	177
V	QUAD-11	YAG-04	““	179

Table 5.3: Extending Table 5.1, the selections of quadrupole and screen for both horizontal (H) and vertical (V) phase-space tomography scans are listed, including the number of 1^o projection angle intervals accessible.

5.2.2 Camera Filter-Changer

Filter Changer A 3-position mechanism for remotely changing glass neutral-density filters between screen and camera lens was fitted to the ALICE cameras in the tomography section. The set of filters selected for the tomography section cameras had 10% - 3% - 1% transmissions, based on a study of average image intensities. It should be noted that to provide a 100% (straight-through) option would have occupied one of the three filter positions, limiting the effective choice to 2 filters only.
The ability to select filters allows improved optimisation of the signal/noise ratio in images for the most commonly-used screens, provided that the transmission values of the filters are appropriately chosen.

5.2.3 Results of Phase-Space Reconstructions

The experimental tomography scan data for both horizontal and vertical phase-space was reconstructed, with the reference position for all distributions being at the QUAD-07 entrance.

In the horizontal, QUAD-07 and QUAD-10 scans were compared, for bunch-charges of 5, 10, 20, 40, and 52.6 pC, the latter being the maximum achievable charge at full laser power (i.e. with minimum laser attenuation). The two sets of reconstructions are shown side-by-side in Fig. 5.9, reading in column order by increasing charge.

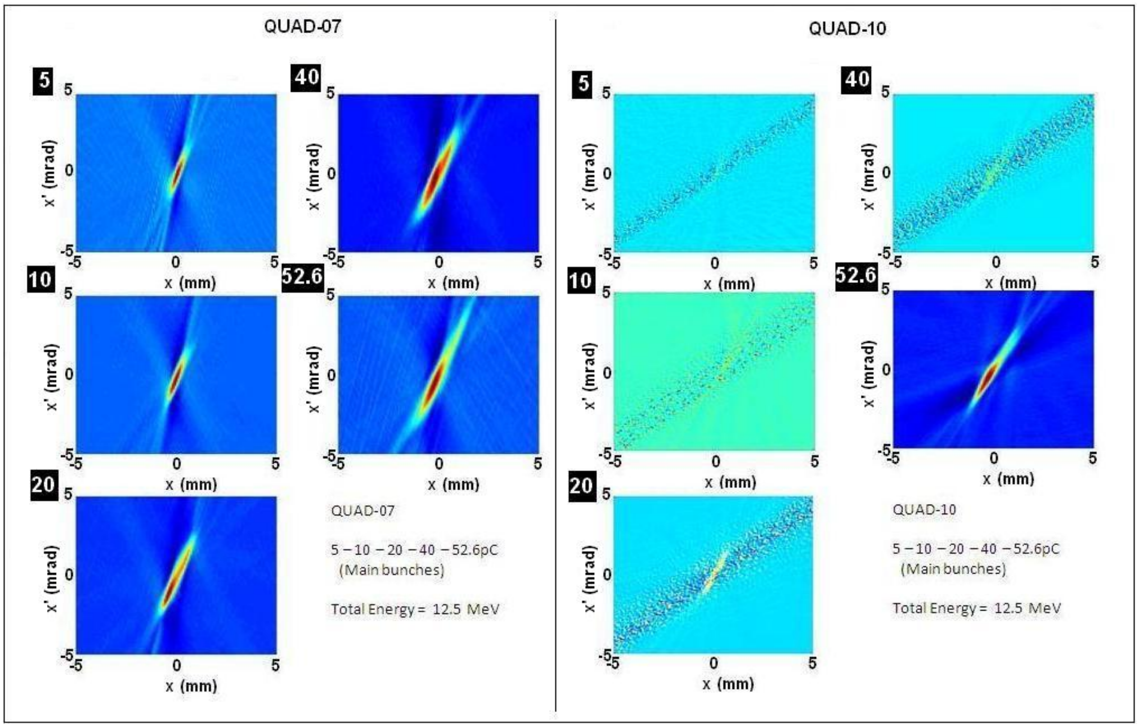

Figure 5.9: Reconstructed horizontal phase-space distributions are arranged, labelled in order of increasing bunch charge from 5 to 52.6 pC at 12.5 MeV (total energy), to compare QUAD-07 results (L) with QUAD-10 (R).

In Fig. 5.9, the reduced quality of the reconstructions in the QUAD-10 case, compared with QUAD-07, may be ascribed at least partly to a combination of increased camera noise and lower image intensity, as a different screen/camera system is used.

In the vertical, QUAD-06 and QUAD-11 scans were compared, for the same range of bunch-charges as the horizontal. These are shown in Fig. 5.10.

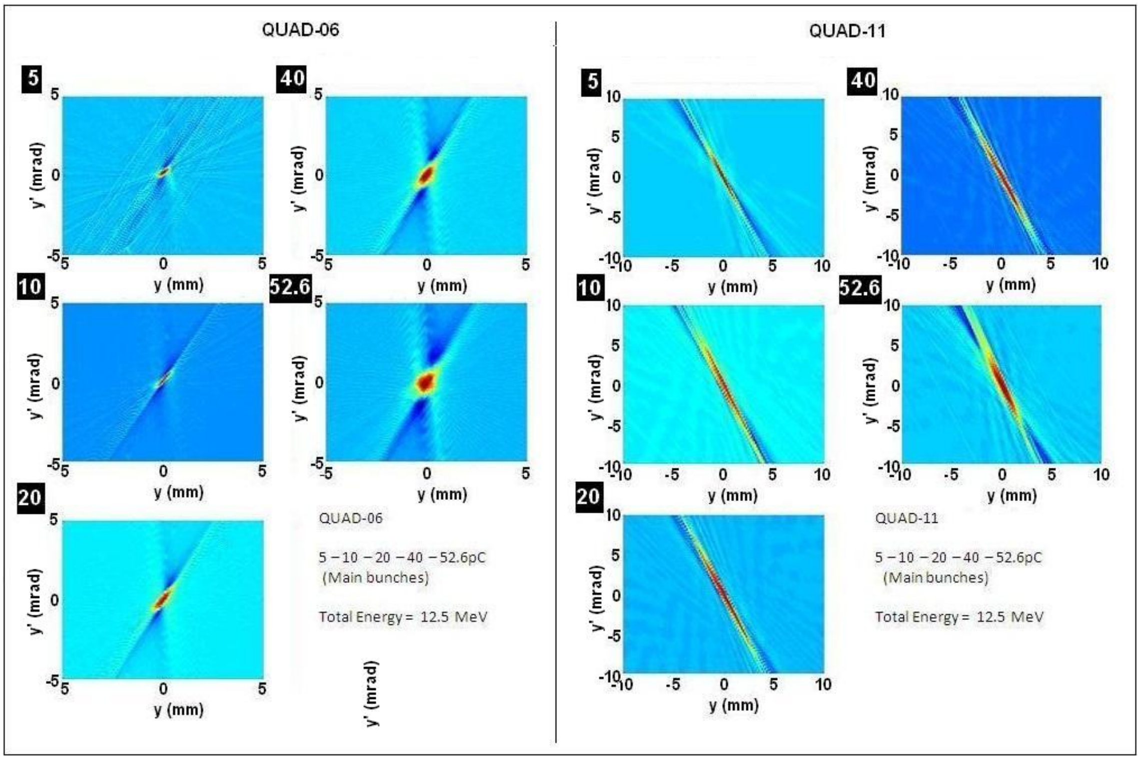

Figure 5.10: Reconstructed phase-space distributions in the vertical are arranged in bunch charge order from 5 to 52.6 pC at 12.5 MeV (total energy). Although results for QUAD-06 and for QUAD-11 are separately consistent, there is a clear discrepancy when comparing one with the other, at all charges.

5.3 Analysis of Space-Charge - Part2: Evidence from Further Experiments and Comparison with Simulation

The second series of 'comparative space-charge' experiments, denoted Phase 4 and described in Section 5.2.1, have their reconstructions shown in Fig. 5.9 for horizontal phase-space and in Fig. 5.10 for the vertical. These results are now considered in more detail.

Horizontal There is a general trend of increasing emittance, as shown by a growth in the central distribution with bunch-charge. A close similarity in shape is seen between corresponding phase-spaces measured with QUAD-07 and with QUAD-10, at the same bunch-charge. This is clear even though the QUAD-10 results are considerably noisier than for QUAD-07, especially at lower charges; this is evident in the Fig. 5.11 plots, which show a more consistent trend with bunch-charge for QUAD-07.

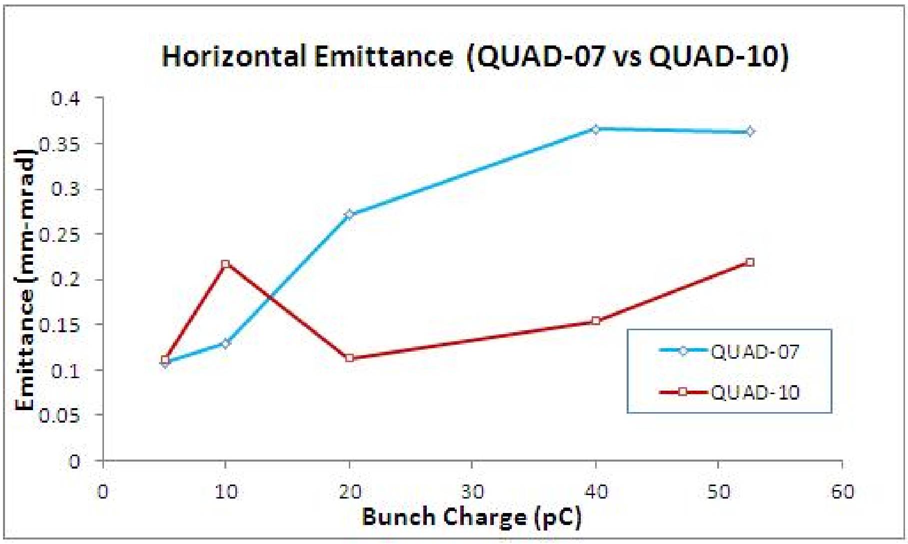

Figure 5.11: Horizontal emittance growth with bunch charge is plotted to compare QUAD-07 with QUAD-10 data. The less consistent trend for QUAD-10 may be a consequence of higher levels of reconstruction noise.

Vertical The trend of emittance growth with bunch-charge, shown in horizontal phase-space, is also seen in the vertical, plotted in Fig. 5.12. This occurs both in the QUAD-06 and in the QUAD-11 reconstructions. However, the most obvious difference is the clear dissimilarity between QUAD-06 and QUAD-11 distributions, in all beam parameters. Both shape and orientation are distinctly different.

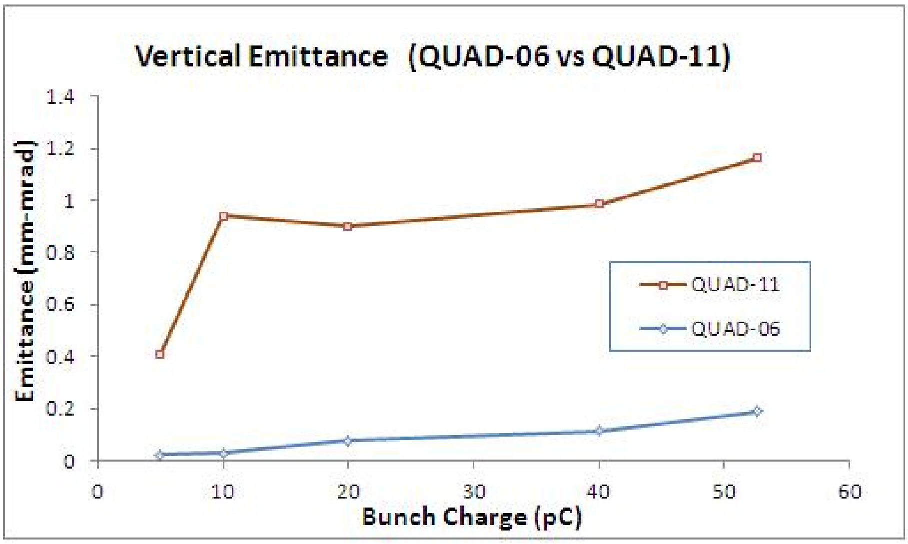

Figure 5.12: Vertical emittance also grows with bunch charge as seen in results from QUAD-06 and QUAD-11. The difference in the trend of the two datasets is very marked, reflecting the clear distinction in their phase-space distributions.

5.3.1 Vertical Phase-Space: Investigations into Discrepancies

The apparent anomalies in the vertical phase-space results from experiment clearly required further investigation if any meaningful conclusions about consistent space-charge effects were to be made. The corresponding results from GPT simulation, already presented in Section 4.2, strongly suggested that the anomaly was genuine and associated with the vertical data only. One obvious common factor in the generation of both experimental and simulated results was use of the same MATLAB-based processing and tomographic reconstruction software, and this was therefore subjected to scrutiny.

In Fig. 5.13 a direct comparison is made between experiment and GPT simulation at an energy of 12.5 MeV, simplifying matters by taking the case of minimum bunch-charge (5 pC) so that any space-charge effects can be neglected.

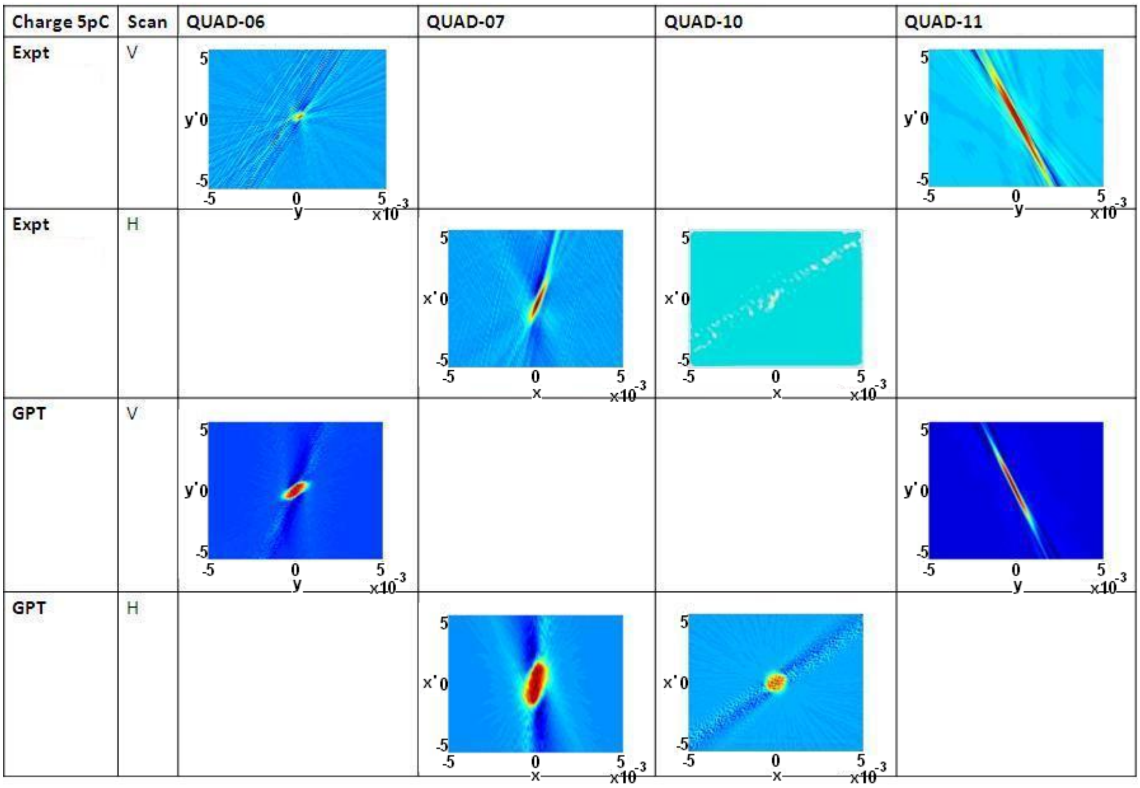

Figure 5.13: Collation of reconstructed phase-space distributions enables a comparison of experimental results with corresponding GPT simulations, both in the horizontal (QUAD-07 & QUAD-10) and the vertical (QUAD-06 & QUAD-11). Selected data is for 5pC charge, to minimise any space-charge effects which could make comparisons less valid.

It should be noted that results could be influenced by possible differences in initial conditions between model and simulation, in particular the assumption - in the case of the GPT model - that the starting bunch has a Gaussian distribution. Nevertheless, good agreement is observed between experiment and GPT in the orientation and general shape of the reconstructed distributions, particularly for the QUAD-06, QUAD-07 and QUAD-11 results; for QUAD-10 comparison is more difficult, as experimental data is affected by noise. This agreement can be taken as evidence of freedom from gross inaccuracy in the model, and could be further improved by incorporating more detail into the initial bunch distribution; in the simulation, initial particles are specified purely by their aggregate properties, emittance and Twiss parameters, not in detail.

Proposed Explanations

Several possible sources for the observed discrepancy in vertical phase-space have been considered, including:

Errors in the Lattice The dimensions of drift spaces or strengths of quadrupoles between the measurement screen and reconstruction location which contribute to the transport matrix, and therefore to reconstructed phase-space, could be incorrect.
This was considered unlikely, as the relevant differences would apply only to the section between QUAD-10 and QUAD-11, and QUAD-10 scans apparently gave 'correct' results. The values were checked in any case and no errors found.

Reconstruction Process Parameters The phase-space input at the start of the tomography section could be shown to be as expected, at least in simulation; but the reconstruction did not agree. Among the parameters affecting imaging, projection, and therefore the results of tomography, are the number of projections/images, and the number of positions/projection samples.

Reconstruction Algorithm The standard tomographic reconstruction method used for these studies is 'Filtered Back Projection' (FBP); however, some alternatives have already been mentioned in Section 1.6.2, specifically the 'MENT' technique which is described in more detail in Section 7.1. A short investigation has therefore been made to determine whether the anomalies in the phase-space distributions from QUAD-06 and QUAD-11 scans for the same reconstruction reference point, which are expected to be identical but are distinctly different, could be reconstruction-method-specific.
A typical experimental dataset for vertical phase-space was selected, consisting of tomography scans with QUAD-06 and QUAD-11, at 40 pC bunch-charge in order to provide good-quality clear beam images as raw input data. Of the 159/179 images available, a sample of 5, uniform in projection angle, was taken to avoid possible convergence problems in MENT with large datasets. It was decided that to facilitate direct comparison, the same sample would also be processed using FBP. The established preprocessing steps as in 2.3.2 were carried out, with the addition of 'threshold correction', as explained in Section 3.1.4, without which MENT can sometimes prove unstable. A

threshold of 0.1 × peak projection height was found by experiment to be satisfactory. The results in Figure 5.14 show phase-space reconstructed using MENT, compared with that using FBP. It is clear that in spite of the strong artifacts in the FBP reconstructions, which tend to obscure the outlines and which are largely absent from MENT, there is an obvious similarity in both shape and orientation. These results should also be viewed alongside the corresponding cases in Figure 5.10, which show the FBP reconstructions of the *full* datasets.

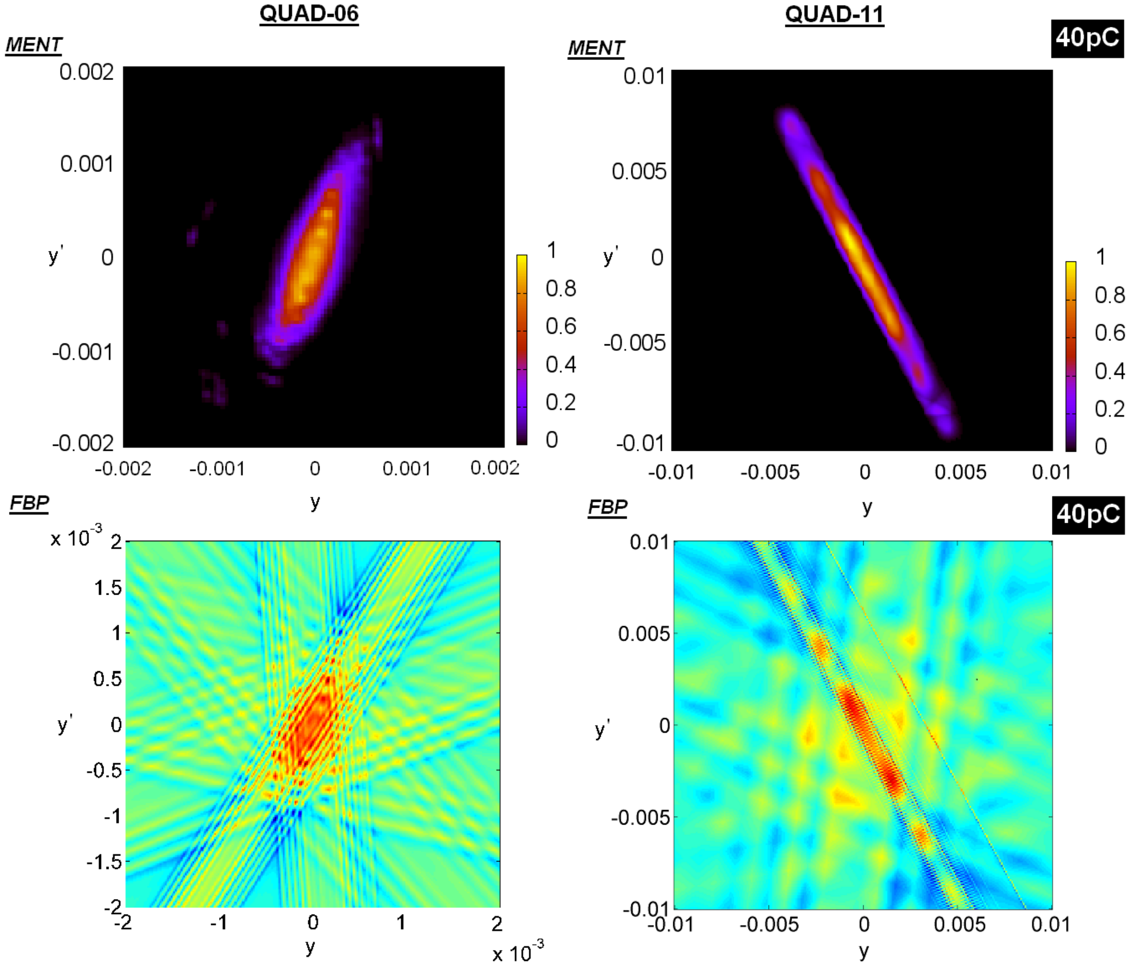

Figure 5.14: Vertical phase-space reconstructions using the MENT method, using reduced experimental datasets sampled by only 5 projections, are compared directly with the same data using FBP. No significant difference may be observed either in the case of QUAD-06 or of QUAD-11, and the ‘anomaly’ between the two quads remains.

It may be concluded even from this very simplified study that there is no evidence that the reconstruction algorithm alone is a significant factor in the observed discrepancy in vertical phase-space calculated from QUAD-06 and QUAD-11 tomography scans. However, as we expect phase-space measured at the same point from both quadrupole tomography scans to be identical, we may deduce that the difference is due either to a deficiency in the input data or pre-processing which is common to both algorithms, or to a shared lack of robustness under certain conditions; and that it appears to be specific to the vertical phase-space.

Evidence for Solution

Using an independent computer simulation code for generating projection sets (due to Dr K Hock), it was found that the resolution of the projections, that is the number of positions at which they are sampled, which is determined ultimately by the raw image pixel size, could have a major effect on the resulting reconstruction, particularly its orientation. This effect was checked in GPT simulation by increasing the image resolution by 25 times in both x and y dimensions, but the results were not conclusive; further investigation will be required.

Unfortunately, experimental confirmation of the influence of resolution has not been directly possible at the time of writing, because it is strictly limited by the number of pixels available on the installed cameras, which is currently fixed (572 × 768).

5.4 Summary

This chapter has dealt with the planning, preparation, results and analysis of tomography experiments designed specifically to investigate space-charge effects in the ALICE diagnostic section. The use of optical filters to overcome camera saturation in beam images is considered, with examples. The principle of 'comparative' quadrupole tomography scans for the detection of local space-charge effects is explained and the experimental configurations described, with the preparation of input data. For the first phase of these experiments, the reconstructions of phase-space are presented, both in raw form and as Gaussian fits, organised by bunch-charge for each scanned quadrupole. The results of analysis in terms of horizontal emittance and Twiss parameters are plotted against charge, and the conclusion is drawn that although positive effects are unproven, the evidence is not conclusive.

Proposals are listed for a further experimental phase, extended to include vertical phase-space, with details of a more advanced remote triple filter-changer for the screen cameras. Experiment results for the horizontal QUAD-07 and QUAD-11 scans are presented for comparison, then the vertical QUAD-06 and QUAD-10 scans are compared. In the analysis and discussion of trends, these experimental results are brought together with the corresponding simulations previously described in Chapter 4. An obvious discrepancy between the vertical phase-space from QUAD-11 and QUAD-06 scans is highlighted and explanations proposed; results of an investigation using the alternative MENT reconstruction method are described; and finally, evidence for a possible solution is given.

Chapter 6

Normalised Phase Space

Introduction

Beam tomography measurements are usually carried out in terms of ‘real’ phase-space (x, x'). However, if a specially-chosen normalising transformation is applied, the resulting ‘normalised’ phase-space is found to possess some useful properties. These can be related to the design of multi-screen tomography beam-lines, and confer advantages over working in ‘real’ phase-space in certain situations. The practicalities of making such measurements are discussed, and example results are given.

6.1 Normalised Phase-Space Technique

Normalisation of Phase Space It can be shown that there exists a transformation of the ‘real’ phase-space (x, x') - considering just the horizontal for the present - with the property that between two different positions on a beam-line, the betatron phase advance becomes equal to the angle of rotation of the transformed phase-space. This has become known as ‘normalised’ phase-space (x_N, x'_N) and the transformation is defined by the matrix equation:

$$\begin{bmatrix} x_N \\ x'_N \end{bmatrix} = \begin{bmatrix} \frac{1}{\sqrt{\beta}} & 0 \\ \frac{\alpha}{\sqrt{\beta}} & \sqrt{\beta} \end{bmatrix} \begin{bmatrix} x \\ x' \end{bmatrix} \tag{6.1}$$

where β, α are the Twiss parameters at the relevant position.

Firstly, ‘normalisation’ for beam tomography implies that if several fixed screens (i.e. 3 or more) are used to generate different projections of the beam, from which the underlying phase-space distribution may be reconstructed, then arranging for equal betatron phase advances between screens will ensure that projection angle intervals are also equal. This is shown in Fig. 6.1 for the design settings of the ALICE to EMMA injection line [8]. An advantage of this is the avoidance of a type of reconstruction artifact which occurs when angle steps are unequal, particularly for the FBP algorithm. The same equal intervals can also be arranged when using the alternative ‘quadrupole tomography scan’ technique, by setting the magnet currents appropriately.

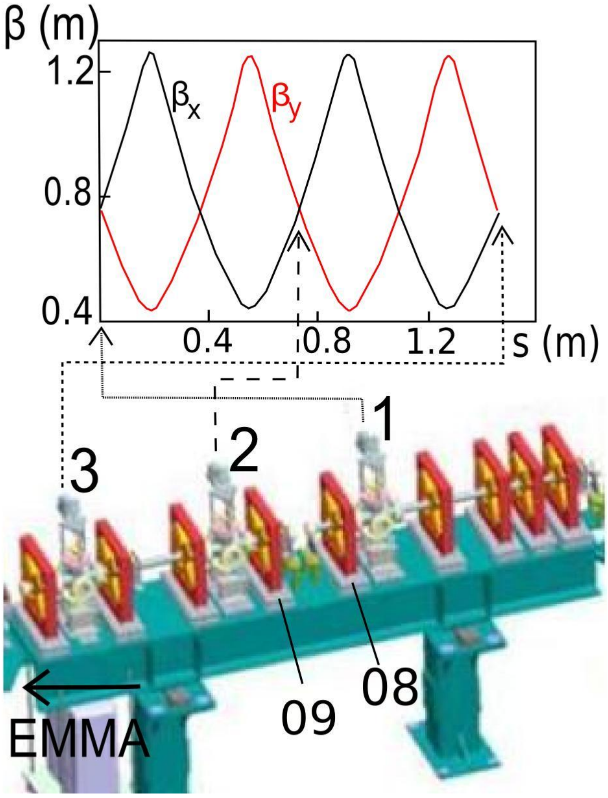

Figure 6.1: The tomography section of the EMMA Injection Line was designed so that when appropriately set up, the beta functions β_x and β_y would be periodic, having equal values at each of the screens numbered 1, 2, 3 (arrowed on the plot of β vs. distance s).

Secondly, when working in normalised phase-space, the expected distribution is - under ideal conditions - a circular shape rather than the usual ellipse. This does not change, except for a rigid rotation, if observed at other locations as the beam propagates down the line; in a sense, it is a 'global' representation of the beam properties.

In practice, to work in normalised phase-space, the standard 'real space' transfer matrix R, which is denoted as M in Section 2.1, between the reference/reconstruction position and the measurement point (i.e. screen), is modified by applying the 'normalisation matrix' N, derived by inverting Eq. 6.1:

$$N = \begin{bmatrix} \sqrt{\beta} & 0 \\ \frac{-\alpha}{\sqrt{\beta}} & \frac{1}{\sqrt{\beta}} \end{bmatrix} \tag{6.2}$$

As N is a function only of the lattice functions α and β at the reference point, it can be calculated given assumptions about the particle source and the known state of the beam-line elements up to this point, using a computer code such as MAD (see Fig. 6.2 (i)). This code facilitates the propagation of lattice parameters through arbitrary linear beam-line elements. A comprehensive discussion of normalised phase-space tomography will be found in [48].

It is the derived matrix $R_n = RN$ which is then used in calculating the tomographic projection angles θ, where

$$\tan\theta = \frac{R_{n12}}{R_{n11}} \tag{6.3}$$

However, as the magnet settings actually used during an experiment are usually optimised to give the best beam imaging conditions, they are unlikely to coincide with the standard (or 'design') values of α and β used in the original calculation of matrix N; in addition, the actual beam source may have a different distribution to that assumed. Under these circumstances, normalisation will not be exact and will not generally produce a reconstructed distribution of the expected circular shape.

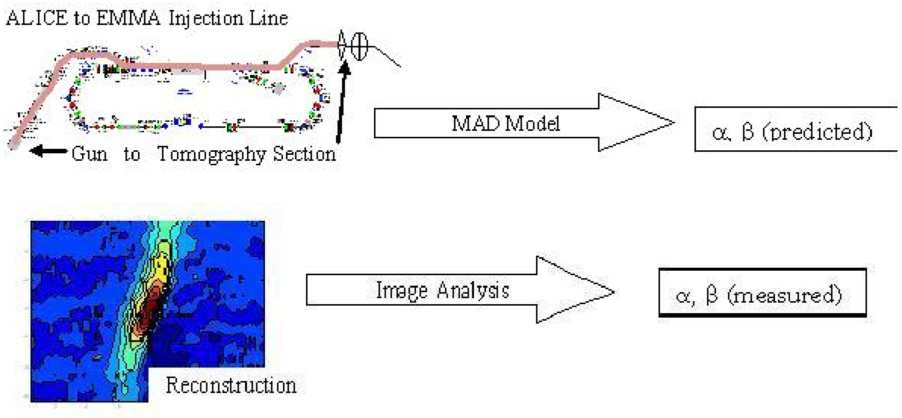

Figure 6.2: The values of α and β required to calculate the normalisation matrix may be obtained either by prediction from a MAD model of the full ALICE beam-line (top), or by measurement from an earlier tomography experiment (bottom).

A more realistic estimate of α and β can be obtained if a previous phase-space tomography reconstruction is available (see Fig. 6.2 (ii)). Ideally, the two sets of values (α, β) would be expected to agree, within the limits of experimental uncertainty.

A practical normalised tomography procedure could follow this sequence:-

- The actual values of α and β are estimated, using the methods of Section 3.2.1, or by the analysis in Section 3.1.1 using data from real (un-normalised) phase-space tomography at the reconstruction point. It should be noted that prior knowledge of matrix N is not required at this stage (see Fig. 6.2 (ii)).
- These Twiss parameters (α, β) are applied to build the normalisation matrix N, which is then used to derive the magnet settings which would give uniform steps in phase advance, from measurement point to screen(s).

- A repeat tomography experiment, this time in normalised phase-space, is carried out using these settings.
- We may expect a normalised phase-space reconstruction with an approximately circular distribution, as predicted by theory.

Prediction of Beam Twiss Parameters As an exercise, a composite model of the ALICE beam-line, from the booster exit up to the end of the EMMA Injection Line, was assembled from two existing MAD-8 codes (see Fig. 6.2 (i)). Experimental values for ALICE magnet settings were applied as input data to the MAD model, using magnet tables to calculate focussing strengths k at the given beam energy; and with reasonable values assumed for Twiss parameters α, β at the starting point (i.e. after the booster), the model was run to predict α, β at the measurement position in the tomography section. Knowledge of α, β would allow working in normalised phase-space, by applying the 'normalisation matrix' N in Eq. 6.2. Unfortunately, the experimental conditions were sufficiently different from the design settings (which had been assumed for the development of the original models) that the calculated α, β values were at best unrealistic, at worst beyond the acceptance limits of the MAD code.

Validation of Beam-Line Models It therefore became apparent that the value of such a model, based on the real lattice, may be found instead in predicting properties of the beam-line in the reverse sense. By working backwards, given the measured phase-space distribution and α, β parameters at the tomography location and applying a known lattice, the real (x, y) space distributions (i.e. beam profiles) may be predicted at any desired upstream position, then compared with experimental measurements made with YAG screens. As screen images at strategic points down the beam-line are collected and snapshots are taken of the lattice settings as part of routine operations, this data is available for analysis such as that described above, whenever required.

6.2 Measurements in Normalised Phase-Space

At several accelerators, including ALICE but also at the Photo-Injector Test Facility Zeuthen (PITZ), FLASH and others, tomography sections have been designed for equal phase advance between screens, a condition which would lend itself to working in normalised phase-space. Although not fully implemented as such, some of the effects discussed have been demonstrated in experiments at ALICE.

Example 1. In Fig. 6.3, an example distribution is plotted both in 'real' and in 'normalised' phase-space. The difference in scales should be noted when making comparisons. From the general appearance, obvious points are the ideal circular shape shown by the normalised plot, rather than the strong elongation of the real-space plot; and the much more detailed structure visible in the normalised scan (Note. Data analysis is taken from [49]).

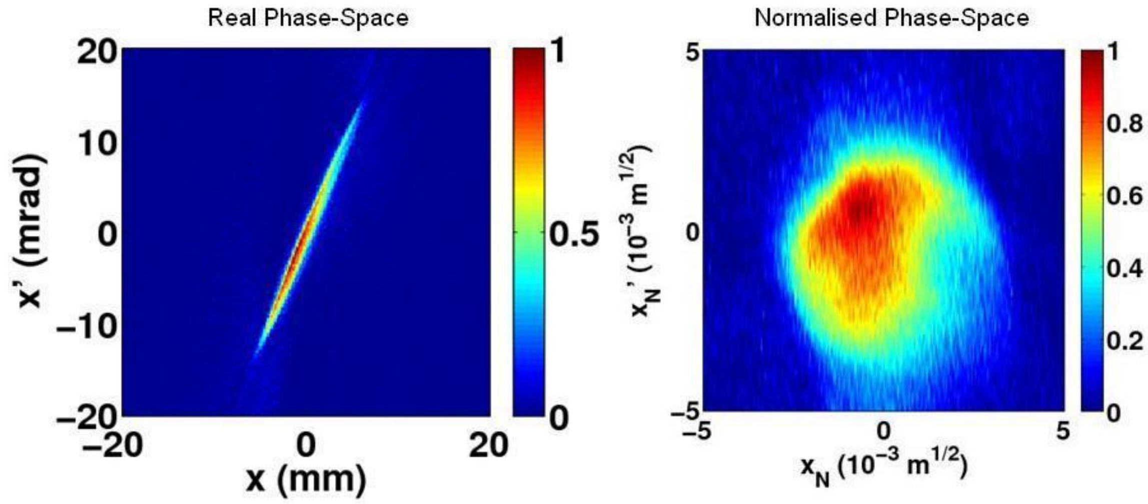

Figure 6.3: Example 1. The real phase-space distribution (L) is compared with its equivalent calculated in normalised phase-space (R), whose shape is close to the ideal circle (analysis taken from [49]). Axis units are changed accordingly.

Example 2. In contrast to Example 1, in Fig 6.4 little difference is seen between the results of the two types of tomography. This suggests that the assumed values of α, β used in the normalisation matrix N were not appropriate. Better results would have been obtained by applying the 'practical procedure' suggested above, starting with the 'real phase-space' reconstruction.

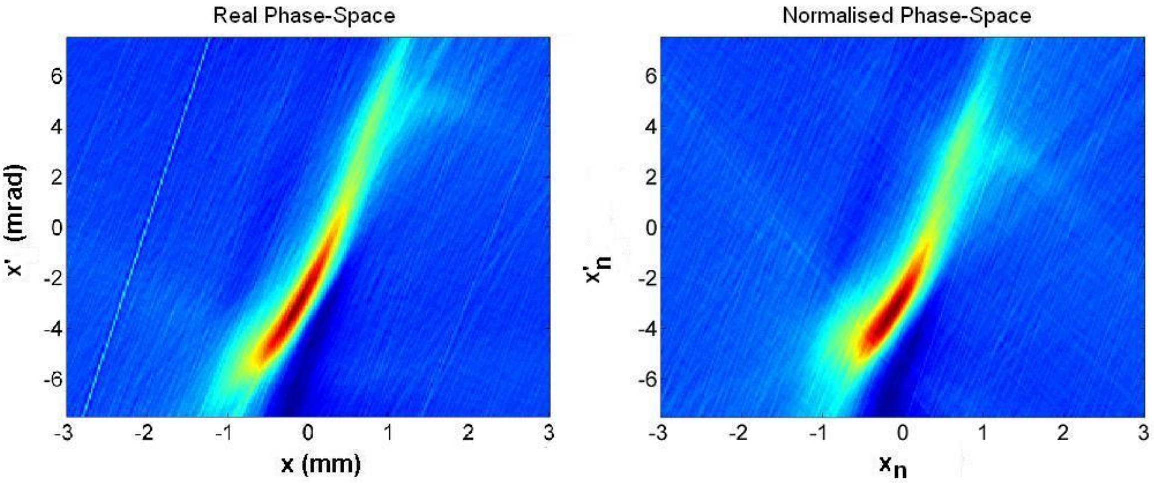

Figure 6.4: Example 2. In this example, the normalised phase-space (R) is only a little different when compared with the real phase-space (L). The predicted α, β values used were clearly not the appropriate ones.

6.3 Summary

In this chapter the concept of 'normalised phase-space' is introduced, as a linear transformation of the 'real' phase-space. It is placed in the context of the design of the EMMA injection line tomography section, which has three screens, and the phase advances between these screens. A practical process for working in the normalised phase-space is proposed. Methods of determining the normalisation matrix are discussed, either by beam-line modelling, or by calculating the Twiss parameters α, β using other techniques. The chapter ends by comparing two examples of real and the equivalent normalised phase-spaces, illustrating some of the possible benefits.

Chapter 7

Three-Screen Data: Reconstruction Approaches

Introduction

In general, the quality of phase-space reconstruction from the Filtered Back Projection (FBP) algorithm is much better if as many projections as possible can be acquired. With the quadrupole tomography scanning technique, it is usual to employ intervals no larger than 1^o, giving up to 180 projections. However, there are circumstances when the number of projections is strictly limited, as in the case of the so-called 'three-screen' tomography. The ALICE to EMMA diagnostic section illustrated in Fig. 6.1 was designed for this technique. Under these conditions, other algorithms can offer significantly improved reconstructions, and one which has been extensively applied to beam tomography is described in this chapter in more detail.

7.1 Outline of the MENT Algorithm

As previously stated in Section 1.6.2, the Maximum Entropy (MENT) technique belongs to the class of 'iterative' reconstruction algorithms. These work by converging to a solution via a series of successively better approximations, starting from some sensible initial estimate.

We start by considering projections of the unknown distribution in phase-space $f(x, x')$. Each of these N projections may be written as

$$p_n(s) = \int f(x_A, x'_A)dt \tag{7.1}$$

Referring to Fig. 7.1, the mapping between (s, t) and (x, x') is represented as

$$\begin{bmatrix} s \\ t \end{bmatrix} = A_n \begin{bmatrix} x \\ x' \end{bmatrix} \tag{7.2}$$

where A_n is the arbitrary linear transport matrix for the n^{th} tomography screen, relative to the plane of reconstruction.

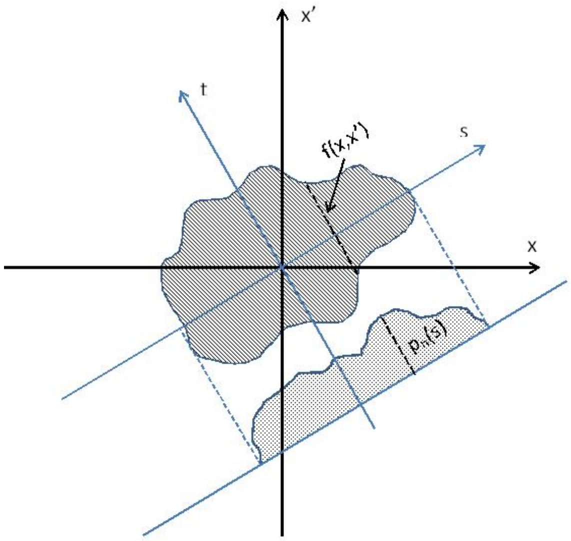

Figure 7.1: The measured data consists of a set of parallel projections of an unknown distribution $f(x, x')$, such as $p_n(s)$ which is the n^{th} projection and is onto the s axis.

The maximum entropy principle states that the most likely, i.e. ‘reasonable’, distribution is that which is produced naturally in the greatest number of ways. The term ‘entropy’ is used by analogy with statistical mechanics, from the resemblance to the Boltzmann distribution of particle energies. From a definition of the entropy H of the distribution $f(x, x')$

$$H(f) = -\int\int f(x, x')ln[f(x, x')]dxdx' \tag{7.3}$$

This formula may be derived by counting the different ways of distributing N particles over the M cells which make up the solution grid in phase space.

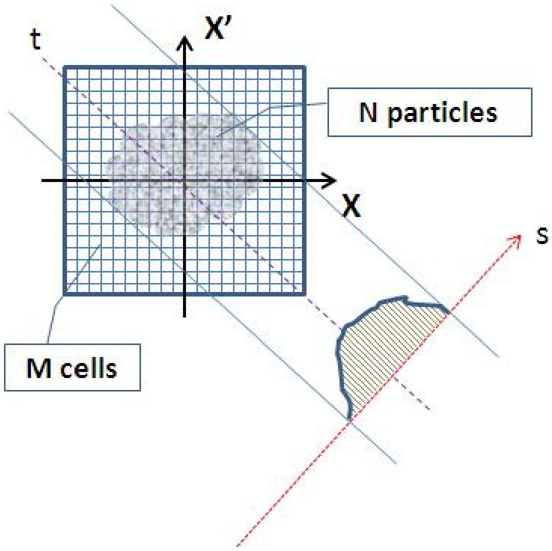

Figure 7.2: A proposed solution can be considered as a distribution of N particles over a rectangular grid of M cells, constrained by the observed set of projections onto s.

Without constraints, maximising entropy would naturally tend to a uniform distribution across the grid. The maximisation may be carried out using the method of 'Lagrange multipliers' $\lambda_n(s)$. Defining the unknown 'Lagrange factors' by $h_n(s) = \exp(J_n\lambda_n(s) - 1/N)$, where J_n is the Jacobian of the transport matrix A_n (normally $J_n = 1$ in situations of constant emittance), we obtain a simple product for the maximum entropy distribution:

$$f(x_A, x'_A) = \prod_{n=1}^{N} h_n(s_n(x_A, x'_A)) \tag{7.4}$$

Applying the constraints, which are defined by the projections in Eq. 7.1, to Eqn.7.4 by substituting for $f(x_A, x'_A)$, and factoring out $h_n(s)$, we obtain a set of N equations in the functions $h_n(s)$:

$$p_n(s) = h_n(s) \int \prod_{k \neq n}^{N} h_k(s_k(x_A, x'_A))dt \tag{7.5}$$

These equations may be rapidly solved for $h_n(s)$ by Gauss-Seidel iteration. This works by progressively refining $h_n(s)$ by repeatedly solving Eq. 7.5. Projections $p_n(s)$ calculated with this $h_n(s)$ from Eq. 7.1 are compared with the measured $p_n(s)$ at each iteration step. When the desired tolerance is achieved, the result is the required distribution $f(x_A, x'_A)$.

7.2 Comparison of MENT with FBP

It can be seen that with very limited numbers of projections, FBP reconstructions will by their nature always be dominated by strong artifacts. On the other hand, MENT is capable of producing clear distributions using just the same projection data. This is very obvious in Fig. 7.3, where the MENT reconstruction is taken from [49], using codes to be found in [29].

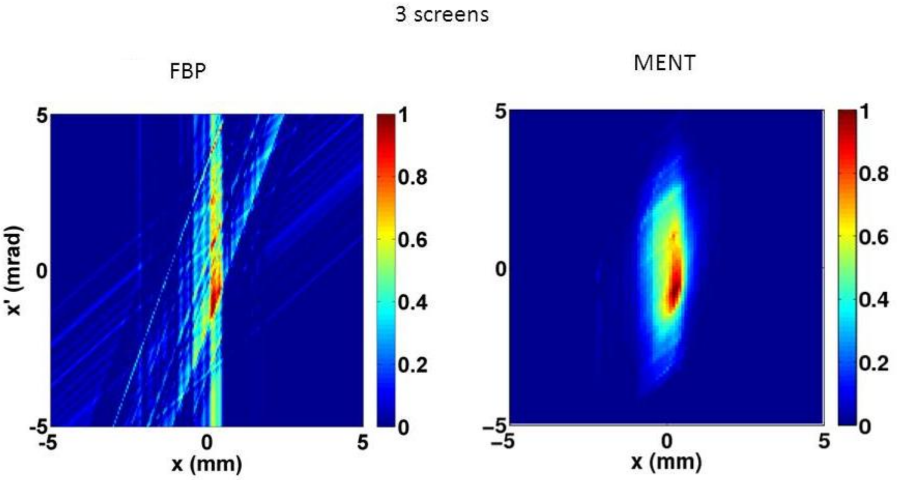

Figure 7.3: With image data from just 3 screens, the horizontal phase-space reconstruction using the FBP algorithm (L) is compared with the results of reconstructing the same data using MENT (R). The clarity and lack of artifacts is evident.

7.2.1 Problems with MENT

Although its reconstructions are apparently superior to other techniques, care must be taken as MENT can under some conditions introduce serious distortion, which might go undetected. This has been clearly demonstrated in simulation, where the original distribution is of course a priori well known [50].

Importance of Choice of Angles MENT can show a sensitivity to the projection angles selected. This is partly a consequence of the small number of projections: it is unavoidable that large intervals of angle are not sampled. In phase-space, distributions which are long and narrow should have their projection directions, also described as 'rays', concentrated along the principal axis. This is readily demonstrated by considering the simulated example of a simple Gaussian distribution in phase-space. When projections are taken at the three equally-spaced angles indicated by the 'rays' in Figure 7.4(a), the MENT reconstruction (b) based on the three projections is seen to be in very good agreement with the original.

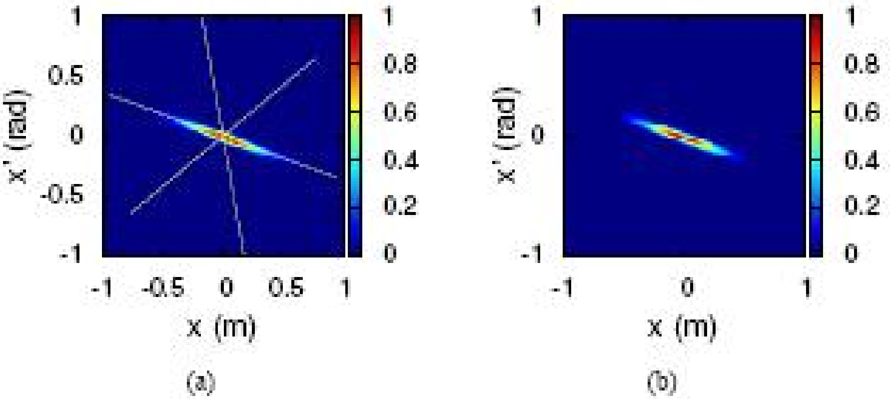

Figure 7.4: (a) Projections of a simple Gaussian phase-space example are taken along 3 rays at equally-spaced angles. (b) The MENT reconstruction from these 3 projections is shown to agree very well.

If however the chosen angles are rotated, as in Figure 7.5(a), it is now clear from the reconstruction (b) that it is significantly distorted. The cause is that the very limited set of projections fails to sample the distribution adequately, especially along its 'long' axis.

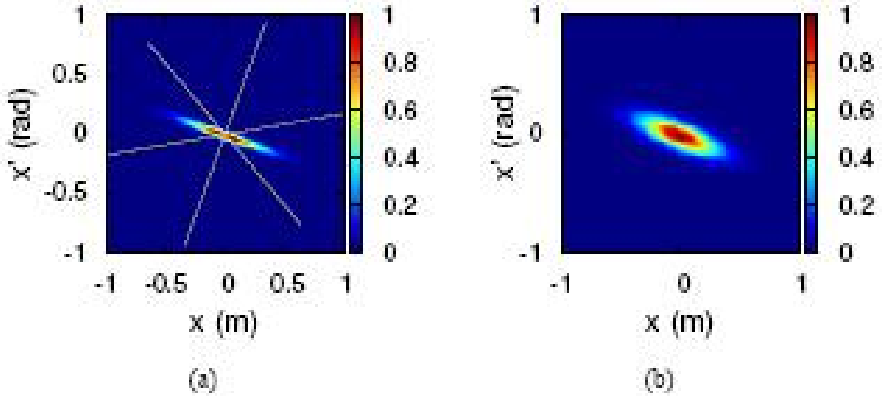

Figure 7.5: (a) The ray directions for projection are now rotated, while remaining equiangular. (b) The reconstruction with MENT still appears clean, but shows significant distortion compared with the original.

The solution is to choose angles which produce equal projection angle intervals in **normalised phase-space**, which is equivalent to arranging for equal phase advances between measurement screens, as explained in Chapter 6. This works even when, as in real life, we do not know the shape of the distribution beforehand.

In practice, setting screen-to-screen phase advances to be equal is rarely straightforward and requires a knowledge of the Twiss parameters α, β. Instead, the basic technique of quadrupole tomography scanning previously described in Section 2.3.2

may be used, to obtain a reasonable projection angle range, which though less than the ideal 180^o will still usually be adequate. A FBP reconstruction may then be made, and the Twiss parameters estimated. A small number of angles (e.g. 3 or 4) having intervals giving equal phase advance may then be selected from the angular range covered by the scan. For these angles, the corresponding projections are taken, and reconstructed using MENT. The results shows advantages over using FBP alone, in terms of freedom from artifacts and cleanliness of the background region of the distribution.

7.3 Limitations and Optimisation of MENT

MENT is not always guaranteed to converge to the ‘correct’ result, especially in the presence of excessive noise, or when projection values do not fall properly to zero within the limits of s_n. Methods such as the ‘thresholding’ techniques described in Section 3.1.4 may be beneficial in this case.

MENT is an iterative algorithm, and may sometimes fail to converge at all; that is, after a certain number of iterations the difference between successive calculated projections and the measured ones ceases to decrease. Even though the specified tolerance level has yet to be reached, no further improvement will be made regardless of how many iterations are run. For Gaussian distributions this problem has been found to occur when the number of projections exceeds about 10; however, any noise tends to decrease the limit, and for very noisy data there may be no convergence whatever limit is set.

In practice the problem is not serious, as MENT is generally applied only to very small projection sets, and measures already described may be used to reduce noise.

7.3.1 Implementations of MENT

For the work described here, an implementation of the MENT algorithm has been created in the ‘C’ language, supported by ‘Scilab’ scripts [29]. This version is very much a development tool, and does not therefore have an advanced user interface; on the other hand, it is very flexible.

A study of a publicly-available version of MENT, tested using real ALICE experimental data, is included in Appendix D [15]. As this code did not prove to have any particular advantages over the version developed in-house, no further use has been made of it to date.

7.4 Multiple-Screen Tomography

For ALICE tomography, the design method is to use just the three screens of the tomography section in the EMMA Injection Line. There is however no theoretical limit to the number of screens if more are available, although in practice on ALICE this is reached when the three screens in the remainder of the Line are included as well, making a total of six. The processing software has been designed to handle an arbitrary number of projections n, for FBP reconstruction these being at equal angular intervals, provided that the appropriate input data in the form of transport matrices $[M_1...M_\mathrm{n}]$ has been prepared. A comparison has been made to determine whether the use of further screens confers any measurable advantage.

Type	**Screens/ Projections**	**Ref Point**	*Reconstruction* Units: x in mm. x' in mrad.
Multi-Screen	3 Screens: EMI-2 EMI-3 EMI-4	EMI-02 YAG	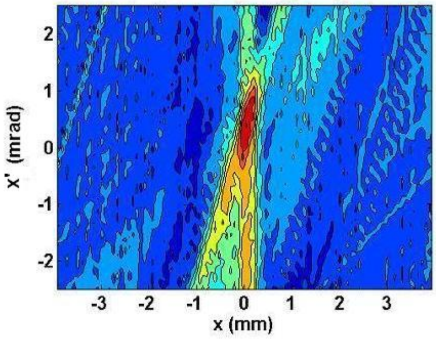
Multi-Screen	6 Screens: EMI-1 EMI-2 EMI-3 EMI-4 EMI-5 EMI-6	EMI-01 YAG	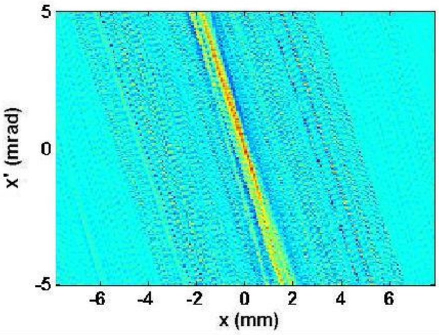

Figure 7.6: Tomography with 3 screens as shown (Top) may be extended by including additional screens available before and after the tomography section itself; the effect of 6 screens on reconstructed phase-space is seen (Bottom). In general, screen locations will not be ideal with respect to equality of projection angle intervals.

In Fig. 7.6 the reconstructions, both from the FBP algorithm, appear quite different in character as well as shape. For the '3 screens' case in the upper plot, the very limited projections produce prominent linear artifacts emanating from the centre. For the '6 screens' below, the background noise has a higher spatial frequency, but there is no obvious improvement in definition, mainly due to the unfavourable range of projection angles covered ($\ll 180^o$). Also, the line has not been designed or set up specifically for six-screen tomography, and the angle intervals, which are functions of the beam-line transport matrices, will not be equal and therefore less than optimal for the FBP algorithm.

Moreover, in the example of Fig. 7.6, distributions are not expected to be identical because:-

- reference positions for reconstruction are different for the two measurements;
- beam-line magnet settings are not standardised and depend on machine state, energy etc. at the time of the experiment.

Other accelerators making use of phase-space tomography and referred to in Section 6.2 have been designed with multiple screens: PITZ (× 4 screens) [12]; PSI (× 3 to × 5) [15]; SNS (× 5) [14]; TRIUMF (× 3). MENT is used as the algorithm of choice at these sites.

7.5 Summary

This chapter has considered the Maximum Entropy Tomography (MENT) algorithm as an alternative approach to reconstruction when there are as few as three screen projections available. The mathematical theory of MENT is outlined, and a comparison is made between example data reconstructed using MENT and the standard method, Filtered Back Projection (FBP); the clear advantages are shown. Some of the practical problems and limitations of MENT are also mentioned. In conclusion, the extension of tomography to multiple screens is briefly discussed, with results of a six-screen trial example from ALICE.

Chapter 8

Conclusion

8.1 General Summary

The technique of transverse phase-space tomography has been developed as a diagnostic tool on a section of the beam-line of the ALICE research accelerator at the Daresbury Laboratory of STFC. Requirements for screen image acquisition hardware, including cameras and associated optics, have been specified and quality tests defined; some improvements in user-selectable optical filtration have been implemented on the beam-line. A programme of tomography experiments has been planned and carried out, within the overall shift work schedule for ALICE, specifically to use the method for investigating the effects of space-charge. Experimentation has been supported by extensive particle tracking simulations. Results in terms of phase-space reconstructions and derived beam parameters have been analysed and conclusions drawn, giving recommendations for future work.

8.1.1 Detailed Summary by Chapter

The material covered in each chapter is summarised, and conclusions are drawn from the results obtained; references are made to the particular experimental (and simulated) datasets upon which findings are based, and which are illustrated in the chapters themselves.

1. The requirements for beam diagnostics in current particle accelerators are considered. The two machines ALICE and EMMA, based at the Daresbury Laboratory, are briefly described. The basic theory of transverse beam dynamics is covered, as background material to a brief account of some of the standard diagnostic methods used on ALICE and EMMA.
The general principles of computed tomography are outlined, with the two main classes of reconstruction algorithm, and the mathematical theory of the most popular algorithm 'Filtered Back Projection' (FBP) is also presented. Basic space-charge theory in particle beams, as applied to simple beam geometries, is developed to establish the

context for later work.

2. The theory underlying phase-space tomography measurement is described, relating real-space tomography mathematically to its counterpart in phase-space by a simple geometrical treatment. The plan for experimental tomography on ALICE is broken down into four phases for convenience. Each of these phases is described in terms of hardware improvements and adjustments; experimental procedures and protocols; input data preparation; specific settings of the beam-line; and the presentation of results in raw form. The first two phases are introduced:-
'Proof of Concept' (Phase 1) includes an analysis of requirements for an ideal tomography screen camera, and the optimisation of focussing carried out on installed cameras, as their early replacement by higher-specification types was not anticipated; the method of calculating current settings for quadrupole tomography scans; the stages in computer processing of results from screen images into reconstructed distributions, for example [Table B.1 Ref. 4, 47]; and the benefits of digital filtration after reconstruction to reduce noise, as applied to dataset [Table B.1 Ref. 5].
'Quantitative Measurements' (Phase 2) covers the procedure for camera recalibration; the implications of extending measurements from horizontal to vertical phase-space, illustrating that non-optimal vertical data gives inferior results [Table B.1 Ref. 4]; the significance of dispersion, with an ALICE measurement to show that it has an acceptable value; and experimental results from the initial studies with variable bunch-charge, in dataset [Table B.1 Ref. 7-10]. The possible implications of tomography for the future of the EMMA project are also discussed.

3. The linear beam dynamics theory underlying the analysis techniques used to derive Twiss parameters by calculation of 2^{nd} moments of phase-space is stated, with an example [Table B.1 Ref. 4] showing the effects of 'zoom' and 'filter' preprocessing on analysed reconstructions. The results of image data rebinning is demonstrated, and the fitting of an idealised 2-D Gaussian distribution, as applied to [Table B.1 Ref. 6], shows its effect on derived parameters. Two other useful correction methods for reducing noise, both pre- and post-reconstruction, are introduced: 'thresholding', illustrated on datasets [Table B.1 Ref. 20-24], and 'projection truncation' for background removal. An alternative and well-established analysis method, based on quadratic fitting to RMS beam-size from quadrupole-scanning, is outlined. Analysis is placed within the context of the overall tomography processing sequence. Comparisons are made between parameter values, principally horizontal emittance, from selected tomography experiments [Table B.1 Ref. 7-9] and those from earlier ALICE emittance measurements and simulations, showing good agreement under comparable beam conditions.

4. The physical principles underlying the particle tracking computer code GPT are described, and the various models available for applying space-charge effects in GPT are introduced, justifying the choice of a '3-D Point-to-Point' model in this work. Demonstrations of space-charge in the simplest beam-line geometry, a drift space, are illustrated [Table B.2 Ref. GPT01] by showing divergence in the beam. 'RMS bunch radius' is used to benchmark GPT [Table B.2 GPT02,03] against an analytical code based on established theory [Table B.2 Ana01,02], over a range of bunch dimensions and charges, both for Gaussian and for uniform section beams. The GPT user interface, and the input and output file structure, is presented. Initial results of modelling the ALICE tomography section in detail are plotted and deductions made, in terms of the 'fractional horizontal beam-size difference due to space-charge' metric [Table B.2 GPT05,06] which shows a distinctive peaked sign-change structure at the beam-size minimum. A convergence check is made for this metric, against number of particles modelled in the bunch, indicating ≥ 2000 particles to be suitable [Table B.2 GPT04].
A scheme for using the GPT model of the tomography section in an end-to-end simulation of the full phase-space tomography process is prepared, showing all data flows and functions. A method devised for generation of GPT input particle specification files is described, showing the processing steps and the text format of a GPT particle file. Giving results [Table B.2 GPT07] and explaining problems found, it is concluded that the assumption of simple Gaussian phase-space distributions and experimental values for input Twiss parameters is the best available approach. Various ways of validating the input specification against observed GPT outputs [Table B.2 GPT08] and against an independent analysis method [Table B.2 GPT09] are considered, and results compared for emittance and Twiss parameters, showing good agreement. This is supported by GPT-generated phase-space plots [Table B.2 GPT10].

5. 'Detailed Space-Charge Experiments' (Phase 3) begins with a consideration of the problem of camera CCD saturation in beam images at high bunch-charge, and its solution using optical filtration. Experiments specifically designed to detect space-charge induced effects in tomographic reconstructions by measurements at separated points in the beam-line are described, with their associated input data preparation. Both the raw reconstructed output, and the corresponding Gaussian-fitted phase-space distributions, when shown in tabular form, illustrate a clear gradation in size and shape with increasing charge [Table B.1 Ref. 17-26]. Plots of horizontal emittance against bunch-charge, derived from the two sets of quadrupole tomography scanning results for QUAD-07 and QUAD-11, have very obvious upward trends, converging at higher charge and showing no definite evidence of a positive space-charge effect, up to 80 pC. Twiss parameter α, β plots also indicate similar trends but these are rather less consistent.
In 'Further Space-Charge Studies' (Phase 4), the experiments are extended to include

vertical phase-space, and camera imaging is further improved by deploying remote-control filter-changers. The maximum bunch-charge range available is from 5 pC to 52.6 pC. Again, reconstructions are compared side-by-side: QUAD-07 and QUAD-10 data in the horizontal show good agreement in shape though not in size, from datasets [Table B.1 Ref. 32-36, 37-41]. Emittance shows a rising trend with charge for both quadrupoles, although there is a × 2 difference except at low charge.
In contrast, the QUAD-06 and QUAD-11 datasets [Table B.1 Ref. 27-31, 42-46] in the vertical are distinctly different both in shape and in orientation, and the emittances, though both on an upward trend, differ by up to × 10. The equivalent simulated data from GPT [Table B.2 GPT11-12] confirm this QUAD-06/QUAD-11 difference. Considering possible sources for the discrepancy, lattice errors could be discounted; a study using MENT as the reconstruction method in comparison with FBP on datasets [Table B.1 Ref. 30, 45] does not provide an explanation. However, there is evidence [from simulations by K Hock] that the resolution of projections, directly related to camera image pixel size, can affect reconstructions in the way observed, if it is too low. Experimental confirmation, although not possible within this body of work, would be an interesting topic for further study, using more advanced camera systems.

6. The 'normalised phase-space' transformation is defined, and its relationship with the design of the EMMA Injection Line tomography section, in terms of phase-advance, is explained. Methods for estimating the Twiss parameters α and β, as required for normalisation, are suggested. Two example results from experiment are given, comparing real with normalised phase-space distributions: one is an ideal case showing the additional detail obtainable, and a second from [Table B.1 Ref. 4,5] which fails to show appreciable advantages in the result because of inappropriate selections of α and β for normalisation.

7. The reconstruction of tomographic data using the Maximum Entropy (MENT) algorithm is described, with an outline of the main principles of its mathematical theory. It is demonstrated in examples of 3-screen experimental data [Table B.1 Ref. 2] that MENT has clear advantages over the FBP algorithm in its relative freedom from reconstruction artifacts, when just a few projections are available. However, it is further shown by simulation that significant distortion in reconstructions can occur, and that care must be taken in the choice of projection angles, if the validity of MENT results is to be ensured. It is concluded that in this respect, working in *normalised* phase-space is an effective solution.
An example of multiple-screen tomography with FBP is compared, using data from [Table B.1 Ref. 2,3], but shows no advantage over the standard 3-screens method in this limited case.

Appendix A. In the first part of the Appendix, a standard method for evaluating screen imaging cameras, using an ISO test card and analysis software, is proposed. Desireable attributes for an advanced high-specification camera are listed. The procedure for optimising the focus setting of existing ALICE screen cameras is described, and a calculation is presented for the theoretical depth of field. Results (without beam) of an experimental check of camera focus at a screen are also shown, before and after focus setting.

Appendix B. The experimental and simulated datasets referenced in this document are listed with their most important attributes, allocating each a unique ID.

Appendix C. The detailed steps of the computer processing system developed for phase-space tomography data are described, showing example graphics output at key stages in the sequence.

Appendix D. Finally, a study of the MENT code (originating at Los Alamos) referenced in Chapter 7 is described, giving an example of its adaptation for use with a particular set of experimental ALICE three-screen data [Table B.1 Ref. 26a]. Although demonstrated to work successfully, due to its inflexibility it is considered unsuitable for further development of ALICE beam tomography.

8.2 Overall Conclusions

The success on ALICE of the quadrupole tomography scanning technique, with reconstruction of phase-space using the FBP algorithm, strongly recommends it as having the potential for producing good-quality results from beam tomography on general beamlines, although the reconstruction anomalies of the type discussed in Section 5.3.1 will need to be resolved. Where sufficient imaging diagnostics, such as YAG screens, are already provided, it will normally be possible to identify a suitable quadrupole-screen combination, related to the desired reconstruction reference position, to give an adequate projection-angle range (close to 180^o) for quality results free from excessive artifacts. At the same time, the evidence of the anomalous results observed in vertical phase-space indicates that care should always be taken to check reconstructions, wherever possible, against alternative measurements, however well-defined and conclusive they appear to be.

Phase-space tomography has demonstrated its potential in the study of perturbing effects, using space-charge as an example which is relevant for low-energy, high bunch-charge regimes. It has also been shown that using particle-tracking codes to simulate the process of generating phase-space distributions by tomography can be a useful aid for investigating these effects, and potentially for understanding them better.

8.3 Further Work

Under this heading are

- objectives not achieved or only partially met, due to time or resource constraints, but which are still considered feasible and desirable;
- possible extensions to other situations, applications or locations;
- new ideas, generated during the project itself, but which there was insufficient time to investigate further.

Application to Other Facilities It is at present uncertain that any further ALICE operations will continue beyond December 2012. However, concepts already trialled on ALICE, including 'normalised phase-space', may find applications at other research accelerator facilities, for example PITZ at DESY [12]. PITZ in particular has a dedicated tomography section with up to 4 beam imaging screens available, supported by advanced cameras and optics as illustrated in Fig. 8.1, and there is significant experience within the PITZ group in applying the various tomography techniques.

Figure 8.1: In the tomography section of the PITZ beam-line, advanced CCD cameras, well shielded from stray radiation, are used with high-quality remotely-adjustable optics to provide optimum screen images.

Processing of ALICE Data It would be useful to process more of the data, including '3-screen' image sets, which has already been taken but not yet examined in detail due to other priorities. Other data which has been processed once may benefit from a revisit, using more advanced tools and methods, such as background suppression or the systematic application of the MENT algorithm.

New Local Facilities The Versatile Electron Linear Accelerator (VELA), formerly known as the Electron Beam Test Facility (EBTF), is entering its commissioning phase at the Daresbury Laboratory [51]. It will be important to characterise the beam in this machine as fully as possible; beam tomography will be a very useful tool to help achieve this. Key VELA parameters will be:

Energy range $\leq 5\,\text{MeV}$;
Normalised horizontal emittance = 1 to 4 mm-mrad;
Bunch-charge = 10 to 250 pC

A continuation of the study of space-charge effects using tomography, both by simulation and by experiment, would be very relevant, as under the VELA regime much more significant effects might be expected than on ALICE, with lower beam energy and far higher maximum bunch charge.

Extensions to EMMA The future of the EMMA project is still undecided, due partly to its dependence on ALICE for injection. However, if work continues, beam tomography in the extraction line, which as stated in Section 2.5 is already suitably equipped, would provide further useful data on the effects of acceleration in FFAGs.

Advances in Equipment Improvements in hardware which would lead to better-quality results from tomographic reconstructions and which are considered in Section 2.3.1 and Appendix A should be installed, including high-specification screen imaging cameras and associated networking and control systems.

Multi-Dimensional Phase-Space Tomography Tomography in four dimensional (4-D) phase-space (x, x', y, y') is a logical extension of the technique in 2-D, i.e. (x, x') or (y, y'), which has been described in this work. The supporting 4-D theory has already been developed and tested in simulation [47]; it is based on multiple scans using a pair of quadrupole magnets, one defocussing and the other focussing, and a single screen. It is planned to run 4-D tomography experiments on the new VELA facility within the next 3 years.

Appendix A

Camera Performance and Specifications

A.1 Camera Specification for Improved Performance

An advanced camera system (not specifically for the scientific market) has been evaluated in demonstration against suitability criteria for screen imaging [52].

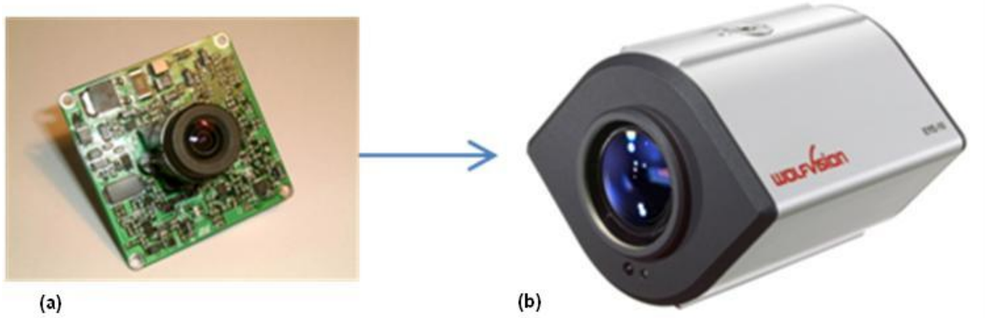

Figure A.1: (a) A CCD ‘board’ camera with fixed lens, of the type currently used throughout ALICE. (b) An example of a high-specification camera with remote control, evaluated as an option for specialised applications on ALICE.

Optics Built-in zoom allows focus and image magnification adjustment to optimise use of available pixels to image the beam, and iris control gives exposure variation as well as some adjustment of depth of field. The option of a ‘periscope’ mount viewing the screen at 90^o, to keep the camera well away from the beam-line axis and reduce the risk of CCD damage from radiation, can be investigated.

Communications A standard and reliable Ethernet link facilitates networking without requiring further dedicated cabling.

Resolution The region of interest around the beam itself is covered by more pixels. A 12-bit depth per pixel improves the signal to noise ratio and therefore the final quality of reconstructions.

Software Control Exposure which is remotely controllable allows the maximum dynamic range to be used while avoiding the saturation of pixels.

Maintainability ALICE experience shows that in some locations, over months of service there is a visible degradation of image quality, due to permanent radiation damage to CCD pixels. Although suitable shielding can reduce this, the ability to replace affected CCD chips quickly and economically is useful in extending system lifetimes.

Conclusion A single camera should be procured and a mounting fabricated for viewport deployment by directly replacing an existing board camera. The most appropriate initial location is proposed as screen EMI-YAG-03.

A.2 Focus Setting Procedure

Coarse Focus The brass fine-focussing ring is first set to the middle of its travel (noting its approximate original position). The camera, mounted on its base-plate, is then removed from the housing, after first taking off the rear cover with its 4 retaining screws. The lens assembly is mounted on a threaded fitting, permitting adjustment of the lens-to-CCD distance (‘v’ in Fig. A.2). With the camera pointed towards a test object at approximately the correct distance as when assembled, a good focus is set by slight rotation of the lens holder. Care should be taken not to disturb the filter over the lens (if fitted).

Fine Focus Adjustment uses the central knurled ring at the rear of the camera housing, which alters the camera distance to the screen (‘u’ in Fig A.2). It has been found that fine adjustment has little effect on focus; this is confirmed by theory, which predicts that the depth-of-field will include the whole screen (edge to edge) in spite of its being viewed at a 45^o angle.

Typical results of refocussing are illustrated in Fig. A.3.

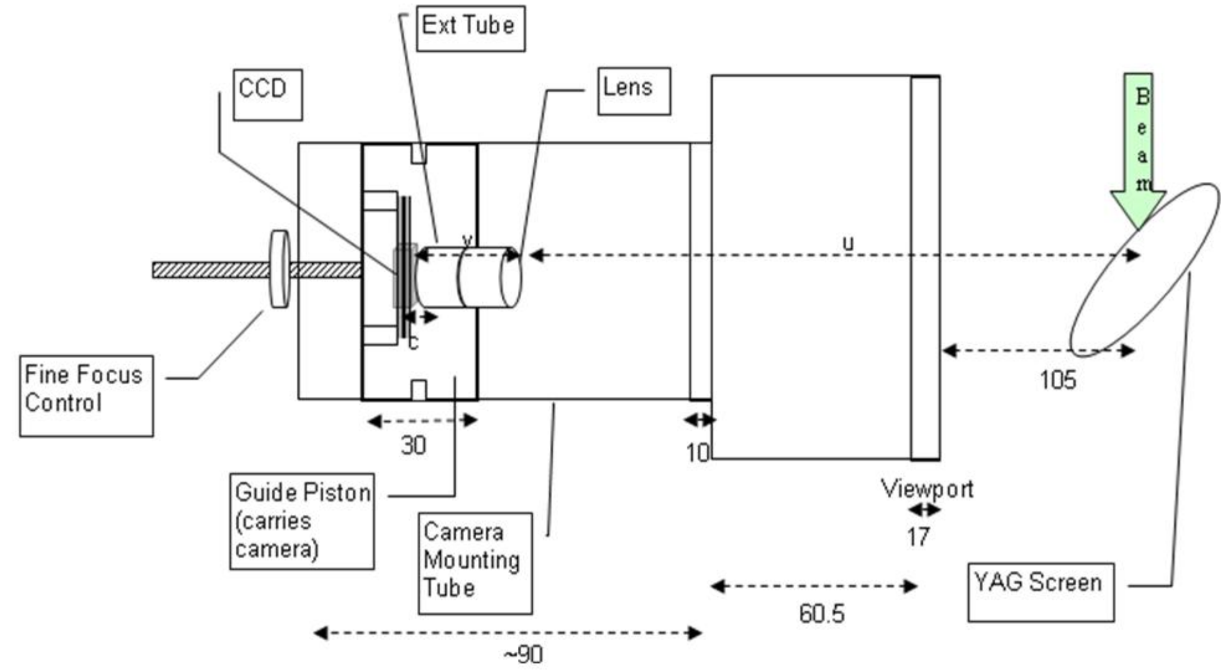

Figure A.2: The dimensioned schematic (units = mm) shows the mounting arrangement for current ALICE screen cameras, including controls provided for focussing adjustment. The whole assembly is bolted onto the imaging viewport for the screen.

Table A.1 calculates Depth-of-Field (D_{Far} - D_{Near}) for typical dimensions of the screen camera shown above. YAG screens are circular (60 mm diam) but are inclined at 45^o to the camera and the beam.

Depth of Field: Calculation

$$\begin{aligned} FocalLength &= 16\,\text{mm} \\ D_{Near} &= sf^2/(f^2 + Nc(s-f)) \\ D_{Far} &= sf^2/(f^2 - Nc(s-f)) \end{aligned} \tag{A.1}$$

Object distance s	Stop diam d	f-num N	Circle of Confusion c	D_{Near}	D_{Far}	Depth of field	Screen width at 45^o
186.7	3	5.33	0.02	174.30	201.0	26.69	42.43

Table A.1: Equations A.1 are used to calculate near and far points D_{Near} & D_{Far}, and hence depth-of-field, for comparison with effective screen width. f-number N is derived from focal length f and aperture d by $N = f/d$ (all units in mm).

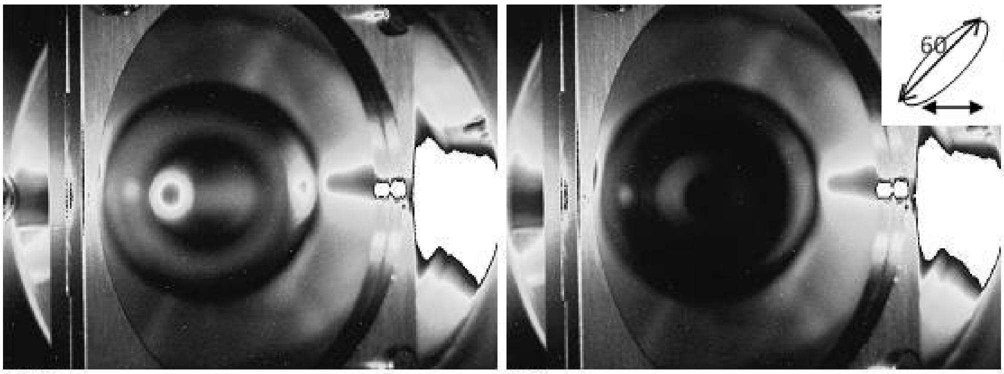

Before

After

Figure A.3: Camera images taken of YAG screen 'EMI-3', using LEDs for illumination, show the results of the focus setting procedure, before adjustment (L) and afterwards (R). The inset (Top R) shows the screen diameter (in mm.) with its 45^o orientation.

Appendix B

List of Datasets Used

B.1 Experimental Data

Data has been taken during experimental shifts which have been spread over much of the duration of the project. Individual datasets are identified uniquely by the date of the shift and the time-stamp of the image or image-sequence collected, where the time is automatically attached to all data file names by the acquisition software. Within the main chapters, a particular dataset is referenced by the combination of Date and Time, in the format 'DDMMYY TTTT'. The most important parameters and machine settings are also recorded here for convenience.

B.2 Simulated Data

Simulations involving particle tracking have been run between experimental campaigns and to fit the time around scheduled shifts. In the same way as the experiments, datasets are given references by Date and Time.

Ref	Date ddmmyy	Time hhmm	Type	Quad	Screen (YAG)	Charge (pC)	Energy (MeV)	Notes
1	030810	1855	3-Screen			40	15.51	
2	150810	1911	3-Screen			40	15.51	
3	210810	1329	6-Screen			12	15.51	
4	150910	0103	Scan	Q-08	03	40	12.51	
5	150910	0130	Scan	Q-08	03	40	12.51	Normalised
6	211010	0217	Scan	Q-08	03	40	12.51	
7	160211	0620	Scan	Q-08	03	40	12.51	
8	270211	0646	Scan	Q-08	03	40	12.51	
9	090311	0342	Scan	Q-08	03	40	12.51	
10	090311	0413	Scan	Q-08	03	50	12.51	
11	090311	0508	Scan	Q-08	03	60	12.51	
12	090311	0541	Scan	Q-08	03	70	12.51	
13	090311	0354	Scan	Q-09	03	40	12.51	
14	090311	0425	Scan	Q-09	03	50	12.51	
15	090311	0519	Scan	Q-09	03	60	12.51	
16	090311	0552	Scan	Q-09	03	70	12.51	
17	190411	0202	Scan	Q-07	02	20	12.51	
18	190411	0233	Scan	Q-07	02	40	12.51	
19	190411	0255	Scan	Q-07	02	60	12.51	
20	190411	0359	Scan	Q-07	02	70	12.51	
21	190411	0324	Scan	Q-07	02	80	12.51	
22	190411	0216	Scan	Q-10	04	20	12.51	
23	190411	0244	Scan	Q-10	04	40	12.51	
24	190411	0307	Scan	Q-10	04	60	12.51	
25	190411	0410	Scan	Q-10	04	70	12.51	
26	190411	0347	Scan	Q-10	04	80	12.51	
26a	190411	0046	3-Screen			40	12.51	
27	060812	2022	Scan	Q-06	02	5	12.51	
28	060812	2123	Scan	Q-06	02	10	12.51	
29	060812	2209	Scan	Q-06	02	20	12.51	
30	060812	2258	Scan	Q-06	02	40	12.51	
31	060812	1836	Scan	Q-06	02	52.6	12.51	
32	060812	2042	Scan	Q-07	02	5	12.51	
33	060812	2133	Scan	Q-07	02	10	12.51	
34	060812	2220	Scan	Q-07	02	20	12.51	
35	060812	2311	Scan	Q-07	02	40	12.51	
36	060812	1900	Scan	Q-07	02	52.6	12.51	3.2% filter
37	060812	2056	Scan	Q-10	04	5	12.51	
38	060812	2144	Scan	Q-10	04	10	12.51	
39	060812	2232	Scan	Q-10	04	20	12.51	
40	060812	2322	Scan	Q-10	04	40	12.51	
41	060812	1915	Scan	Q-10	04	52.6	12.51	
42	060812	2106	Scan	Q-11	04	5	12.51	
43	060812	2157	Scan	Q-11	04	10	12.51	
44	060812	2245	Scan	Q-11	04	20	12.51	
45	060812	2334	Scan	Q-11	04	40	12.51	
46	060812	1955	Scan	Q-11	04	52.6	12.51	3.2% filter
47	151112	1429	Scan	Q-07	02	69.0	12.51	

Table B.1: Experimental data referenced in the text is listed by date. ‘Ref’ is a unique identifier; the ‘Time’ stamp denotes the start of a scan; ‘Type’ refers to either a *multi-screen tomography* or a *quadrupole tomography scan* measurement; ‘Quad’ (for scans) is the quadrupole ID; ‘Screen’ (for scans) is the ID of the YAG screen for imaging; ‘Charge’ is that measured for one bunch; ‘Energy’ is the *Total* particle energy, including rest-mass.

Ref	Date ddmmyy	Input Model	Quads	Screens (YAG)	Charge (pC)	Energy (MeV)	Bunch Params (mm)	nps	Notes
GPT01		Drift		at 1.5m	0,80,200	12	Gaussian	1000	Divergence demo
GPT02	170712	Drift		at 0.015-1.50m	5,20,80	12.511	Gaussian r=0.3,0.6,1.2 l=0.5,1.0,2.0	10k	GPT: Benchmarking vs. Analytical code
GPT03	170712	Drift		(as above)	5,20,80	12.511	Uniform (with r,l as above)	10k	(as above)
Ana01	200412	Drift			5,20,80	12.511	Gaussian r=0.3,0.6,1.2 l=0.5,1.0,2.0		Analytical code: Benchmarking vs. GPT
Ana02	200412	Drift			5,20,80	12.511	Uniform (with r,l as above)		(as above)
GPT04	051211	EMI	Q-07 to Q-11	02, 04	0,80	12		100-10k	Check for convergence with NPS
GPT05	231111	EMI	Q-07	02	0,80	12		1000	Space-Charge Beam-Size Difference, YAG-02
GPT06	251111	EMI	Q-10	04	0,80	12		1000	Space-Charge Beam-Size Difference, YAG-04
GPT07	110712	EMI	Q-07 to Q-11	02, 04	0	12	Gaussian (x, x'), (y, y') read from file	10k	Generation of Input Particle Specifications
GPT08	161012	EMI	Q-07	02	0	12.511	$\beta, \alpha, \epsilon = \mathit{exptl}$; l=1.2	10k	GPT Input vs Output validation
GPT09	091012	EMI	Q-06	02	0	12.511	$\beta, \alpha = \mathit{exptl}$; $\epsilon = \mathit{exptl} \times 10$	10k	GPT and 'Quad-Scan Analysis' comparison
GPT10	111212	EMI	Q-06..11	at Q-07	0	12.511	$\beta, \alpha, \epsilon = \mathit{exptl}$	10k	GPT Phase-Space plots
GPT11	241012	EMI	Q-06 & Q-07	02	0,5,10, 20,40,52.6	12.511	$\beta, \alpha, \epsilon = \mathit{exptl}$	10k	GPT Tomography Scans to compare with Experiment
GPT12	011112	EMI	Q-10,11	04	0,5,52.6	12.511	$\beta, \alpha, \epsilon = \mathit{exptl}$	10k	(as above)

Table B.2: Simulated data which appears in the text is listed by order of appearance. 'Ref' identifies the run sequentially as a GPT model (GPT*nn*) or Analytical code (Ana*nn*); 'Input Model' is typically a simple *Drift*, or *EMI* for EMMA Injection Line; 'Quad' is the ID of quadrupole(s) modelled; 'Screen' is the ID (or position in m. from the start) of the imaging YAG screen; 'Charge' is for one bunch; 'Energy' is *Total* particle energy; 'Bunch Params' denotes *distribution* and ***r**adii/**l**engths*; 'nps' is the *number of particles* simulated (1k=1000).

Appendix C

Phase-Space Tomography Computer Processing

C.1 Sequence of Steps in Processing Raw Images into Reconstructed Phase-Space

In general, it is assumed in this code that the input data, particularly the transfer matrices, have been correctly formatted and that all other essential files are available in the locations specified in the parameters files. However, a degree of error-trapping is provided for foreseeable cases of missing or invalid files.

The sequence followed is [with functions marked '*' dependent on preset parameters (selected as control file variables)]:-

1. Determine whether data relates to horizontal (H) or vertical (V) phase-space.
2. Read in transfer matrices.
   This is the array of matrices $[M_1 ... M_{\mathrm{nproj}}]$ where the M_{i} are defined as in Eq. 2.1 and nproj is the number of projections.
3. Calculate angles θ and scale factors s from the matrices M.
   Eq. 2.4 and Eq. 2.6 are applied, respectively, for θ and s.
4. Get and process image data, and create a sinogram, by following these steps:-
   - Load options from file.
     User options may be predefined before run-time, in a parameters file. These control some processing options, and supply the directories where image and other files are to be found.
   - Select and read in images.
     User chooses files from list OR all files in directory (from a scan) are read automatically. Display screen images (as a check) only if there are less than 6 files, as in Fig. C.1.

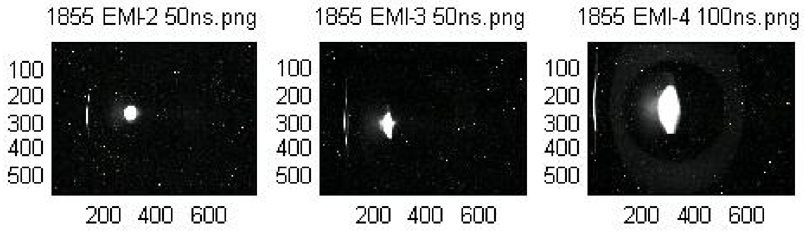

Figure C.1: This example shows images of an 3-screen tomography dataset as they are displayed after being loaded from files. Headings are the actual filenames and the axes scales are in pixels.

- Parse image filenames to determine screen IDs/train lengths.

  Extract the screen identifier and the electron bunch train-length, encoded in the image filename (e.g. ‘1836 EMI-2 30ns EMI-QUAD-06=0.044.png’) by the camera software when the image is created.

- Get screen backgrounds from storage.

  The most recent background images (for each separate screen used; there may be only one) are read from a standard location; see Fig. 2.11.

- Subtract backgrounds from images.

  Available options are: (a) subtract pixel-by-pixel; (b) subtract a single level (average of whole background image); (c) subtract a user-defined single level, which allows user estimation by viewing a profile, or otherwise.

- *Correct for baseline level in images.

  As the beam is nearly always just a small peak in a flat continuum in the screen image, a very approximate baseline correction may be optionally applied by subtracting the average of each image from that same image.

- Normalise images for different train-lengths, if necessary.

  Image intensity depends on the number of bunches per train; if this is changed during the experiment, the effect is compensated for using the train-lengths read previously.

- Check overall intensities, by plotting for all images.

  Display integrated image intensity values $\sum_x \sum_y i_{xy}$ on the same plot for comparison; ideally intensity is uniform.

- Read in screen calibration data.

  Screen ID is used to find matching data in an EXCEL calibration file and retrieve calibration factors (in mm per pixel)

- Apply calibration; interpolate (onto new grid).

  Image pixels are converted to positions (in mm.)

- Display overlaid images (with H, V projections), and select window.

  User interactively sets a window around the beam, to reject extraneous features, as illustrated in Fig. C.2. Possible choices are: (a) use selected window; (b) use full screen area; or (c) use keyboard-entered window extents (useful for replicating a previous run).

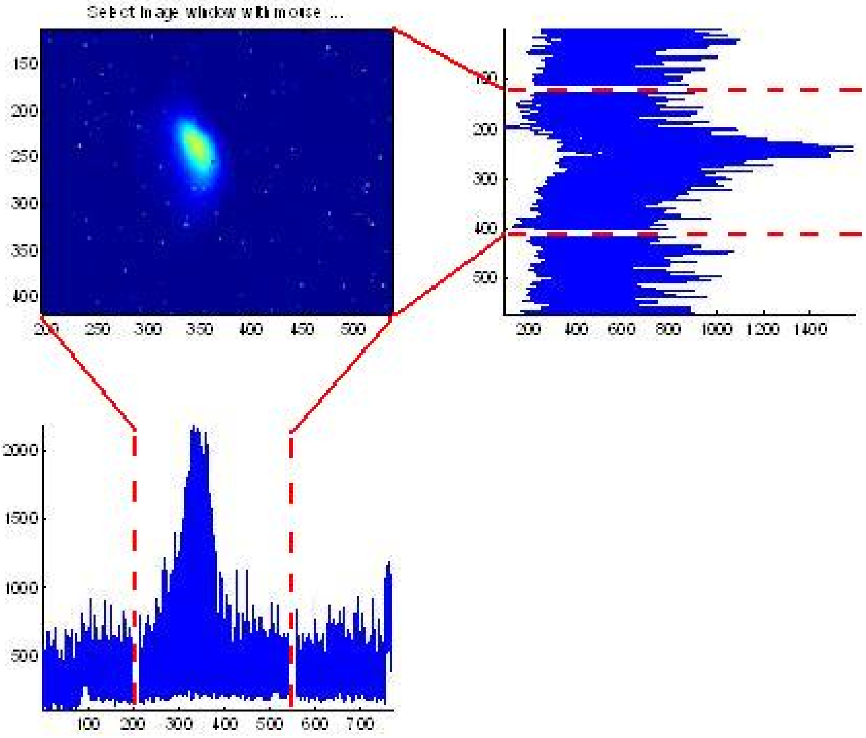

Figure C.2: The full beam image set is displayed, superimposed as a single overlay, with the composite horizontal and vertical projections shown underneath and to the R. The user can interactively select a rectangular window around the beam, guided by the peak extents; the image display zooms in to this selection.

- Select reduced image set

  User may reject any particularly high (or low) intensity images at start/end of the sequence which would add to reconstruction noise. An example of choosing an upper value is shown in Fig. C.3.

- Renormalise new image set.

  Image intensities are adjusted to normalise them to the maximum image.

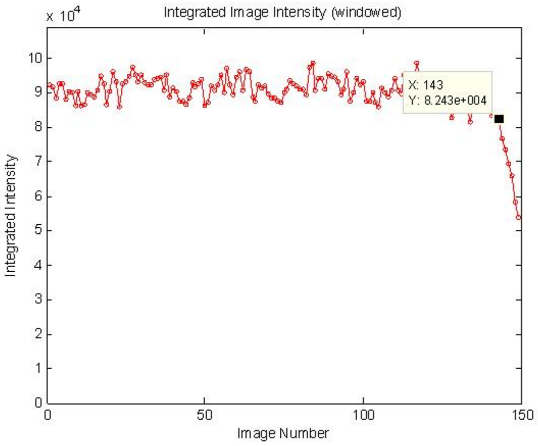

Figure C.3: Integrated intensities are plotted for all images in the set, as a guide for the user to select upper and lower bounds. If chosen, because they appear significantly below the average value, images outside the bounds will be rejected.

- Project (onto x or y axis) to create a sinogram.

  The sinogram is assembled as an array of projections.

- *Calculate baseline correction around peaks in projections.

  User may select to apply correction by: (i) fitting Gaussian to the peak to find its extent; then (ii) calculating a 'base level' from regions to each side of the peak; and (iii) subtracting baseline; repeated for each projection.

- Scale projections.

  Apply scale factors s to all projections in the sinogram.

- Find centre (*centroid, or peak value) for each projection.

  Normally the centroid is the appropriate measure of the 'centre'. A sample of the projections is plotted, as in Fig. C.4, for comparison and to confirm corrected baseline level.

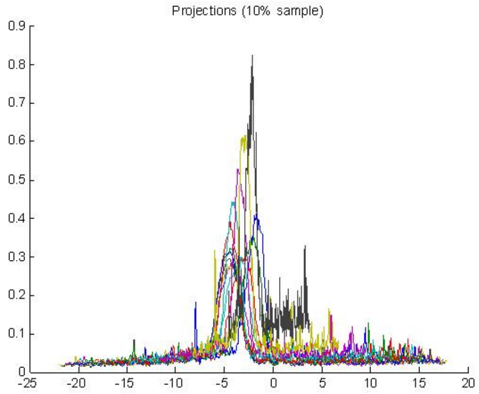

Figure C.4: A sample of 10% of all projections is displayed, superimposed and in distinguishing colours. The user can confirm that the baseline is now at least approximately zero, and that only the main 'beam' peak is present.

- *Calculate weightings for projections, for irregular angle intervals.

  Angle weighting is applied only exceptionally; normally, intervals will be regularly-spaced, as the reconstruction algorithm requires.
- Re-sort projections in sinogram by angle order, if necessary.

  Usually the 'angle' array is already in monotonically increasing order; if not, it is re-sorted.
- Display sinogram and save, along with positions and other projection data.

  A sample plot is shown in Fig. C.5, where the x-axis represents 'position' and the y-axis is 'angle'.

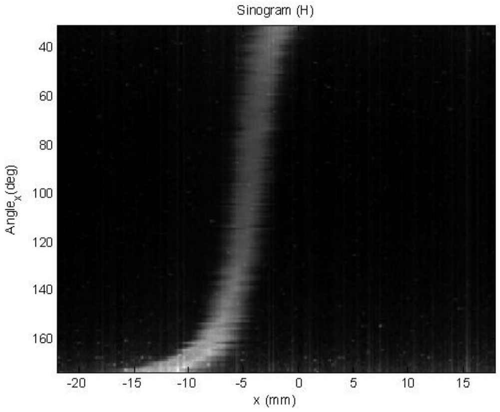

Figure C.5: The sinogram, built from the assembled and ordered projections, is displayed with *position* (in mm.) on the x-axis and *projection angle* (in degrees) on the y-axis.

5. Reconstruct from sinogram; display result as a contour plot, e.g. Fig. C.6.

   After viewing the initial reconstruction, a user may enter new phase-space limits and repeat the reconstruction step (or exit). There is an option to save, both as image files and a MATLAB array datafile.

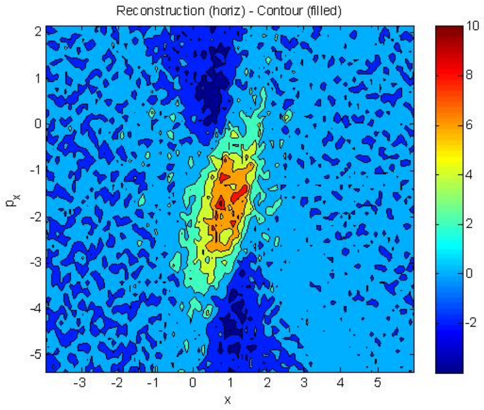

Figure C.6: The result of reconstruction of phase-space with FBP is displayed in contour plot form, for user acceptance. Axis units are mm (x horizontal) and mrad (x' vertical). The user may then repeat the reconstruction having optionally selected new, reduced phase-space limits.

Appendix D

An Implementation of the MENT Tomographic Reconstruction Code

A FORTRAN code implementing MENT which was originally developed at Los Alamos, USA, in 1979 has been adopted at the Paul Scherrer Institute (PSI) and is still in use [15]. This code has been installed and successfully tested at the Daresbury Laboratory, although new interfaces have been necessary to handle the details of suitably converting the ALICE tomography camera image data for input to MENT(PSI).

D.1 Data Preparation and Execution Environment

The Maximum Entropy Tomography (MENT) code produced at PSI requires a very specific input file format. Code has therefore been developed to pre-process the tomographic projections together with their corresponding control parameters and transfer matrices, as shown in Figure D.1. In addition, the user graphics runs in an X-Windows environment, and output is generated as Postscript files which would require conversion before further analysis by other programs.

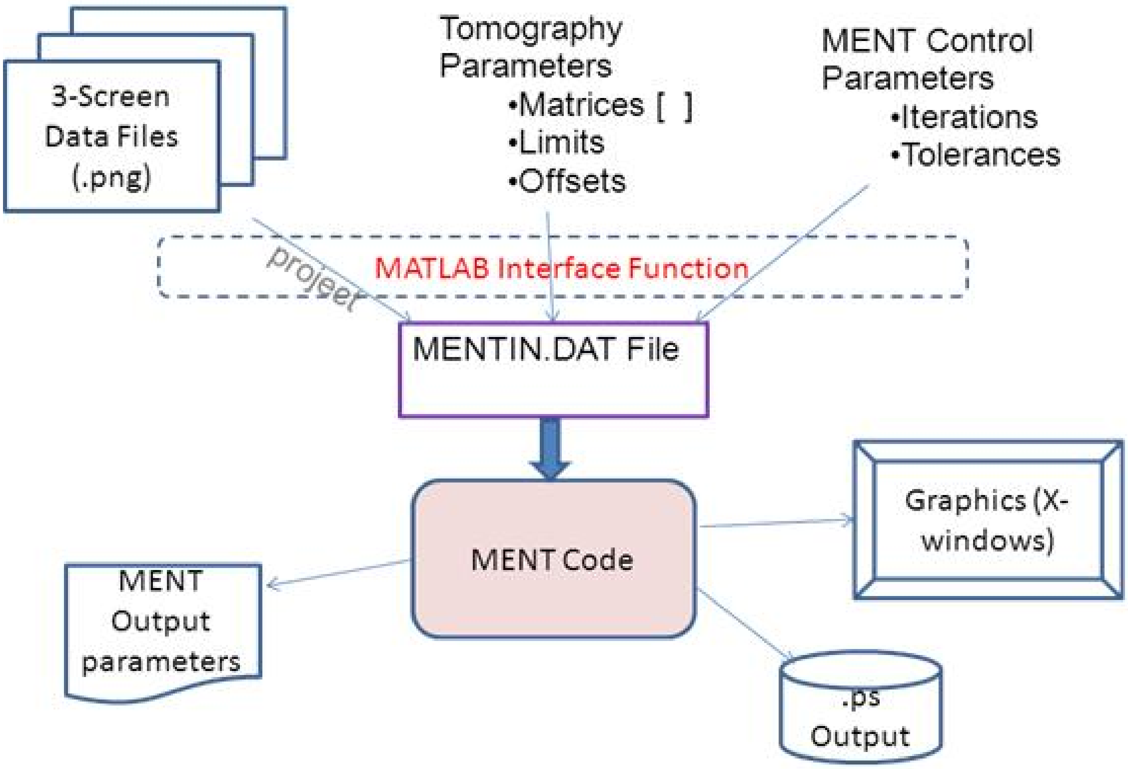

Figure D.1: The MENT implementation by PSI has very specific input and output format requirements for its MENTIN.DAT file. MATLAB interface functions have been written to convert ALICE tomography data to suit.

Although the code is mature and therefore efficient and reliable, it is also rather inflexible, which created problems with interfacing to ALICE experimental data, and with modifying parameters to more appropriate values for ALICE, e.g. to make use of the full image resolution available.

D.2 Applying the MENT Code

Data Conversion to MENT(PSI) Format For the conversion of existing ALICE tomography data to the fixed format of the 'MENTIN.DAT' input file, as shown in Fig. D.2, MATLAB code has been written to:

- perform background subtraction;
- correct for any differences in calibration between the 3 screens;
- interpolate to reduce the projection positions down to the limited number accepted (= 51), far fewer than the pixels available in an image;
- allow windowing, to select the essential central beam data only.

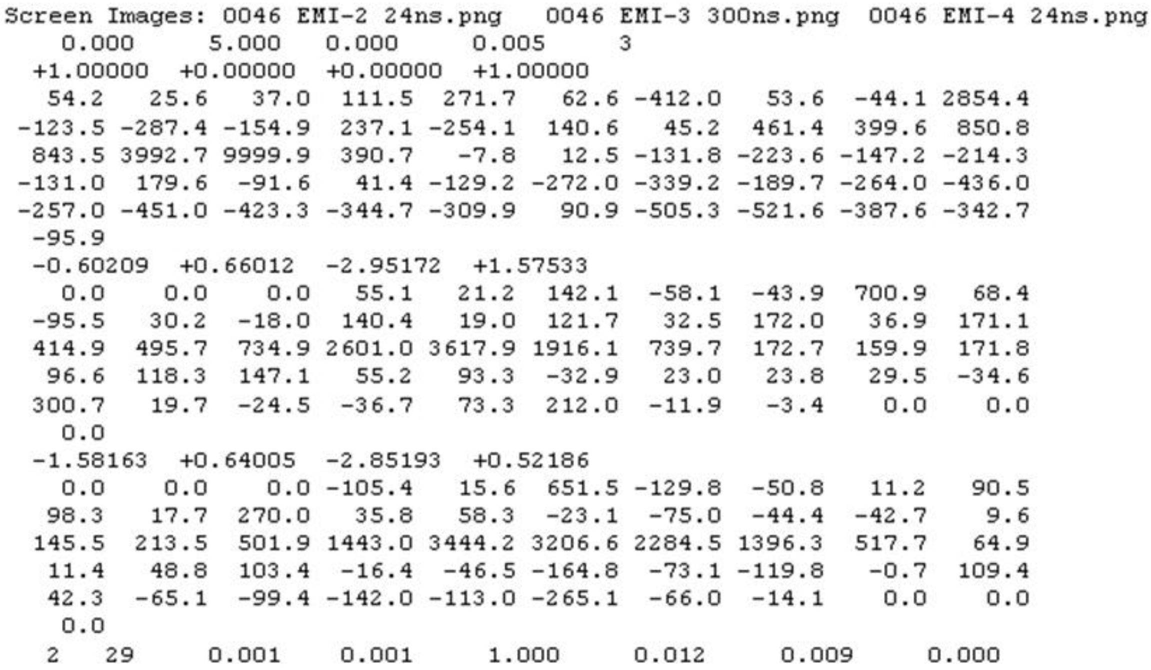

```
Screen Images: 0046 EMI-2 24ns.png   0046 EMI-3 300ns.png  0046 EMI-4 24ns.png
   0.000      5.000   0.000      0.005     3
  +1.00000  +0.00000  +0.00000  +1.00000
   54.2    25.6    37.0   111.5   271.7    62.6 -412.0    53.6   -44.1 2854.4
 -123.5 -287.4 -154.9   237.1 -254.1   140.6    45.2   461.4   399.6  850.8
  843.5 3992.7 9999.9   390.7    -7.8    12.5 -131.8 -223.6 -147.2 -214.3
 -131.0  179.6  -91.6    41.4 -129.2 -272.0 -339.2 -189.7 -264.0 -436.0
 -257.0 -451.0 -423.3 -344.7 -309.9    90.9 -505.3 -521.6 -387.6 -342.7
  -95.9
  -0.60209  +0.66012  -2.95172  +1.57533
    0.0     0.0     0.0    55.1    21.2   142.1   -58.1   -43.9   700.9   68.4
  -95.5    30.2   -18.0   140.4    19.0   121.7    32.5   172.0    36.9  171.1
  414.9   495.7   734.9 2601.0 3617.9 1916.1   739.7   172.7   159.9  171.8
   96.6   118.3   147.1    55.2    93.3   -32.9    23.0    23.8    29.5  -34.6
  300.7    19.7   -24.5   -36.7    73.3   212.0   -11.9    -3.4     0.0    0.0
    0.0
  -1.58163  +0.64005  -2.85193  +0.52186
    0.0     0.0     0.0 -105.4    15.6   651.5 -129.8   -50.8    11.2   90.5
   98.3    17.7   270.0    35.8    58.3   -23.1   -75.0   -44.4   -42.7    9.6
  145.5   213.5   501.9 1443.0 3444.2 3206.6 2284.5 1396.3   517.7   64.9
   11.4    48.8   103.4   -16.4   -46.5 -164.8   -73.1 -119.8    -0.7  109.4
   42.3   -65.1   -99.4 -142.0 -113.0 -265.1   -66.0   -14.1     0.0    0.0
    0.0
   2   29      0.001     0.001      1.000      0.012      0.009      0.000
```

Figure D.2: An example of a MENTIN.DAT input file is shown, with 51-position projection data from 3 screen images (background-subtracted). Other fields contain projection angles and MENT control parameters.

The MENT Output Window provides alternative display options to show:

- fitted and experimental projections (as overlays)
- phase-space distribution (as a 2-D contour plot)
- emittance probability (on lin-log axes)
- 3-D plot of phase-space (corresponding to the contour plot)

This example in Fig. D.3 shows real ALICE data, where the parameters have been optimised for fit of experimental to calculated projections. In the emittance plot of the function $\log(1-f)$ `versus` ϵ_x, where $f =$ fraction of beam inside emittance ϵ_x, beams with Gaussian profile shapes produce straight lines. Deviations from Gaussian can therefore be seen very easily. In this instance, the approximate straight line indicates that the phase-space distribution is close to Gaussian.

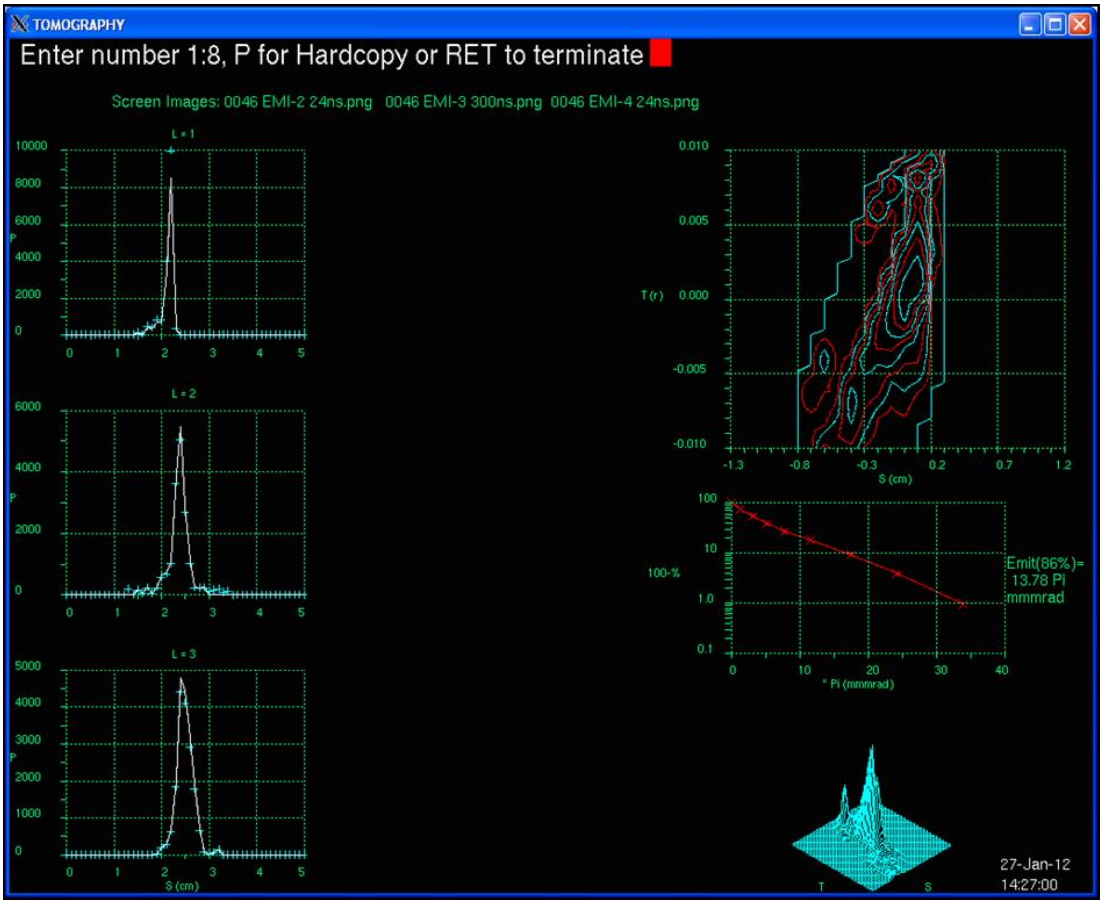

```
Enter number 1:8, P for Hardcopy or RET to terminate
Screen Images: 0046 EMI-2 24ns.png  0046 EMI-3 300ns.png  0046 EMI-4 24ns.png
Emit(86%)=
 13.78 Pi
mmmrad
27-Jan-12
14:27:00
```

Figure D.3: The MENT output window combines plots of the experimental-input and MENT-fitted projections (overlaid); a 2-D contour plot of reconstructed phase-space; an emittance-probability plot (lin-log); a 3-D phase-space plot of the reconstruction.

Although the processing of 3-screen data by MENT was successfully demonstrated, using an ALICE input dataset, it was concluded that significantly improved results would only be obtained when the planned camera modifications had been made, giving better image quality. In addition, modifications to the core MENT code would be necessary to make the output more accessible for further analysis.

Bibliography

[1] M G Ibison and K M Hock. ALICE Tomography Section: Measurements and Analysis. *Journal of Instrumentation*, 7:P04016, 2012.

[2] R T P D'Arcy, D J Holder, B D Muratori, and J Jones. MODELLING OF THE EMMA NS-FFAG INJECTION LINE USING GPT. In *IPAC 10*, number MOPEC046, University College London, UK, 2010. Held in Kyoto, Japan.

[3] Victor Smaluk. *Particle beam diagnostics for accelerators*. VDM Verlag Dr. Muller, 2009.

[4] Ben Shepherd. *File:EMMA schematic INJ EXT v02.jpg*. Daresbury Laboratory, 2.0 edition, March 2010. `http://projects.astec.ac.uk/EMMAManual/index.php/File:EMMA_schematic_INJ_EXT_v02.jpg#file`.

[5] S Machida et al. Acceleration in the linear non-scaling fixed-field alternating-gradient accelerator EMMA. *Nature Physics*, 8:243–247, 2012.

[6] S L Smith. EMMA, The World's First Non-Scaling FFAG Accelerator. In *PAC09*, STFC, Daresbury Laboratory, Warrington, UK, 2009. Held at Vancouver, BC, Canada.

[7] D J Holder and B D Muratori. MODELLING THE ALICE ELECTRON BEAM PROPERTIES THROUGH THE EMMA INJECTION LINE TOMOGRAPHY SECTION. In *PAC09*, number FR5REP107, Liverpool University and STFC, Daresbury Laboratory, Warrington, UK, 2009. Held at Vancouver, BC, Canada.

[8] D J Holder. Modification of the EMMA Injection Line to act as a Full-Energy Electron Beam Diagnostic for ALICE. Internal Report, Liverpool University and Cockcroft Institute, UK, 2009.

[9] R Hofler. Simulation of transverse emittance measurements using the single slit method. Technical report, DESY Zeuthen, 2007. Summer Student Program.

[10] Yuri Saveliev. *Transverse emittance measurements: General Info and Theory*. Daresbury Laboratory, August 2009. `http://projects.astec.ac.uk/ERLPManual/index.php/Transverse_emittance_measurements`.

[11] Peter Strehl. *Beam Instrumentation and Diagnostics.* Springer, 2006.

[12] G Asova. First experience with tomographic reconstruction with quadrupole scan data. PITZ, DESY, Zeuthen, December 2009.

[13] D Stratakis, R A Kishek, H Li, S Bernal, M Walter, B Quinn, M Reiser, and P G O'Shea. Tomography as a diagnostic tool for phase space mapping of intense particle beams. *PHYSICAL REVIEW SPECIAL TOPICS - ACCELERATORS AND BEAMS*, 9:112801, 2006.

[14] D Reggiani, M Seidel, and C K Allen. TRANSVERSE PHASE-SPACE BEAM TOMOGRAPHY AT PSI AND SNS PROTON ACCELERATORS. In *IPAC10*, number MOPE065, PSI, 5232 Villigen, Switzerland and ORNL, Oak Ridge, TN 37831, U.S.A., 2010. Proceedings of IPAC10, Kyoto, Japan.

[15] U Rohrer. MAXIMUM ENTROPY BEAM TOMOGRAPHY AT PSI, Paul Scherrer Institut. `http://people.web.psi.ch/rohrer_u/ment.htm`.

[16] C B McKee, P G O'Shea, and J M J Madey. Phase space tomography of relativistic electron beams. *Nuclear Instruments and Methods in Physics Research A*, 358: 764–267, 1995.

[17] W S Graves, E D Johnson, and P G O'Shea. A HIGH RESOLUTION ELECTRON BEAM PROFILE MONITOR. Technical report, NSLS, Brookhaven National Laboratory, Upton, NY 11973 USA, Duke University, Durham, NC USA.

[18] H Ohgaki, S Hayashi, A Miyasako, T Takamatsu, K Masuda, T Kii, K Yoshikawa, and T Yamazaki. Measurements of the beam quality on ku-fel linac. *Nuclear Instruments and Methods in Physics Research Section A: Accelerators, Spectrometers, Detectors and Associated Equipment*, 528(12):366 – 370, 2004. ISSN 0168-9002. doi: http://dx.doi.org/10.1016/j.nima.2004.04.082. URL `http://www.sciencedirect.com/science/article/pii/S0168900204007223`. Proceedings of the 25th International Free Electron Laser Conference, and the 10th {FEL} Users Workshop.

[19] Tomographic reconstruction. Figure 1: Parallel beam geometry. *Wikipedia*, 20 March 2006. `http://en.wikipedia.org/wiki/File:Tomographic_fig1.png`.

[20] Radon transform. Radon Transform definition. *Wikipedia*, 6 June 2013. `http://en.wikipedia.org/wiki/Radon_transform`.

[21] Radon transform. Sinogram Result - Two Squares Phantom. *Wikipedia*, 5 April 2010. `http://en.wikipedia.org/wiki/File:Sinogram_Result_-_Two_Squares_Phantom.png`.

[22] Kevin Shivnauth. CT Scan Set-Up Diagram. *Website*. `http://computertomography.weebly.com/ct-scan-diagram.html`.

[23] X-ray computed tomography. Example of a CT pulmonary angiogram. *Wikipedia*, 3 May 2007. `http://en.wikipedia.org/wiki/File:SADDLE_PE.JPG`.

[24] A C Kak and M Slaney. *Principles of Computerized Tomographic Imaging*. IEEE Press, 1988.

[25] A Mather. Analytical and Statistical Image Reconstruction Techniques. In *Universities Nuclear Technology Forum (UNTF)*, University of Liverpool, April 2005. Held at Imperial College London.

[26] G Pratx. *Image Reconstruction In High-Resolution PET: GPU-Accelerated Strategies For Improving Image Quality And Accuracy*. PhD thesis, Department Of Electrical Engineering, Stanford University, December 2009. `http://www.stanford.edu/~pratx/thesis_guillem.pdf`.

[27] C T Mottershead. MAXIMUM ENTROPY BEAM DIAGNOSTIC TOMOGRAPHY. *IEEE Trans Nucl Science*, NS-32, No.5:764–267, 1985.

[28] Gerald Minerbo. MENT: A Maximum Entropy Algorithm for Reconstructing a Source from Projection Data. *Computer Graphics and Image Provcessing*, 10:48–68, 1979. Los Alamos Scientific Laboratory of the University of California, Los Alamos, New Mexico 87546.

[29] K M Hock. Tomography Reconstruction Codes, 2010. `http://hep.ph.liv.ac.uk/~hock/tomography/index.html`.

[30] V Yakimenko, M Babzien, I Ben-Zvi, R Malone, and X-J Wang. Electron beam phase-space measurement using a high-precision tomography technique. *PHYSICAL REVIEW SPECIAL TOPICS - ACCELERATORS AND BEAMS*, 6:122801, 2003.

[31] J J Scheins. Tomographic Reconstruction of Transverse and Longitudinal Phase Space Distributions using the Maximum Entropy Algorithm. Technical report, DESY, May 2004. TESLA Report 2004-08.

[32] F E Hannon, I V Bazarov, B Dunham, Y Li, and X Liu. PHASE SPACE TOMOGRAPHY USING THE CORNELL ERL DC GUN. In *EPAC08*, number TUPC032, Thomas Jefferson National Accelerator Facility, Newport News VA*, Cornell University, Ithaca, NY, 2008. Held at Genoa, Italy.

[33] Klaus Floettmann. *ASTRA, A Space Charge Tracking Algorithm*, October 2011. `http://www.desy.de/~mpyflo/Astra_dokumentation/Astra-Manual_V3.pdf`.

[34] Florian Lohl. Image Analysis and Emittance Calculations using OTR Beam Images. In *X-Ray FEL Commissioning Workshop*, DESY / University of Hamburg, April 2005. Held at DESY Zeuthen.

[35] G Vashchenko. Camera Measurements: Prosilica GC-1380 vs. JAI BM-141. Technical report, DESY, March 2010. PITZ physics seminar.

[36] P Williams. Analogue cameras, 2009. `http://projects.astec.ac.uk/ERLPManual/index.php/Analogue_cameras`.

[37] *Model PC-375a Black and White CCD Board Camera D-Mount.* Tokyo, Japan, November 2004. Specification Sheet.

[38] *Specification Sheet for Mini-Lens (D-Mount).* Tokyo, Japan.

[39] JAI Ltd. *Users Manual CM-140GE CB-140GE CM-140GE-RA CB-140GE-RA CM-140GE-UV Digital Monochrome / Color Progressive Scan GigE Vision Camera.* Japan, 2.0 edition, September 2009. Camera revision: G (UV:A) CMB-140GE Ver.2.0 Sept09.

[40] S H Westin. *ISO 12233 Photography - Electronic still picture cameras - Resolution Measurements Chart.*

[41] P Burns. *sfrmat 2.0 Users Guide.* pdburnsieee.org, 2.0 edition, August 2003.

[42] Ben Shepherd. *Calibrate images.nb.* ben.shepherd@stfc.ac.uk, March 2011. ALICE Camera Image Calibration.

[43] Andy Wolski. Lecture Course in Linear Dynamics, Lecture 8, 2006. University of Liverpool and the Cockcroft Institute, Daresbury, UK.

[44] M G Ibison, K M Hock, D J Holder, M Korostelev, B D Muratori, and A Wolski. MEASUREMENTS AT THE ALICE TOMOGRAPHY SECTION. In *IPAC 11*, number TUPC149, Cockcroft Institute, Daresbury Laboratory, Warrington WA4 4AD, United Kingdom, 2011. Held in San Sebastian, Spain.

[45] J M Garland, H L Owen, B D Muratori, and J W McKenzie. CHARACTERISATION OF THE ALICE ACCELERATOR AS AN INJECTOR FOR THE EMMA NS-FFAG. In *IPAC10*, number THPD030, Manchester University, STFC Daresbury Laboratory, ASTeC and Cockcroft Institute, 2010. Held at Kyoto, Japan.

[46] Dr S B van der Geer and Dr M J de Loos. *General Particle Tracer User Manual.* Eindhoven, The Netherlands, 2.80 edition. `http://www.pulsar.nl`.

[47] K M Hock and A Wolski. Tomographic Reconstruction of the Full 4D Transverse Phase Space. *Nuclear Instruments and Methods A*, 2013. Submitted.

[48] K M Hock and M G Ibison. Beam tomography in transverse normalised phase space. *Nuclear Instruments and Methods A*, 642:36–44, 2011.

[49] Kai Hock. Reconstructions: FBP vs MENT. Private communication, 2011.

[50] K M Hock and M G Ibison. A study of the Maximum Entropy Technique for phase space tomography. *Journal of Instrumentation*, 2013. in press.

[51] P A McIntosh, D Angal-Kalinin, N Bliss, S Buckley, J Clarke, G Diakun, A Gallagher, and A Gleeson. A NEW ELECTRON BEAM TEST FACILITY (EBTF) AT DARESBURY LABORATORY FOR INDUSTRIAL ACCELERATOR SYSTEM DEVELOPMENT. In *IPAC12*, number THPPR044, STFC Daresbury Laboratory, Warrington, UK, 2012. Held at New Orleans, Louisiana, USA.

[52] *EYE-10 Live Image Camera.* Vorarlberg, Austria, January 2012. `http://www.wolfvision.com/visualizer/index.php/en/live-image-camera/eye-12/specs`.